

Evaluation of failure criteria for rock under various stress states

Héloïse Fuselier

Master Thesis
Submitted 17 january 2020



University of Minnesota, Minneapolis, USA
Department of Civil, Environmental and Geo-engineering
École Polytechnique Fédérale de Lausanne, Switzerland
Faculté ENAC, Section de Génie-Civil



Supervisors:
Professor Joseph F. Labuz, University of Minnesota
Professor Lyesse Laloui, EPFL

Minneapolis, University of Minnesota, 2020

Acknowledgements

The work completed for this project would not have been possible without the assistance, help and support from several individuals. I would first like to thank Prof. Joseph Labuz for agreeing to be my thesis supervisor and giving me the chance to conduct this project at the University of Minnesota. He welcomed me with open arms and his door was always open whenever I had a question. His precious guidance and insightful comments helped me in all the time of research and writing of this thesis.

I would also like to express my sincere gratitude to Prof. Lyesse Laloui for his help and unfailing support all along my master studies at EPFL, and particularly in the search of a master thesis abroad. He always took the time to guide and help me in doubt times on my future perspectives.

I thank Pouyan Asem for his contribution to this thesis, without whom the experiments performed in this work would not have been possible. I really enjoyed our stimulating discussions which created a great atmosphere in the rock mechanics lab, and his review of this thesis was greatly appreciated. I also thank Chen, Xiaowan and Mugurel whose help was important to the success of the experiments.

My stay in the beautiful city of Minneapolis would not have been the same without Vicki. She welcomed me like I was part of her family and took care of me during these five month away from everything I knew, and I would be forever grateful for having the chance to meet her.

Last but no least, I would like to thank my family, my brother and my parents for their unconditional support and constant encouragement. Thank you to Robin for his support, encouragement, patience, catching enthusiasm and for teaching me most of the programming skills used in this thesis.

Minneapolis, January 16th 2020

H. F.

Abstract

The failure mode and strength of rock are often evaluated using failure criteria that (i) neglect the intermediate principal stress or (ii) examine conditions over a limited range of mean stress. Review of the literature, however, shows that tests involving multi-axial stress states suggest that all three principal stresses should be considered in evaluating yield or failure. Further, rock displays a pressure dependence that can be interpreted as a change in friction with mean stress. To explore the nature of stress states at failure, experiments and published data were analyzed for Dunnville sandstone within the framework of stress invariants p , q , and θ , where p = mean stress, q = deviatoric stress, and θ = Lode angle. A series of conventional triaxial compression, conventional triaxial extension, and true-triaxial tests were conducted. Published data for Dunnville sandstone were collected and a database consisting of similar tests on Dunnville sandstone was developed. The axisymmetric compression data were fitted to three failure criteria: Mohr-Coulomb (MC), Hoek-Brown (HB), Paul-Mohr-Coulomb (PMC), a generalized linear criterion containing all three principal stresses. This criterion was evaluated using three parameter and six parameter formulations. The results show that the six-parameter PMC provides the best approximation of the test data and successfully captures, in a piecewise-linear manner, the well-known nonlinear nature of the failure surface. The Paul-Mohr-Coulomb criterion representation in the $(p - q)$ diagram involves a failure surface in principal stress space that can be described as a 6-12-6 sided pyramid. The thesis presents analyses, including data from multi-axial stress states, and discussion on the three failure criteria, including details of the generalized linear condition as well as a simplified version of Paul-Mohr-Coulomb failure criterion.

Contents

Acknowledgements	i
Abstract	iii
List of figures	vii
List of tables	ix
1 Introduction	1
1.1 Introduction	1
1.2 Objective and scope	2
1.3 Thesis organization	3
2 Failure criteria	5
2.1 Introduction	5
2.2 Review	7
2.2.1 Mohr-Coulomb criterion	7
2.2.2 Hoek-Brown criterion	11
2.2.3 Paul-Mohr-Coulomb criterion	14
2.3 Paul-Mohr-Coulomb fitting	18
3 Dunnville sandstone	21
3.1 Geology, mineralogy and mechanical properties	21
3.1.1 Geological history	21
3.1.2 Mineralogy	21
3.2 Uniaxial compression test	22
3.2.1 Specimen preparation	23
3.2.2 Procedure	23
3.2.3 Results	23
3.3 Conventional triaxial tests	24
3.3.1 Hoek-Franklin cell	26
3.3.2 Specimen preparation	26
3.3.3 Conventional triaxial compression test	28
3.3.4 Conventional triaxial extension test	29
3.3.5 Results	30

Contents

4 Multi-axial experiments	35
4.1 Introduction	35
4.2 Multi-axial apparatus	36
4.2.1 Development	36
4.2.2 Description	36
4.3 Specimen preparation	38
4.3.1 Dimensions	38
4.3.2 Specimen instrumentation	39
4.3.3 Jacketing	39
4.4 Experiments	40
4.4.1 True-triaxial testing	40
4.4.2 Axisymmetric triaxial stress on a prismatic specimen	44
4.5 Results	47
4.5.1 True-triaxial experiment under plane strain condition	47
4.5.2 Axisymmetric triaxial compression experiment on a prismatic specimen	47
4.5.3 True-triaxial experiment under constant mean stress condition	51
5 Analyses and Discussion	53
5.1 Overview	53
5.2 Evaluation of the failure criteria	53
5.2.1 Mohr-Coulomb failure criterion	55
5.2.2 Hoek-Brown failure criterion	56
5.2.3 Paul-Mohr-Coulomb failure criterion with one plane	58
5.2.4 Comparison of the failure criteria	63
5.3 Paul-Mohr-Coulomb failure criterion with two planes	64
5.3.1 Paul-Mohr-Coulomb with six parameters	64
5.3.2 2-plane fitting	65
5.3.3 Dunnville sandstone	68
5.4 Simplified Paul-Mohr-Coulomb criterion	74
5.5 Discussion	76
6 Conclusion	77
A Notations	79
B Failure criterion formulation in π-plane	81
C Fitting program	85
D Paul-Mohr-Coulomb failure surface	87
E Paul-Mohr-Coulomb failure criteria for rocks from literature	89
Bibliography	92

List of Figures

2.1 Failure surface in (a) the principal stress space and (b) the π -plane [1]	7
2.2 Schematic representation of the Mohr-Coulomb criterion failure surface in $(\sigma_3 - \sigma_1)$ plane	9
2.3 Schematic representation of Mohr-Coulomb criterion failure surface in the $(p - q)$ plane	11
2.4 Schematic representation of Mohr-Coulomb criterion failure surface in π -plane	12
2.5 Schematic representation of Hoek-Brown criterion failure surface in $(\sigma_3 - \sigma_1)$ plane.	13
2.6 Schematic representation of Hoek-Brown criterion failure surface in $(p - q)$ plane.	14
2.7 Schematic representation of Hoek-Brown criterion failure surface in π -plane.	15
2.8 Schematic representation of Paul-Mohr-Coulomb criterion failure surface in $(\sigma_3 - \sigma_1)$ plane.	17
3.1 Dunnville sandstone mineralogy	22
3.2 Stress and strain response for the uniaxial compression test	25
3.3 Failed specimen after the uniaxial compression test	25
3.4 Hoek-Franklin cell	26
3.5 Conventional triaxial test set up	27
3.6 Membrane containing the rock specimen in the Hoek-Franklin cell	28
3.7 Strain Gage set up on a CTC specimen	29
3.8 Summary of the stress-strain relationships for the triaxial compression and extension tests	31
3.9 Mohr-Coulomb circles for the conventional triaxial compression tests.	31
3.10 Deformation response of Dunnville sandstone	32
4.1 Elements of the Plane Strain Apparatus	37
4.2 Specimen dimensions and loading directions	38
4.3 Specimen instrumented with axial and transversal strain gages	39
4.4 Jacketed specimen (left) and the coating set-up (right)	40
4.5 Apparatus for the true-triaxial experiments	41
4.6 Apparatus for the axisymmetric triaxial stress on a prismatic specimen	45
4.7 Stress and axial strain response for the true-triaxial experiment performed under plane strain condition	48

List of Figures

4.8 Transversal strain vs. time during true-triaxial experiment under plane strain condition	48
4.9 Failure surface of the TT 1 specimen	49
4.10 Stress vs. axial strain plot for the axisymmetric triaxial compression experiment	50
4.11 Failure surface of the TT2 specimen from the side and bottom	50
4.12 Sketch of the procedure for true-triaxial experiment under constant mean stress condition	51
4.13 Failure surface on constant mean stress test specimen	52
5.1 Mohr-Coulomb criterion failure surface in $(\sigma_3 - \sigma_1)$ plane	57
5.2 Mohr-Coulomb criterion failure surface in $(p - q)$ plane	57
5.3 Mohr-Coulomb criterion failure surface in π -plane	58
5.4 Hoek-Brown criterion failure surface in $(\sigma_3 - \sigma_1)$ plane	59
5.5 Hoek-Brown criterion failure surface in $(p - q)$ plane	59
5.6 Hoek-Brown criterion failure surface in π -plane	60
5.7 Paul-Mohr-Coulomb criterion failure surface in $(\sigma_3 - \sigma_1)$ plane	62
5.8 Paul-Mohr-Coulomb criterion failure surface in $(p - q)$ plane	62
5.9 Paul-Mohr-Coulomb criterion failure surface in π -plane	63
5.10 Paul-Mohr-Coulomb 6-12-6 sided failure surface graphical representations	66
5.11 Paul-Mohr-Coulomb 6-12-6 sided failure surface in $(\sigma_{II} - \sigma_I)$ plane	67
5.12 Paul-Mohr-Coulomb failure surface in the $(p - q)$ plane for Dunnville sandstone	71
5.13 Paul-Mohr-Coulomb failure surface in the $(\sigma_{II} - \sigma_I)$ plane for Dunnville sandstone	71
5.14 Paul-Mohr-Coulomb failure surface in the π -plane for Dunnville sandstone	72
5.15 6-12-6 sided pyramid projection in the π -plane for Dunnville sandstone	72
5.16 Paul-Mohr-Coulomb 6-12-6 sided failure surface pyramid for Dunnville sandstone	73
D.1 Paul-Mohr-Coulomb 6-12 sided failure surface graphical representations from Labuz et al. (2018) [1]	87
D.2 Paul-Mohr-Coulomb 6-6 sided failure surface graphical representations from Labuz et al. (2018) [1]	88

List of Tables

3.1	Mineralogy of Dunnville Sandstone [2]	22
3.2	Summary of CTC and CTE tests results	30
3.3	Mohr-Coulomb strength parameters for various stress regimes for Dunnville sandstone	32
3.4	Failure surfaces for conventional triaxial compression tests	33
3.5	Failure surfaces for conventional triaxial extension tests	34
4.1	Results of the true-triaxial experiment under plane-strain condition	47
4.2	Results of the axisymmetric triaxial experiment on a prismatic specimen	49
4.3	Results of the true-triaxial experiment under plane-strain condition	49
4.4	Results of the true-triaxial experiment under plane-strain condition	52
5.1	Database of experiments results for Dunnville Sandstone. The "Published" data are from Zeng et al. (2019) [3]	54
5.2	Mean standard deviation misfits obtained for the three failure criteria	64
5.3	Parameters of the planes defining the failure surface of Paul-Mohr-Coulomb criterion	64
5.4	Types of failure surfaces for the six parameters Paul-Mohr-Coulomb criterion .	65
5.5	P_1 and P_2 least-square solutions x for Dunnville sandstone	70
5.6	P_1 and P_2 strength parameters for Dunnville sandstone	70
5.7	P_1 and P_2 fitting parameters for Dunnville sandstone	70
5.8	Paul-Mohr-Coulomb general equation coefficients for Dunnville sandstone .	70
5.9	Summary of P_1 and P_2 strength parameters for Dunnville sandstone	70
5.10	Data selected to fit the simplified Paul-Mohr-Coulomb failure criterion	74
5.11	P_1 and P_2 strength parameters for Dunnville sandstone obtained from the simplified Paul-Mohr-Coulomb criterion fitting	75
5.12	Mean standard deviation misfits obtained for the three failure criteria	75
C.1	Organization of the program	85
E.1	Values of the six PMC parameters for selected rock with a 6-12-6 sided failure surface	89

1 Introduction

1.1 Introduction

The wide variety of rocks that forms the earth crust makes constitutive modeling a challenge. In some sense, each formation can in itself be considered as a different material, with diverse mineralogy, geological history, and behavior. However, a common thread is their composite structure formed by solids (minerals), pores, and cracks [1]. Years of research on these materials show similarities in response, through the definition of material parameters used to characterize their behavior. Analysis and interpretation of these experimental outcomes are key elements in the understanding of rock response, and enables safer prediction of their behavior, which is used in the design of geotechnical structures.

Rock response under a certain state of stress is often characterized by its strength. Multiple experiments, such as axisymmetric triaxial and multi-axial tests, have been developed with the aim of getting information on the various states of stress that lead to failure. However, site-specific rock engineering properties are often not available during the preliminary design phase of structures constructed on or in the rock mass. Therefore, models are widely used in the initial stage of the design for prediction of the engineering properties of the rock mass.

Over the last century, many predictive models have been developed for failure. These models describe surfaces in $(\sigma_1-\sigma_2-\sigma_3)$ space that approximate experimental data, where σ_1 , σ_2 and σ_3 are principal stresses with no regard to order. The plethora of failure criteria arise from the challenge of finding one that can give the most accurate description of rock behavior. Empirical models are usually developed for a specific rock type or rock formation and therefore, need to be evaluated before they can be applied to a design.

The most well-known and widely used failure criterion is the Mohr-Coulomb (MC) model, which provides a linear relationship between the normal stress and shear stress on the failure plane. The slope of the failure envelope is characterized by the friction angle ϕ and the shear-stress intercept, also called cohesion c [4]. MC can also be written in terms of principal stresses σ_I and σ_{III} , respectively the major and minor principal stresses; note that the intermediate

stress σ_{II} does not appear. Other criteria, such as the Hoek-Brown (HB) model for intact rocks and rock masses, are non-linear in the Mohr and $(\sigma_3 - \sigma_1)$ planes [5]. HB provides a reasonable estimate of the state of stress at failure. Note that Mohr-Coulomb and Hoek-Brown failure criteria do not include the intermediate principal stress (σ_2). Experiments have shown that the intermediate principal stress affects the mode of failure and the principal stresses that are developed at failure [1, 6, 3, 7]. Moreover, the failure envelope that describe best the experimental data is not linear over a large range of mean stress.

To address the limitations of the $\sigma_I - \sigma_{III}$ failure criteria such as that of Mohr-Coulomb, and following the pioneering work of Paul (1968), other investigators developed a failure criterion that accounts for the three principal stresses, σ_I , σ_{II} and σ_{III} [8, 9]. The piecewise linear failure surface enables a more accurate prediction of the rock behavior.

This new approach to represent rock failure and the corresponding stress state requires material constants to be evaluated and calibrated using multi-axial strength tests. Experimentation is the key element in the quest to evaluate failure criteria. In order to be recognized as accurate, the criterion should provide a failure surface that gives good prediction of the test results. It is also important that the chosen experiments are diverse and representative of the states of stress in the field. Indeed, a failure criterion well suited for the prediction of a particular test could lead to a poor estimate for another test. Therefore, additional test data will help to provide a more accurate evaluation of the model parameters for the failure criterion proposed by Paul (1968) and forms the impetus for the present work [8].

1.2 Objective and scope

The main objective of the work presented in this thesis is to explore the nature of stress states at failure as described by the three principal stresses and to investigate the accuracy of three failure criteria. A laboratory testing program was devised (i) to study the mechanical properties of Dunnville sandstone, (ii) to evaluate the existing failure criteria, and (iii) to calibrate the Paul-Mohr-Coulomb model for this rock. The following define the scope of this thesis:

1. Laboratory tests, including uniaxial compression, axisymmetric (triaxial) compression and extension are performed to characterize the elastic parameters such as Young's modulus (E) and Poisson's ratio (ν), and failure parameters such as friction angle in compression and extension (ϕ_c and ϕ_e , respectively).
2. Many geo-engineering problems involve rock subjected to a plane state of strain. It is particularly the case for tunnels and other long structures with a constant cross-section and loaded in the plane of the cross-section [4]. A true-triaxial device is used to simulate a plane strain condition, where the minor principal stress (σ_{III}) is maintained at a desired target value and the intermediate stress (σ_{II}) is increased to develop a condition where $\Delta\epsilon_2 = 0$ is simulated.

3. A true triaxial device is used to develop a stress path to failure where the mean stress is kept constant during the deviatoric loading stage by decreasing the intermediate principal stress (σ_2) and increasing the major principal stress.
4. The test results from this thesis and those reported in literature are used to evaluate various failure criteria, including the model parameters for the Paul-Mohr-Coulomb (general linear) failure criterion.

1.3 Thesis organization

Chapter 2 presents a review of three widely used failure criteria namely, Mohr-Coulomb, Hoek-Brown, and Paul-Mohr-Coulomb. Chapter 3 summarizes the geologic history and mineralogy of Dunnville sandstone as well as the results of uniaxial and conventional triaxial (compression and extension) tests on samples of Dunnville sandstone. Chapter 4 reviews the theoretical background on true triaxial experiments performed in this study, and the results of plane strain and constant mean stress tests are presented. In Chapter 5, the new test data and the existing data from published literature are used to (i) evaluate existing failure criteria, and (ii) calibrate the Paul-Mohr-Coulomb failure criterion. Chapter 6 presents the conclusions and important findings of this thesis. The symbols and notations used in this thesis are listed in Appendix A.

2 Failure criteria

Failure criteria aim to describe, in the most accurate way, failure under various states of stress. The most successful criteria are usually a generalization of experimental results, from a combination of axisymmetric and multi-axial tests. Indeed, failure criteria are a theoretical conjecture aimed to describe what is observed from material behavior. In this chapter, the mathematical formulations of selected criteria are reviewed.

2.1 Introduction

Many investigators have attempted to develop models or mathematical expressions to describe the failure of rock [1]. These criteria are usually of an empirical nature and stress based:

$$f(\sigma_{xx}, \sigma_{yy}, \sigma_{zz}, \sigma_{xy}, \sigma_{yz}, \sigma_{zx}) = \text{constant} \quad (2.1)$$

Equation 2.1 can be simplified in the case of isotropic materials and the six-parameters stress space can be reduced to three. Indeed, isotropic rock possesses strength properties that are the same in all directions, leading to directional independence. Therefore, the function can then be written in terms of principal stresses:

$$f(\sigma_I, \sigma_{II}, \sigma_{III}) = \text{constant} \quad (2.2)$$

where σ_I , σ_{II} and σ_{III} are the major, intermediate and minor principal stresses. In addition, other stress invariants can be used:

$$f(I_1, J_2, J_3) = \text{constant} \quad (2.3)$$

I_1 is the first invariant of the stress tensor σ_{ij} , J_2 and J_3 are respectively, the second and third

invariants of the deviatoric stress tensor $S_{ij} = \sigma_{ij} - p\delta_{ij}$:

$$I_1 = \sigma_I + \sigma_{II} + \sigma_{III} \quad (2.4)$$

$$J_2 = \frac{1}{6} [(\sigma_I - \sigma_{II})^2 + (\sigma_{II} - \sigma_{III})^2 + (\sigma_{III} - \sigma_I)^2] \quad (2.5)$$

$$J_3 = (\sigma_I - p)(\sigma_{II} - p)(\sigma_{III} - p) \quad (2.6)$$

Three others can be defined, and will be used in this thesis: the mean stress p , the deviatoric stress q , and the Lode angle θ :

$$f(p, q, \theta) = \text{constant} \quad (2.7)$$

with

$$p = \frac{I_1}{3} = \frac{\sigma_I + \sigma_{II} + \sigma_{III}}{3} \quad (2.8)$$

$$q = \sqrt{3J_2} = \frac{1}{6}\sqrt{[(\sigma_I - \sigma_{II})^2 + (\sigma_{II} - \sigma_{III})^2 + (\sigma_{III} - \sigma_I)^2]} \quad (2.9)$$

$$\theta = \frac{1}{3} \arccos \left(\frac{3\sqrt{3}}{2} \frac{J_3}{J_2^{3/2}} \right) = \arctan \left[\frac{\sqrt{3}(\sigma_{II} - \sigma_{III})}{2\sigma_I - \sigma_{II} - \sigma_{III}} \right] \quad (2.10)$$

The Lode angle is a measure of the stress state: $0^\circ \leq \theta \leq 60^\circ$, particularly $\theta = 0^\circ$ for axisymmetric compression $\sigma_{II} = \sigma_{III}$ and $\theta = 60^\circ$ in the case of axisymmetric extension ($\sigma_{II} = \sigma_I$).

Equations 2.2, 2.3 and 2.7 suggest that the failure surface and consequently the failure criterion has a three-dimensional nature. Indeed, depending on the stress ordering, failure criteria describe six surfaces in a three-dimensional $\sigma_1 - \sigma_2 - \sigma_3$ space: (i) $\sigma_1 \geq \sigma_2 \geq \sigma_3$, (ii) $\sigma_2 \geq \sigma_1 \geq \sigma_3$, (iii) $\sigma_2 \geq \sigma_3 \geq \sigma_1$, (iv) $\sigma_3 \geq \sigma_2 \geq \sigma_1$, (v) $\sigma_3 \geq \sigma_1 \geq \sigma_2$, (vi) $\sigma_1 \geq \sigma_3 \geq \sigma_1$. For example, a linear criterion, written in terms of the three principal stresses, σ_I , σ_{II} , σ_{III} , shows a pyramidal shape where the planes have a common vertex V_0 (the theoretical isotropic tensile strength), which is located on the tension side of the space (see Figure 2.1a).

Although the three-dimensional representation of the failure surface is the most complete, other views are often used. For example, two-dimensional coordinate systems such as $(\sigma_3 - \sigma_1)$, $(p - q)$ plane and the π -plane are simple to view. The π -plane is a section of the failure surface in the principal stress space, perpendicular to the hydrostatic axis. It is also called the equipressure plane, as the mean stress is constant over the plane. Moreover, the axes $(\sigma_1^*, \sigma_2^*, \sigma_3^*)$ are the projection of the coordinate axis on the π -plane (Figure 2.1b.). Each point in principal stress space can be represented in polar coordinates in this plane. As the mean

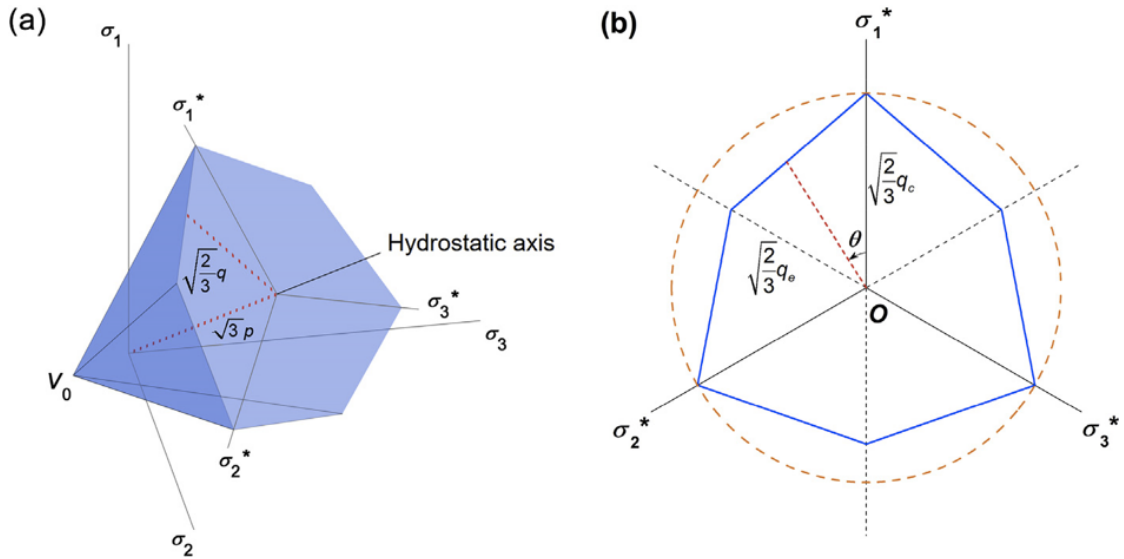


Figure 2.1: Failure surface in (a) the principal stress space and (b) the π -plane [1]

stress is constant over the π -plane, the point is at a distance r from the origin of the hydrostatic axis and oriented at the Lodge angle θ from the σ_1^* axis. Then the principal coordinates of the same point on the π -plane can be written as:

$$\sigma_1 = p + \frac{\sqrt{6}}{3}r \cos(\theta) \quad (2.11)$$

$$\sigma_2 = p - \frac{\sqrt{6}}{3}r \sin\left(\frac{\pi}{6} - \theta\right) \quad (2.12)$$

$$\sigma_3 = p - \frac{\sqrt{6}}{3}r \sin\left(\frac{\pi}{6} + \theta\right) \quad (2.13)$$

In the next sections, selected failure criteria will be presented along with their formulation in each coordinate system.

2.2 Review

2.2.1 Mohr-Coulomb criterion

The Mohr-Coulomb failure criterion (MC) is the most popular and widely used criterion. It provides a relationship between the shear stress τ and normal stress σ acting on the failure plane. The failure envelope may be represented using two material parameters known as the

Chapter 2. Failure criteria

internal failure angle ϕ and the cohesion c :

$$\tau = \sigma \tan \phi + c \quad (2.14)$$

The Mohr-Coulomb failure criterion does not consider the effect of the intermediate principal stress. The shear and normal stresses may be written in terms of the major and minor principal stresses:

$$\tau = \frac{\sigma_I - \sigma_{III}}{2} \cos \phi \quad (2.15)$$

$$\sigma = \frac{\sigma_I + \sigma_{III}}{2} - \frac{\sigma_I - \sigma_{III}}{2} \sin \phi \quad (2.16)$$

Substitution of Equations 2.15 and 2.16 in Equation 2.14 leads to a form of the Mohr-Coulomb failure criterion in terms of the major and minor principal stresses:

$$\sigma_I = \frac{1 + \sin \phi}{1 - \sin \phi} \sigma_{III} + \frac{2c \cos \phi}{1 - \sin \phi} \quad (2.17)$$

or alternatively

$$\sigma_I = K_p \sigma_{III} + C_0 \quad (2.18)$$

where K_p is the slope of the failure surface in $(\sigma_{III} - \sigma_I)$ plane and C_0 is the uniaxial compression strength of the rock.

Mohr-Coulomb in the $(\sigma_3 - \sigma_1)$ plane

Fig 2.2 presents the graphical construction of Mohr-Coulomb envelope in the $(\sigma_3 - \sigma_1)$ plane. The common vertex of the failure surfaces in extension and compression can be expressed using $\sigma_I = \sigma_{III} = -V_0$:

$$V_0 = \frac{C_0}{K_p - 1} \quad (2.19)$$

As Mohr-Coulomb does not consider the intermediate stress effect, it may be conveniently used to represent the failure for rocks subjected to stress states that may be replicated in axisymmetric triaxial tests.

Conventional (axisymmetric) Triaxial Compression (CTC):

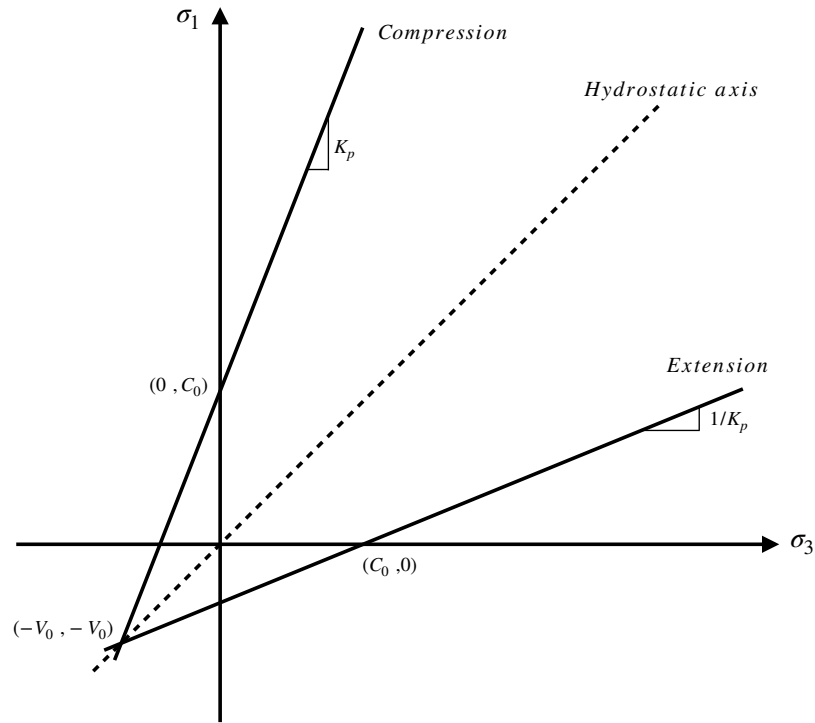


Figure 2.2: Schematic representation of the Mohr-Coulomb criterion failure surface in $(\sigma_3 - \sigma_1)$ plane

$$\sigma_I = \sigma_a \quad (2.20)$$

$$\sigma_{III} = \sigma_r \quad (2.21)$$

$$\sigma_{II} = \sigma_{III} = \sigma_r \quad (2.22)$$

Conventional (axisymmetric) Triaxial Extension (CTE):

$$\sigma_I = \sigma_r \quad (2.23)$$

$$\sigma_{III} = \sigma_a \quad (2.24)$$

$$\sigma_{II} = \sigma_I = \sigma_r \quad (2.25)$$

Mohr-Coulomb in the $(p - q)$ plane

The Mohr-Coulomb model can also be represented in $(p - q)$ plane. For example, in axisymmetric triaxial compression, Equations 2.8 and 2.9 can be written as:

$$p = \frac{\sigma_a + 2\sigma_r}{2} \quad (2.26)$$

$$q = \sigma_a - \sigma_r \quad (2.27)$$

By rearranging Equation 2.17 and incorporating the conditions for CTC, Mohr-Coulomb criterion becomes:

$$(\sigma_a - \sigma_r) = (\sigma_a + \sigma_r) \sin \phi + 2c \cos \phi \quad (2.28)$$

Expanding and substituting Equation 2.26 and 2.26 into 2.28, the following equation is obtained:

$$q_c(3 - \sin \phi) = 6p \sin \phi + 6c \cos \phi \quad (2.29)$$

Finally, the Mohr-Coulomb failure surface formulation in the $(p - q)$ plane is defined by Equation 2.30 for CTC:

$$q_c = \frac{6 \sin \phi}{3 - \sin \phi} p + \frac{6 c \cos \phi}{3 - \sin \phi} \quad (2.30)$$

Following the same approach as that for CTC, the M-C criterion for CTE may be written as:

$$q_e = \frac{6 \sin \phi}{3 + \sin \phi} p + \frac{6 c \cos \phi}{3 + \sin \phi} \quad (2.31)$$

or in the condensed form:

$$q = m_{c,e} p + b_{c,e} \quad (2.32)$$

where c and e defines m and b for compression or extension surfaces:

$$m_c = \frac{6 \sin \phi}{3 - \sin \phi} \quad (2.33)$$

$$m_e = \frac{6 \sin \phi}{3 + \sin \phi} \quad (2.34)$$

$$b_c = \frac{6 c \cos \phi}{3 - \sin \phi} \quad (2.35)$$

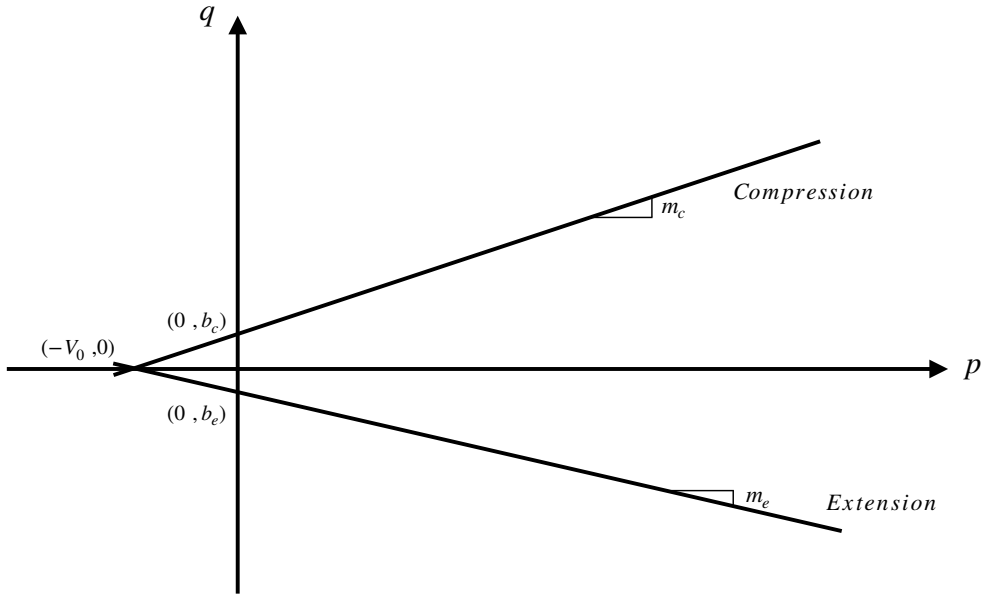


Figure 2.3: Schematic representation of Mohr-Coulomb criterion failure surface in the $(p - q)$ plane

$$b_e = \frac{6c \cos \phi}{3 + \sin \phi} \quad (2.36)$$

Figure 2.3 presents the graphical construction of the failure surfaces in the $(p - q)$ plane. In order to distinguish compression from extension data, the failure surface in extension is shown using a negative deviatoric stress $-q$.

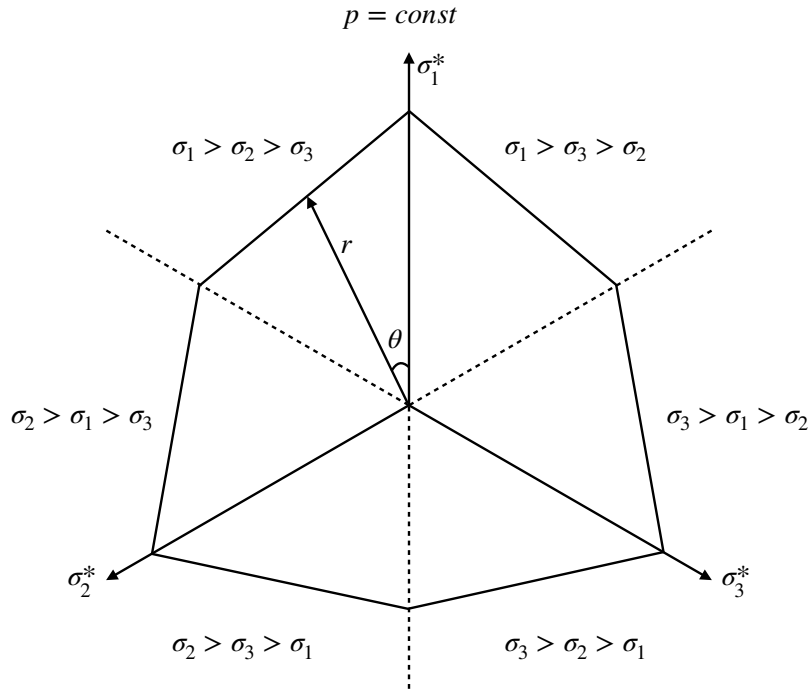
Mohr-Coulomb in the π -plane

The Mohr-Coulomb failure envelope in the π -plane is presented in Figure 2.4. The failure surfaces can be obtained by inserting Equation 2.11 and 2.13 in the criterion formulation defined by 2.18. The obtained expressions and their development are presented in Appendix B.

2.2.2 Hoek-Brown criterion

The Hoek-Brown (HB) criterion is a non-linear model for isotropic rock that does not account for the intermediate principal stress. The criterion may be written as:

$$\sigma_I = \sigma_{III} + C_0 \sqrt{m \frac{\sigma_{III}}{C_0} + s} \quad (2.37)$$


 Figure 2.4: Schematic representation of Mohr-Coulomb criterion failure surface in π -plane

Hoek and Brown (1980) [5] define m and s as constants that depends on the rock type and “blockiness”. The constant s characterizes the initial state of the tested rock. For intact rock, $s = 1.0$ and the strength parameter m is an empirical fitting parameter chosen depending on the rock type.

Hoek-Brown in the $(\sigma_3 - \sigma_1)$ plane

In $(\sigma_3 - \sigma_1)$ coordinate system, and for the axisymmetric triaxial compression tests, the Hoek-Brown criterion may be written as:

$$\sigma_a = \sigma_r + C_0 \sqrt{m \frac{\sigma_r}{C_0} + 1} \quad (2.38)$$

Similarly, the formulation for axisymmetric triaxial extension is written as:

$$\sigma_a = \sigma_r - \frac{\sqrt{4mC_0\sigma_r + m^2C_0^2 + 4C_0^2} - mC_0}{2} \quad (2.39)$$

From Equation 2.38, the theoretical isotropic tensile strength V_0 can be expressed as a function

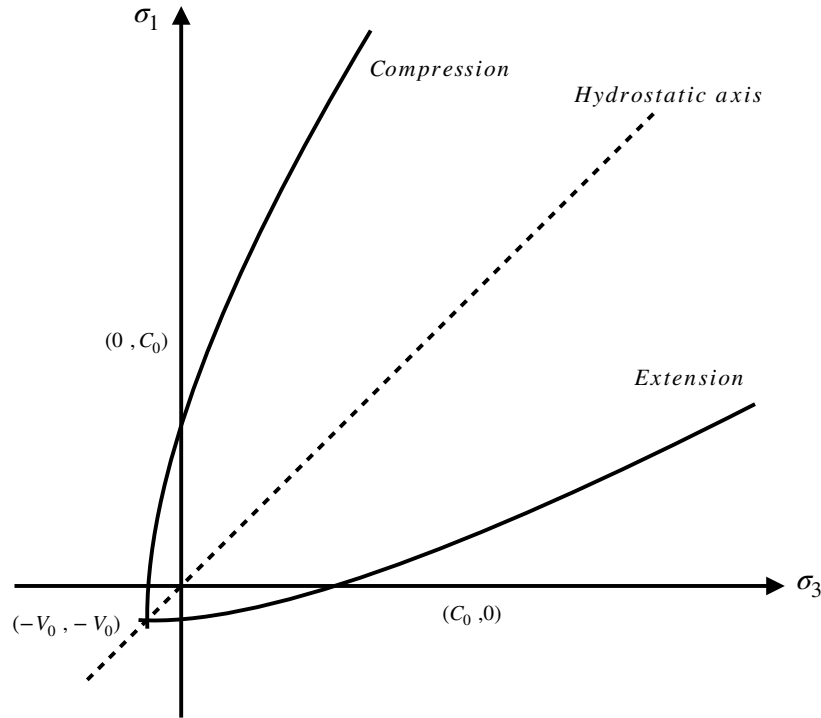


Figure 2.5: Schematic representation of Hoek-Brown criterion failure surface in $(\sigma_3 - \sigma_1)$ plane.

of the uniaxial compression strength C_0 , using : $\sigma_a = \sigma_r = -V_0$:

$$V_0 = \frac{C_0}{m} \quad (2.40)$$

Figure 2.5 presents the Hoek-Brown failure surfaces in the $(\sigma_3 - \sigma_1)$ coordinates system.

Hoek-Brown in the $(p - q)$ plane

Hoek-Brown criterion may also be expressed with the stress invariants p and q . By rearranging Equation 2.37 the formulation becomes:

$$(\sigma_I - \sigma_{III})^2 = C_0^2 \left(m \frac{\sigma_{III}}{C_0} + s \right) \quad (2.41)$$

By rearranging and inserting p and q in Equation 2.41, implicit formulation for CTC and CTE are obtained. Equation 2.42 for compression and 2.43 for extension describe Hoek-Brown criterion after solving roots of the implicit expressions:

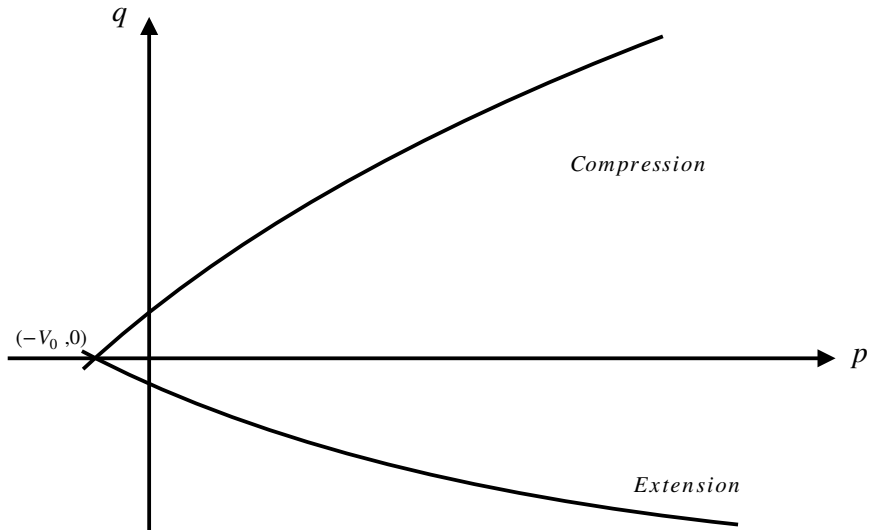


Figure 2.6: Schematic representation of Hoek-Brown criterion failure surface in $(p - q)$ plane.

$$q_c = \frac{1}{6} \left(\pm \sqrt{C_0} \sqrt{C_0 m^2 + 36C_0 + 36mp} - C_0 m \right) \quad (2.42)$$

$$q_e = \frac{1}{3} \left(\pm \sqrt{C_0^2 m^2 + 9C_0^2 + 9C_0 mp} + C_0 m \right) \quad (2.43)$$

The Hoek-Brown criterion surface fitting in the $(p - q)$ plane is presented in Figure 2.6, where the positive root of Equation 2.42 and the negative root of Equation 2.43 are considered.

Hoek-Brown in the π plane

The Hoek-Brown failure criterion in the π -plane is presented in Figure 2.7. The failure surfaces can be obtained by inserting Equation 2.11 and 2.13 in 2.37. The obtained expressions and their development are presented in Appendix B. In Figure 2.7, the surfaces are exaggerated to show the non-linearity of the criterion.

2.2.3 Paul-Mohr-Coulomb criterion

The Paul-Mohr-Coulomb criterion (PMC) is a linear model in terms of the three principal stresses. Unlike Mohr-Coulomb and Hoek-Brown, the Paul-Mohr-Coulomb criterion may be used to represent the effect of all principal stresses on rock behavior at failure. Its formulation is based on the one developed by Mohr-Coulomb, for which the intermediate stress effect is

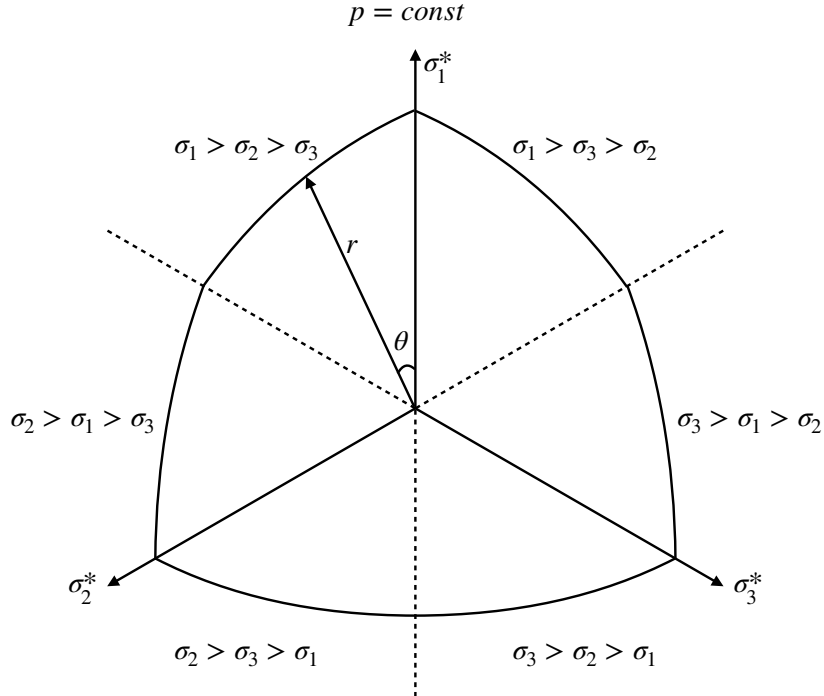


Figure 2.7: Schematic representation of Hoek-Brown criterion failure surface in π -plane.

added [8]. The Paul-Mohr-Coulomb failure criterion has the following general expression:

$$A\sigma_I + B\sigma_{II} + C\sigma_{III} = 1 \quad (2.44)$$

The ordering of the A , B and C with the major, intermediate and minor stresses should be kept as defined in Equation 2.44.

Following Meyer and Labuz (2013) [9], the coefficients A , B and C in terms of the rock properties are expressed as:

$$A = \frac{1 - \sin \phi_c}{2V_0 \sin \phi_c} \quad (2.45)$$

$$B = \frac{\sin \phi_c - \sin \phi_e}{2V_0 \sin \phi_e \sin \phi_c} \quad (2.46)$$

$$C = -\frac{1 + \sin \phi_e}{2V_0 \sin \phi_e} \quad (2.47)$$

Equation 2.44 can therefore be written in its complete form as follow:

$$\sigma_I \left[\frac{1 - \sin \phi_c}{2V_0 \sin \phi_c} \right] + \sigma_{II} \left[\frac{\sin \phi_c - \sin \phi_e}{2V_0 \sin \phi_e \sin \phi_c} \right] + \sigma_{III} \left[-\frac{1 + \sin \phi_e}{2V_0 \sin \phi_e} \right] = 1 \quad (2.48)$$

PMC refines failure criterion definition by considering different values of the rock strength parameters in compression and extension. For example, Paul-Mohr-Coulomb criterion defines two different friction angles: ϕ_c for compression and ϕ_e for extension.

Paul-Mohr-Coulomb in the $(\sigma_3 - \sigma_1)$ plane

Paul-Mohr-Coulomb is an extension of the Mohr-Coulomb criterion, therefore its expression in the $(\sigma_3 - \sigma_1)$ plane is an adjustment of Equation 2.48 considering different friction angles and cohesion for compression and extension conditions:

$$\sigma_I = M_{c,e} \sigma_{III} + C_{c,e} \quad (2.49)$$

Where:

$$M_{c,e} = \frac{1 + \sin \phi_{c,e}}{1 - \sin \phi_{c,e}} \quad (2.50)$$

$$C_{c,e} = \frac{2c_{c,e} \cos \phi_{c,e}}{1 - \sin \phi_{c,e}} \quad (2.51)$$

Paul-Mohr-Coulomb failure surfaces in $(\sigma_3 - \sigma_1)$ coordinates system are presented in Figure 2.8. The computation of V_0 will be discussed in section 2.3.

Paul-Mohr-Coulomb in the $(p - q)$ plane

The PMC in the $(p - q)$ coordinate system for axisymmetric loading may be defined as:

$$q_c = \frac{6 \sin \phi_c}{3 - \sin \phi_c} p + \frac{6c_c \cos \phi_c}{3 - \sin \phi_c} \quad (2.52)$$

$$q_e = \frac{6 \sin \phi_e}{3 + \sin \phi_e} p + \frac{6c_e \cos \phi_e}{3 + \sin \phi_e} \quad (2.53)$$

or in the indicial form as:

$$q = m_{c,e} p + b_{c,e} \quad (2.54)$$

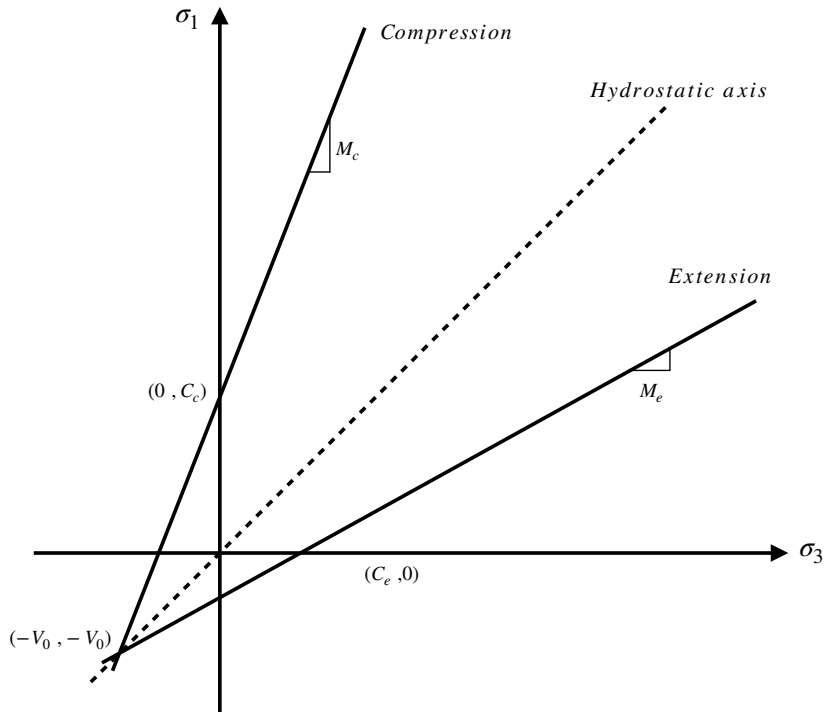


Figure 2.8: Schematic representation of Paul-Mohr-Coulomb criterion failure surface in $(\sigma_3 - \sigma_1)$ plane.

where the coefficients $m_{c,e}$ and $b_{c,e}$ are defined as follow:

$$m_c = \frac{6 \sin \phi_c}{3 - \sin \phi_c} \quad \text{and} \quad m_e = \frac{6 \sin \phi_e}{3 + \sin \phi_e} \quad (2.55)$$

$$b_c = \frac{6 c_c \cos \phi_c}{3 - \sin \phi_c} \quad \text{and} \quad b_e = \frac{6 c_e \cos \phi_e}{3 + \sin \phi_e} \quad (2.56)$$

Figure 2.3 for Mohr-Coulomb can be used to represent Paul-Mohr-Coulomb if $m_{c,e}$ and $b_{c,e}$ are used.

Paul-Mohr-Coulomb in the π plane

The representation of the Paul-Mohr-Coulomb failure criterion in the π -plane is similar to Mohr-Coulomb presented in Figure 2.4. The failure surfaces can be obtained by inserting Equation 2.11 and 2.13 in 2.48. The obtained expressions and their development are presented in Appendix B.

2.3 Paul-Mohr-Coulomb fitting

Failure criterion are conjectural. They provide a mathematical formulation of rock behavior based on experiments. However, the results obtained from them are not direct measurements of the friction angle or cohesion. The data from strength testing give the state of stress at failure. The fitting parameters are computed from these stresses.

The use of the Paul-Mohr-Coulomb requires that the model constants (V_0, ϕ_c, ϕ_e) be estimated by fitting the Paul-Mohr-Coulomb criterion to the measured data from conventional triaxial compression, conventional triaxial extension, and true triaxial tests. Labuz et al. [1] provide a detailed mathematical derivation of Equations 2.11 to 2.13 that leads to the expression of Paul-Mohr-Coulomb failure criterion in terms of the stress invariants p, q and θ .

Failure criterion fitting consists of the computation of the rock properties (V_0, ϕ) from a mathematical formulation of the criterion written in terms of the three principal stresses. Labuz (2018) [1] and Folta (2016) [10] provide detailed mathematical derivation of Equations 2.11 - 2.13 that leads to the expression of Paul-Mohr-Coulomb failure criterion in terms of the stress invariants p, q and θ .

The final formulation is given by Equation 2.57:

$$q \cos(\theta) = \frac{b_c}{V_0} p + k \sin(\theta) q + b_c \quad (2.57)$$

where:

$$k = \frac{1-2\alpha}{\sqrt{3}} \quad (2.58)$$

$$\alpha = \frac{b_c}{b_e} \quad (2.59)$$

Each data point i from a conventional triaxial or multi-axial experiment is defined by a set of (p_i, q_i, θ_i) values. Therefore, for any given data set, Equation 2.57 describes a system of linear equations. This system has m equations, with m being the number of experiments performed on the rock. Equation 2.57 can also be written as a matrix equation of the type $Ax = b$:

$$\begin{bmatrix} q_1 \cos(\theta_1) \\ \dots \\ q_m \cos(\theta_m) \end{bmatrix} = \begin{bmatrix} p_1 & q_1 \sin(\theta_1) & 1 \\ \dots & \dots & \dots \\ p_m & q_m \sin(\theta_m) & 1 \end{bmatrix} \begin{bmatrix} b_c/V_0 \\ k \\ b_c \end{bmatrix} \quad (2.60)$$

where the matrix A is m -by-3, the vector b has m -row, and the vector x has 3-row.

From the system defined in Equation 2.60, b_c , k , and V_0 and can be determined; k and b_c are given by the second and third row of parameter vector x , and V_0 and b_e are computed as

2.3. Paul-Mohr-Coulomb fitting

follow:

$$V_0 = \frac{b_c}{x_1} \quad (2.61)$$

$$b_e = \frac{2b_c}{(1 - \sqrt{3}k)} \quad (2.62)$$

The friction angles can be determined by solving Equations for 2.52 and 2.53 for $q(p = -V_0) = 0$:

$$\sin \phi_c = \frac{3b_c}{6V_0 + b_c} \quad (2.63)$$

$$\sin \phi_e = \frac{3b_e}{6V_0 - b_e} \quad (2.64)$$

Similarly, the cohesions are obtained for $q(p = 0) = b_{c,e}$:

$$c_c = \frac{b_c (3 - \sin \phi_c)}{6 \cos \phi_c} \quad (2.65)$$

$$c_e = \frac{b_e (3 + \sin \phi_e)}{6 \cos \phi_e} \quad (2.66)$$

3 Dunnville sandstone

This chapter presents a summary of geology, mineralogy, and mechanical properties of Dunnville sandstone. The results of simple tests such as uniaxial compression test and conventional triaxial tests on dry specimens are discussed and analyzed.

3.1 Geology, mineralogy and mechanical properties

In this study, Dunnville sandstone was selected for the laboratory experiments due to its availability, homogeneity and its isotropic behavior (at high mean stress when cracks are closed). Indeed, previous experiments on Dunnville Sandstone showed an isotropic behavior under different conditions of triaxial testing [2]. The following paragraphs provide a short summary of geological and mineralogical properties of Dunnville sandstone.

3.1.1 Geological history

Dunnville sandstone comes from Dunnville, Wisconsin. The quarry is located in a valley at the intersection of the Chippewa river and one of its tributary. Dunnville sandstone constituent materials were deposited during the Cambrian period when Wisconsin was submerged several times by a sea, enabling the deposition of a large amounts of sediments. The consolidation and compaction of the deposited materials by glaciers during the Pleistocene Epoch geological time and the subsequent removal of ice due to melting and rise in ambient temperatures led to the development of highly over-consolidated sedimentary rocks in the region (i.e., Dunnville sandstone). Dunnville sandstone is a member of the Elk Mound Formation and particularly the Eau Claire group [11].

3.1.2 Mineralogy

Dunnville Sandstone is composed of 90% of medium-grained quartz and a small amount of cementitious material and may be referred to as a quartz arenite. Other minerals are



Figure 3.1: Dunnville sandstone mineralogy

readily noticeable such as orange beds of alkali feldspars and biotite grains (Fig. 3.1). The elongated biotite crystals are distributed in the rock matrix and oriented parallel to the bedding. The mineralogical composition of Dunnville sandstone performed by American Engineering Testing is summarized in Table 3.1 [2]. Dunnville sandstone is a highly porous and permeable rock, with a porosity of 29-30% and permeability of 220 mD [2].

Table 3.1: Mineralogy of Dunnville Sandstone [2]

Mineral	Volume [%]
Quartz	90-95
Alkali Feldspar	2-5
Biotite	2-5
Plagioclase	Trace -1
Muscovite	Trace
Clinzoisite	Trace
Zircon	Trace
Hematite	Trace
Iron-oxide	1-2

The dry density and the P-wave velocity were measured for all specimens tested in this study. The dry density ρ is $1910 \pm 30 \text{ kg/m}^3$ and the P-wave velocity V_P is $1825 \pm 124 \text{ m/s}$. The wave travel time for evaluation of the P-wave velocity was measured perpendicular to the bedding.

3.2 Uniaxial compression test

One uniaxial compression test was performed on Dunnville sandstone to determine Young's modulus E_i and the uniaxial compressive strength C_o . These parameters are essential to understand the behavior of the rock and are used for the analysis of behavior in subsequent

chapters.

3.2.1 Specimen preparation

A cylindrical specimen was ground to ensure the ends were perpendicular to the specimen axis and oven-dried prior to test in accordance with the ISRM suggested methods [12] and ASTM standard [13]. A detailed description of the specimen preparation procedure will be presented in section 3.3.2. The specimen dimensions, with $h \approx 2d$, were: $h = 95.70\text{ mm}$, $d = 50.76\text{ mm}$. Following Labuz and Bridell (1993) [14], stearic acid was applied to the specimen ends to reduce friction and thereby to minimize the end effects.

3.2.2 Procedure

The test was performed using a 1 MN MTS closed loop servo-hydraulic load frame (MTS System Corporation). The uniaxial compression test was stroke controlled to avoid sudden failure of the rock where a displacement rate of 0.001 mm s^{-1} was used. The displacement of the actuator (stroke) and the force applied to the specimen were recorded during the test.

A small seating load of $\sim 1 - 2\text{ kN}$ was applied before the test initiated to ensure adequate contact between the loading platens and the specimen. The axial load was then increased until $\sim 50\%$ of the expected uniaxial compressive strength C_0 of the rock following by unloading to $\sim 1 - 2\text{ kN}$. This loading-unloading cycle is used to determine the Young's modulus E_i of the rock after specimen displacements were corrected for the specimen displacement. The axial load was then increased until failure of the rock specimen was achieved. The test was continued until the load decreased to $\sim 75\%$ of C_0 .

The following stress path describes the uniaxial test:

$$\sigma_1 = \sigma_a \text{ with } \sigma_a > 0 \quad (3.1)$$

$$\sigma_2 = \sigma_3 = \sigma_r \text{ with } \sigma_r = 0 \quad (3.2)$$

3.2.3 Results

From the recorded axial displacement and force, the axial stress and the axial strain can be computed:

$$\sigma_a = \frac{F_a}{A} \quad (3.3)$$

$$\epsilon_a = \frac{u}{h} \quad (3.4)$$

Where:

σ_a : axial stress [MPa]

ϵ_a : axial strain [-]

$A = \frac{d\pi^2}{4}$: cross section area of the cylindrical specimen [mm²]

F_a : axial load applied through the load frame [N]

u : axial displacement corrected for machine displacement [mm]

h : length of the specimen [mm]

Fig 3.2 present the stress-strain plot obtained from the uniaxial compression test. The uniaxial compressive strength of the rock specimen is calculated as:

$$C_o = \frac{F_{\text{peak}}}{A} = \sigma_{a,\text{peak}} = 29.83 \text{ MPa} \quad (3.5)$$

Young's modulus of the rock is computed using the loading-unloading cycle:

$$E = \frac{\Delta\sigma}{\Delta\epsilon} = 5860 \text{ MPa} \quad (3.6)$$

Fig 3.3 presents the specimen after the test. The failed specimen showed axial splitting and a failure surface with a conical shape.

3.3 Conventional triaxial tests

Shear strength of Dunnville sandstone was determined using conventional (axisymmetric) triaxial tests (CT). Two types of CT tests were performed, namely, the conventional triaxial compression (CTC) and the conventional triaxial extension (CTE). For these tests, two of the principal stresses are equal. The state of stress of the rock specimen is then simplified to the axial stress σ_a and the radial stress σ_r .

3.3. Conventional triaxial tests

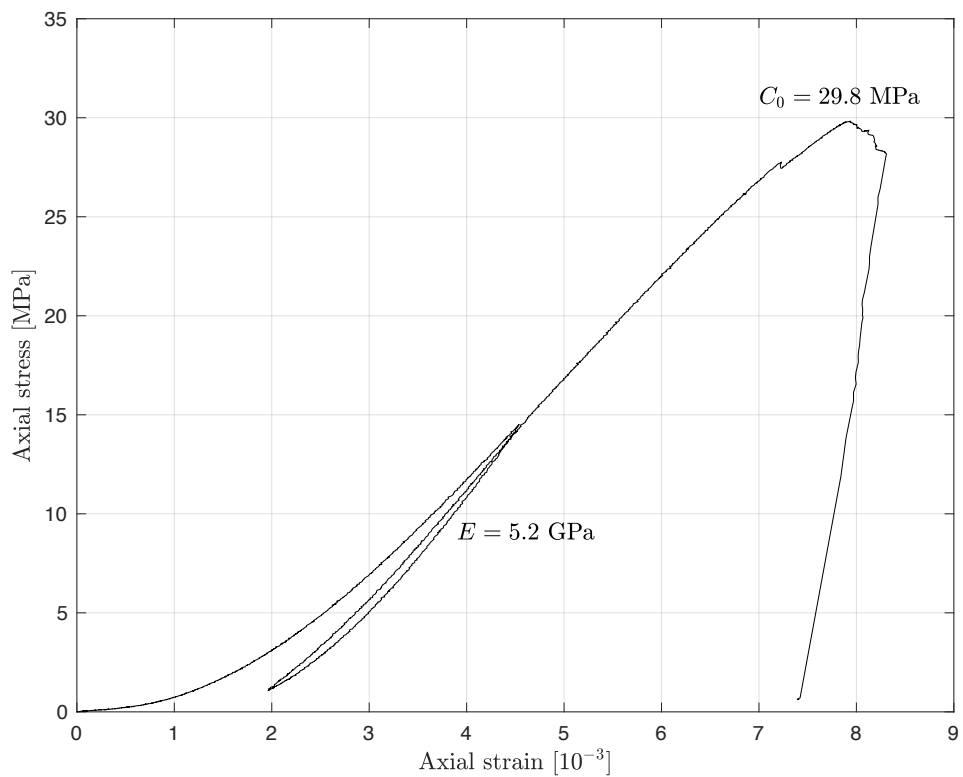


Figure 3.2: Stress and strain response for the uniaxial compression test



Figure 3.3: Failed specimen after the uniaxial compression test



Figure 3.4: Hoek-Franklin cell

3.3.1 Hoek-Franklin cell

A Hoek -Franklin pressure cell was used to perform the conventional triaxial tests [15]. The maximum capacity of the cell is 70 MPa and allows the independent application of axial and radial stresses. The device is composed of a pressure vessel, a synthetic rubber membrane and two loading platens (Fig 3.4).

The radial stress was applied using a fluid pressure system where confinement is provided using hydraulic oil. The fluid pressure system is composed of a microcontroller and a screw-type hydraulic intensifier that allows for confining pressure to be held constant throughout the test. The axial load is applied through steel platens with a 1 MN MTS servo-hydraulic load frame (MTS System Corporation). The monitoring of the axial displacement and axial force are done using a data acquisition system (Fig 3.5).

A rubber membrane was used to isolate the specimen and the loading platens from the confining fluid, and to allow for radial and axial stresses to be applied independently. The membranes used herein have an inner diameter of 32.0 mm and are 85.0 mm in height (Fig 3.6).

3.3.2 Specimen preparation

Rock cores were obtained from a block of Dunnville sandstone. The specimens were prepared following ASTM Standard Practice D4543-19 [13]. In preparation of the test specimens, particular attention was given to (i) the straightness of the elements on the cylindrical surface, (ii) flatness of the end bearing surfaces and (iii) perpendicularity of the end surfaces with the respect to axis of the core. The following describes the procedure used in preparation of the specimens:



Figure 3.5: Conventional triaxial test set up

1. *Cutting and grinding of the end surfaces:* for the purpose of sealing, the specimen dimensions should match that of the cell membrane. The core diameters ranged from 30.2 mm to 30.6 mm. The specimens were cut using a diamond saw and ground using a carborundum grinding wheel. A precision table was used to ensure that specimen ends were perpendicular to the specimen axis. The final height h of the specimens ranged from 75.7 mm to 81.8 mm
2. *Drying:* all the specimens were oven dried at 150 °C for at least 24 hours before the tests to ensure dry conditions existed during the triaxial tests
3. *Minimizing end friction:* the ends and cylindrical surface of the specimens were coated with stearic acid [13]. This lubricant was used to reduce frictional effects between the membrane and the specimen.

In addition to standard preparation, one specimen (TC 9 at $\sigma_r = 5.0 \text{ MPa}$) was equipped with a strain gages rosette where axial and transverse strains were measured (Fig 3.7). The procedure for gluing the strain gage set was executed with much care to avoid damaging the gages. Tools used in the process were cleaned with a weak acid and neutralizer before touching the strain gage. Due to the high porosity of the Dunnville sandstone, the surface of the rock was coated with the same epoxy that was used to attach the gage. The surface of the specimen was then



Figure 3.6: Membrane containing the rock specimen in the Hoek-Franklin cell

cleaned using xylene and the strain gage was attached using M-Bond 200 epoxy adhesive.

3.3.3 Conventional triaxial compression test

The following procedure was followed to setup and conduct the conventional triaxial compression tests:

1. The specimen was inserted in the Hoek-Franklin cell. The cell was held in a horizontal position and hydraulic oil was inserted to ensure no entrapped air existed in the annulus between the cell walls and the membrane.
2. The pressure cell-specimen-loading platen assembly was then placed inside the load frame and seating stress of $\sigma_a \approx 1 \text{ MPa}$ was applied to the specimen to ensure adequate contact between the specimen and the platens. To ensure small deviatoric stresses, $\sigma_r \approx 1 \text{ MPa}$ was applied. It is noted that this condition corresponds to a hydrostatic stress state ($\sigma_a = \sigma_r = 1 \text{ MPa}$).
3. The axial (σ_a) and radial (σ_r) stresses were then increased hydrostatically until the desired confining pressure (σ_r) was achieved. In so doing, a stress increment of $\sim 5.0 \text{ MPa}$ was consistently used.
4. Once the desired radial pressure σ_r was reached, the deviatoric loading was initiated by maintaining the radial stress (σ_r) constant while axial stress (σ_a) were increased until failure was achieved. It is noted that all tests were stroke controlled with a displacement rate of 0.001 ms^{-1} . The stress path applied during the test can be summarized as follow:

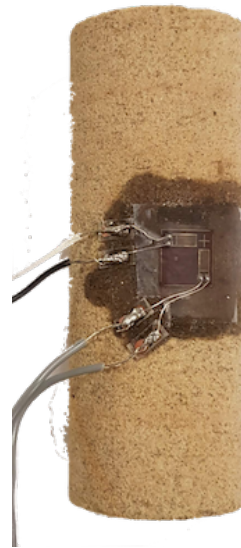


Figure 3.7: Strain Gage set up on a CTC specimen

$$\sigma_1 = \sigma_a \text{ with } \sigma_a > 0 \quad (3.7)$$

$$\sigma_2 = \sigma_3 = \sigma_r \text{ with } \sigma_r = 0 \quad (3.8)$$

$$\sigma_a > \sigma_r \quad (3.9)$$

3.3.4 Conventional triaxial extension test

The following procedure was followed to setup and run the conventional triaxial extension tests:

1. The same device and tests preparation, as those previously explained for the conventional triaxial compression tests, were used for the conventional triaxial extension tests (see steps 1-3 in Section 3.3.3).
2. In a conventional triaxial extension test, however, the axial stress is decreased as opposed to increasing the axial stress in triaxial compression tests.
3. This test was stroke controlled with displacement rate of 0.001 m s^{-1} . The radial stress was kept constant at the desired confining pressure using the hydraulic intensifier, while the axial stresses decreased through the displacement of the load frame. The stress path applied during the test can be summarized as follow:

$$\sigma_1 = \sigma_2 = \sigma_r \text{ with } \sigma_r = 0 \quad (3.10)$$

Table 3.2: Summary of CTC and CTE tests results

Test	σ_1 [MPa]	σ_2 [MPa]	σ_3 [MPa]	p [MPa]	q [MPa]	θ [$^\circ$]	E_i [MPa]
TC 9	49.43	5	5	19.81	44.43	0	5861
TC 0	61.43	10	10	27.95	51.43	0	6407
TC 5	91.08	20	20	44.72	71.08	0	7014
TC 8	127.3	40	40	65.73	87.30	0	6687
TC 10	151.1	60	60	88.12	91.10	0	6842
TE 3	35	35	3.96	24.64	31.08	60	7922
TE 1	40	40	4.50	27.89	36.34	60	8390
TE 2	60	60	9.68	43.01	50.98	60	8695

$$\sigma_3 = \sigma_a \text{ with } \sigma_a < 0 \quad (3.11)$$

$$\sigma_a < \sigma_r \quad (3.12)$$

3.3.5 Results

Five conventional triaxial compression tests ($\sigma_r = 5, 10, 20, 40$ and 60 MPa) and three conventional triaxial extension tests ($\sigma_r = 35, 40$ and 60 MPa) were performed. The test results are summarized in Table 3.2 and the stress-strain relationships for all tests are shown in Fig 3.8

Conventional triaxial compression tests

Stress vs. strain plot From 0 MPa to 20 MPa of confining stress, the rock is in the brittle domain as the axial stress is dropping after reaching maximal axial stress. At higher confining pressures ($\sigma_r > 40$ MPa and $\sigma_r < 60$ MPa), however, rock is transitioning from a brittle to ductile response as represented by the post-peak drop in stresses as seen in Fig. 3.8. Finally, the rock shows a ductile behavior under a confining stress of 60 MPa, where the axial stress does not reach a peak value.

Mohr circles plot The conventional triaxial compression results can also be presented on a Mohr plane, where the Mohr circles and the non-linear failure envelope are shown (Figure 3.9). This plot indicates that the friction angle for Dunnville sandstone is stress dependent and cannot be represented using the Mohr-Coulomb linear failure envelope for the entire range of possible stress states. The nonlinear failure envelope, however, may be linearized over small stress intervals as shown in Fig 3.9. The corresponding Mohr-Coulomb strength parameters (friction angle ϕ and cohesion intercept c) are summarized in Table 3.3.

3.3. Conventional triaxial tests

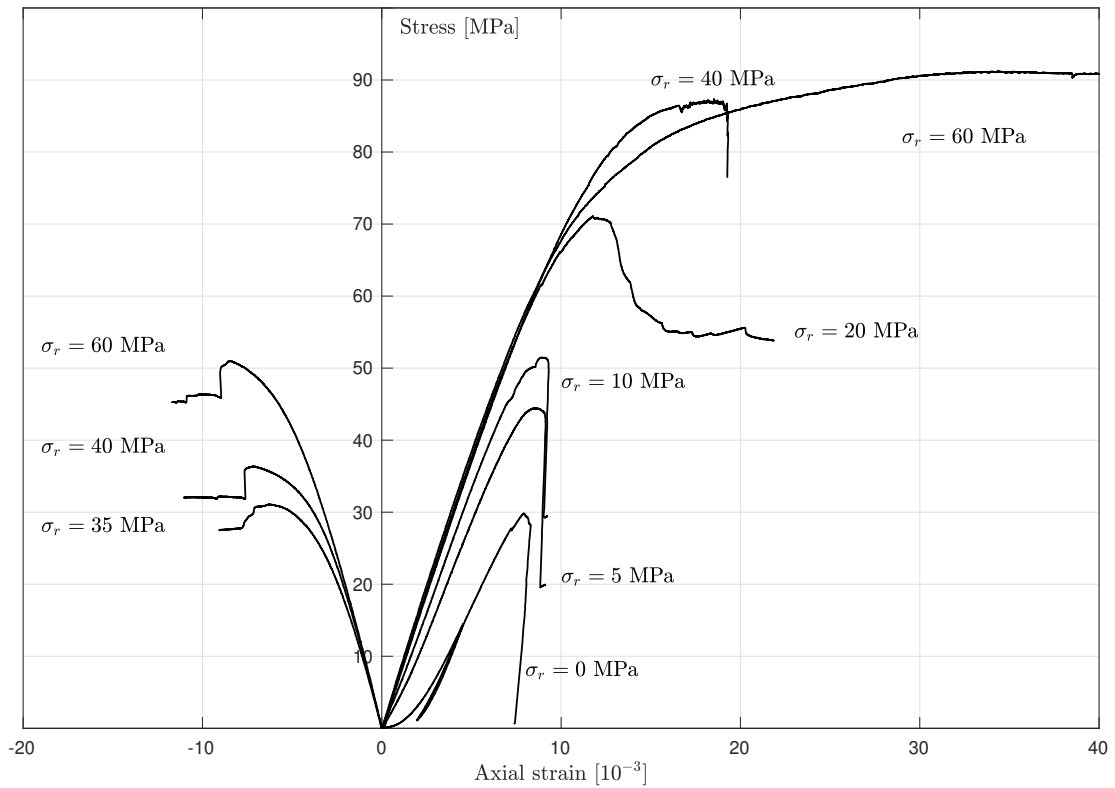


Figure 3.8: Summary of the stress-strain relationships for the triaxial compression and extension tests

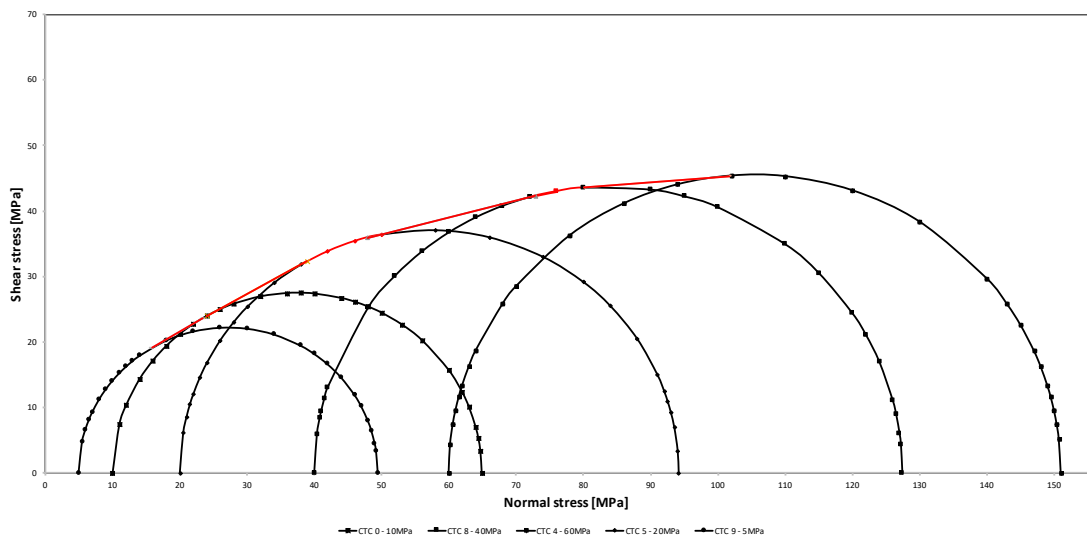


Figure 3.9: Mohr-Coulomb circles for the conventional triaxial compression tests.

Chapter 3. Dunnville sandstone

Table 3.3: Mohr-Coulomb strength parameters for various stress regimes for Dunnville sandstone

Segment	$[\phi^\circ]$	$c[\text{MPa}]$
5 – 10 MPa	30.73	9.67
10 – 20 MPa	29.37	10.42
20 – 40 MPa	14.41	23.6
40 – 60 MPa	4.72	36.94

Poisson's ratio Poisson's ratio of Dunnville sandstone was computed using the results of the axial and radial strains for specimen TC 9:

$$\nu = \frac{-\epsilon_{\text{radial}}}{\epsilon_{\text{axial}}} = 0.26 \quad (3.13)$$

Fig 3.10 shows a plot of the radial strain vs. the axial strain measured during the test.

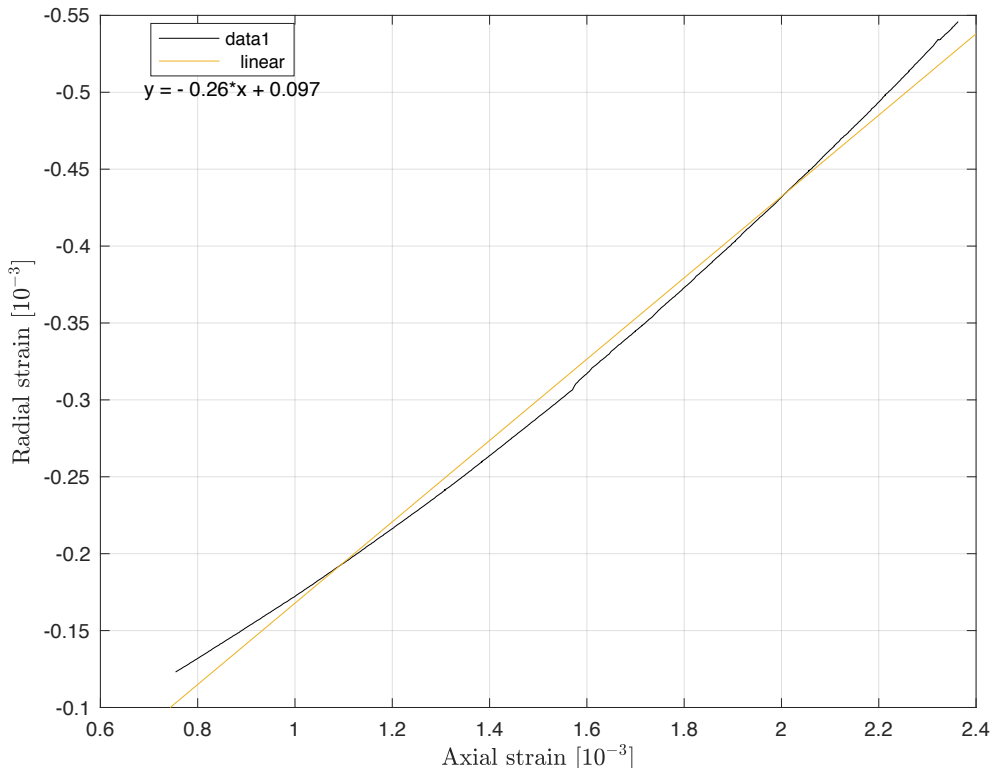
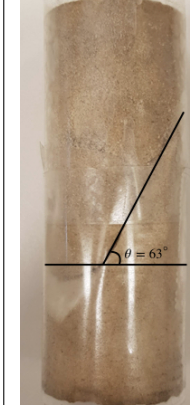
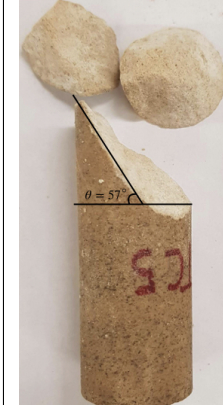
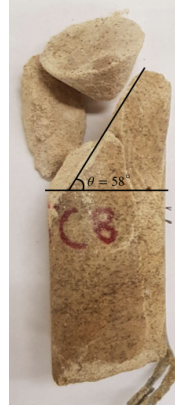


Figure 3.10: Deformation response of Dunnville sandstone

Failure surfaces Table 3.4 presents photos of the CTC tests specimens after failure, where the failure surfaces are observable. A majority of the specimens shows failure angles of approximately 60°, corresponding to the Mohr-circles prediction of $45 + \phi/2$. The specimen

3.3. Conventional triaxial tests

Table 3.4: Failure surfaces for conventional triaxial compression tests

$\sigma_r = 5 \text{ MPa}$	$\sigma_r = 10 \text{ MPa}$	$\sigma_r = 20 \text{ MPa}$	$\sigma_r = 40 \text{ MPa}$	$\sigma_r = 60 \text{ MPa}$
				
$\theta = 66^\circ$	$\theta = 63^\circ$	$\theta = 57^\circ$	$\theta = 58^\circ$	$\theta \approx 0^\circ$

tested at a confining pressure of 60 MPa showed multiple horizontal bands. At this value of mean stress, the rock behavior becomes ductile, leading to the formation of compaction bands.

Conventional triaxial extension tests

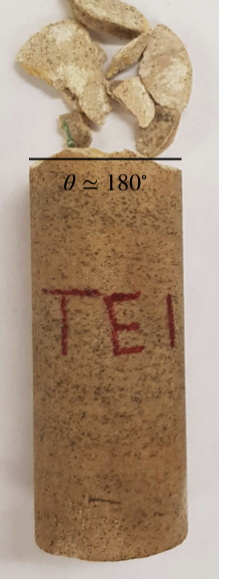
Stress vs. strain plot Fig 3.8 presents the axial stress vs. axial strain curves for the extension tests. The axial stress in the figure represents the amount of axial stress that is removed from the original hydrostatics state of stress. In order to find the axial stress at failure, the following formula is used:

$$\sigma_{\text{failure}} = \sigma_{a,\text{removed}} - \sigma_r \quad (3.14)$$

Failure surfaces Table 3.5 presents photos of the CTE tests specimens after failure.

Chapter 3. Dunnville sandstone

Table 3.5: Failure surfaces for conventional triaxial extension tests

$\sigma_r = 35 \text{ MPa}$	$\sigma_r = 40 \text{ MPa}$	$\sigma_r = 60 \text{ MPa}$
 $\theta \approx 10^\circ$	 $\theta \approx 180^\circ$	 $\theta \approx 27^\circ$
$\theta = 10^\circ$	$\theta = 0^\circ$	$\theta = 27^\circ$

4 Multi-axial experiments

The development of a successful failure criterion requires experiments and particularly multi-axial testing [1] to be performed. These tests are needed to provide material performance at various stress states, e.g. to assess the intermediate principal stress effect and to enrich the database used to calibrate failure criteria. This chapter presents the multi axial experiments performed for this study.

4.1 Introduction

The development of failure criteria requires a diversity of experiments to be the representative of the rock behavior. Axisymmetric or conventional triaxial experiments, presented in Chapter 3, are typical laboratory techniques performed as a first approach to determine strength parameters. Although they are convenient to perform, the principal stresses cannot be varied independently; two principal stresses are always equal. To address this issue, true triaxial testing was developed to represent the in-situ stress state underground, by creating “true triaxial” testing conditions that simulate three-dimensional states of stress [1].

In addition to the three-dimensional state of stress, many geo-engineering problems approximate a plane state of strain. It is particularly the case for tunnels and other long structures with a constant cross-section and loaded in the plane of the cross-section [4]. Although plane strain is a reasonable model of reality, the condition is challenging to reproduce in experiments. Indeed, on top of independent application of the three principal stresses, the plane-strain condition requires a precise control of the strain in the intermediate stress direction, as it should be equal to zero for the duration of the test.

In this study, the Plane-Strain Apparatus developed by Labuz et al. (1996) [6] was selected to perform experiments on Dunnville Sandstone, as it enables experiments to be performed under a three-dimensional stress state, with the option of restricting strain in one direction.

4.2 Multi-axial apparatus

The University of Minnesota Plane-Strain Apparatus enables independent application of the principal stresses, using a stiff biaxial frame to induce the intermediate stress through passive restraint [6]. Recent modifications of the device enable control and monitoring of the three stresses [3].

4.2.1 Development

The Plane-Strain Apparatus (US Patent number 5 063 785), was first designed based on a passive, stiff frame concept. The device enabled testing of rock specimen under plane strain conditions with active application of the major and minor stresses, and passive restraint for the intermediate stress through the biaxial frame [6].

The apparatus was recently improved with the addition of two hydraulic pistons acting in the intermediate principal stress direction which enable the active application and control of major, intermediate and minor stresses [3]. This device allows failure surfaces to develop and propagate in an unrestricted manner, unlike conventional triaxial compression where the specimen is constrained by the loading platens. In short, the Plane-Strain Apparatus gives the possibility to simulate in-situ conditions of rock underground.

4.2.2 Description

The apparatus can be defined as a pressure cell made of four components, each one related to a particular feature of the testing conditions [6, 3]. Figure 4.1 shows the elements of the Plane Strain Apparatus and denotes its components.

Base unit The base unit is equipped with high-pressure pass throughs designed to receive in-vessel instrumentation such as LVDTs (Linear Variable Differential Transformer), strain gages, and an internal load cell, above which specimen is placed.

Biaxial frame The biaxial frame was designed to bring maximum possible stiffness to the apparatus when it was used as passive restraint to restrict deformation of the specimen. It is now hosting the hydraulic pistons, with a maximum capacity of 69 MPa, that directly induce the intermediate stress. The frame is placed so that the pistons are aligned with the lateral platens fixed to the specimen. Two holes were machined in the frame to allow placement of the lateral LVDTs.

Loading piston assembly The loading piston assembly combines two features of the apparatus. It is used to apply the axial load to the specimen and enables the failure surface to

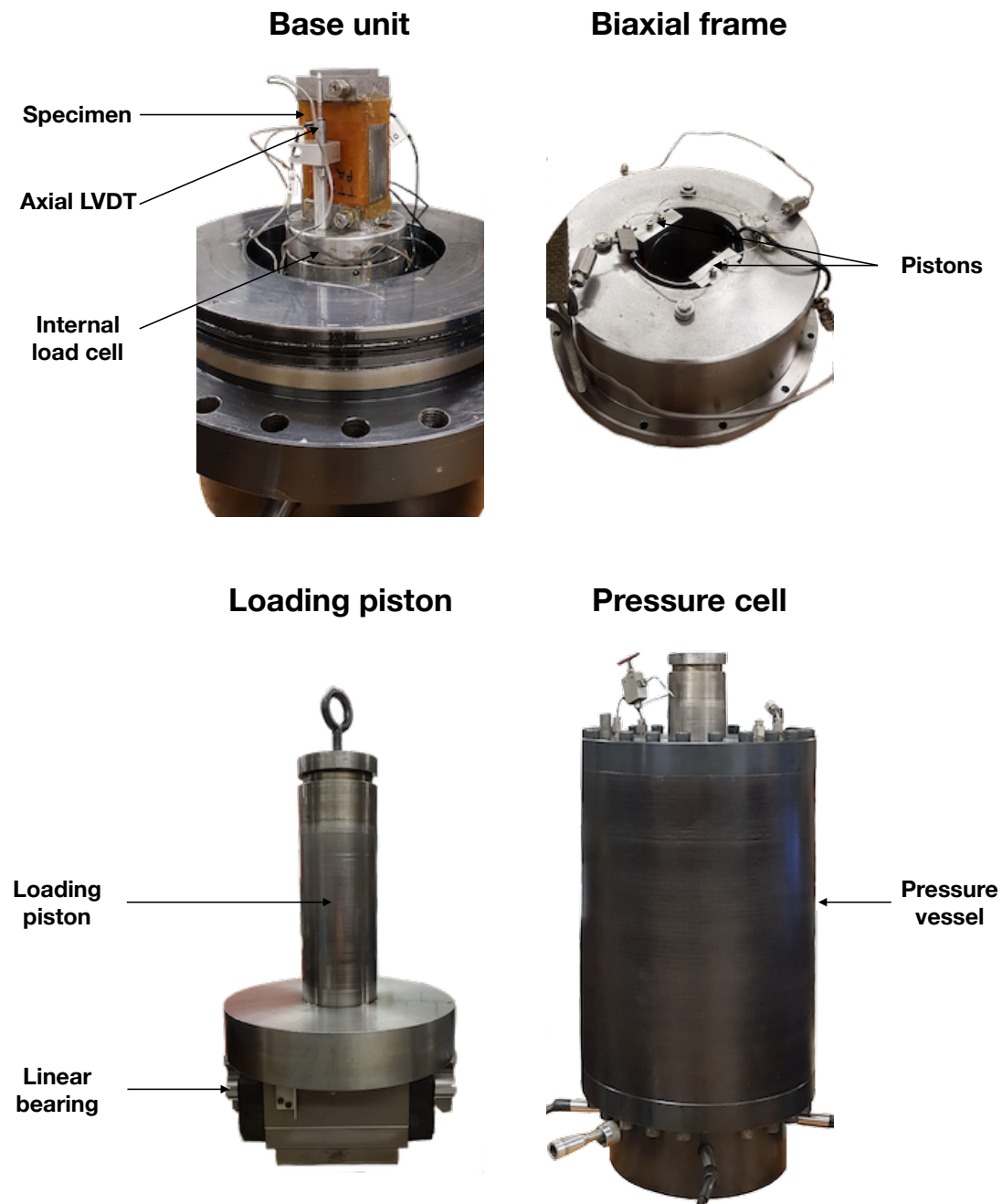


Figure 4.1: Elements of the Plane Strain Apparatus

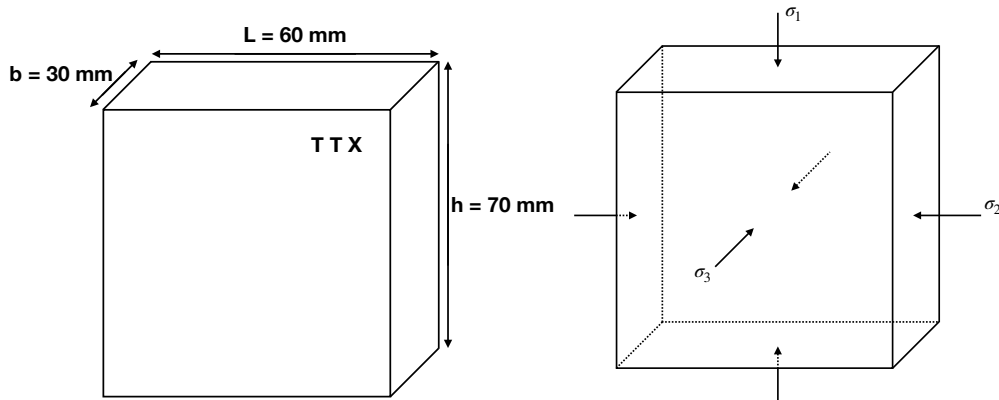


Figure 4.2: Specimen dimensions and loading directions

develop and propagate freely in the minor stress direction. It is composed of a linear bearing, bolted to the bottom of the loading piston, which can slide over a trackway when a mechanism forms. The loading piston maximum capacity is 500 MPa.

Pressure vessel The four elements presented are placed in a pressure vessel designed to hold the pressurized fluid used to apply the minor stress. The top cap and base pot are bolted to the pressure vessel surrounding the apparatus. The maximum capacity is 24 MPa.

4.3 Specimen preparation

The concept of multi axial testing involves the use of a prismatic specimen. Indeed, in order to respect their independence, each of the three principal stresses have to be applied perpendicular to the specimen surface. The specimen preparation included geometric adjustments, instrumentation with strain gages, and jacketing.

4.3.1 Dimensions

The theoretical dimensions of the specimen used for true-triaxial testing in the Plane-Strain Apparatus are presented in the Figure 4.2.

Four prismatic specimens were obtained from a block of Dunnville sandstone to minimize variation in properties. In preparation of the test specimens, particular attention was given to (i) the straightness of the elements on the cylindrical surface, (ii) flatness of the end bearing surfaces and (iii) perpendicularity of the end surfaces with the respect to axis of the core. In order to adjust the dimensions and to ensure (i), (ii) and (iii), the specimens were ground according to the ISRM suggested methods [12] and the ASTM standard [13]. A detailed description of the specimen preparation procedure is presented in section 3.3. The final dimensions for the four specimens tested were: $h = (69 \pm 1)$ mm, $L = (60 \pm 1)$ mm, $b = (30.0 \pm 0.5)$ mm.

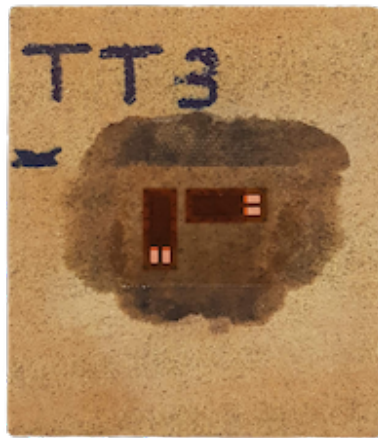


Figure 4.3: Specimen instrumented with axial and transversal strain gages

The true-triaxial experiments, in the Plane Strain Apparatus, are performed on dry specimens (drained conditions). After the geometry adjustment, the specimens were oven dried for 24 hours at 100 °C.

4.3.2 Specimen instrumentation

Strain measurements in the three principal directions are needed to analyze the volume change behavior of the rock specimen during the experiment. These measurements were made using strain gages as part of the instrumentation setup for multi axial tests.

One face of the specimens was equipped with a pair of strain gages made of one for axial strain and the other for transversal strain measurements. The set-up procedure is the same as the one described in section 3.3. Once the strain gages were fixed (24 hours of drying), the lead wires were soldered. Figure 4.3 shows the instrumentation of specimen “TT3”.

4.3.3 Jacketing

During an experiment in the Plane-Strain Apparatus, the specimen and the instrumentation are immersed in oil used to apply one of the lateral stresses. As the true-triaxial experiments were performed under drained conditions, the specimen needed to be dry (drained) for the duration of the test.

The specimen is protected from the oil by a polyurethane membrane that include the top, bottom and lateral platens in contact with the specimen (Figure 4.4a). It is done to prevent any leakage of oil inside the sample that could lead to a loss of strength for the specimen, which makes it an important but also challenging step of the experiment setup. The following coating procedure was applied:

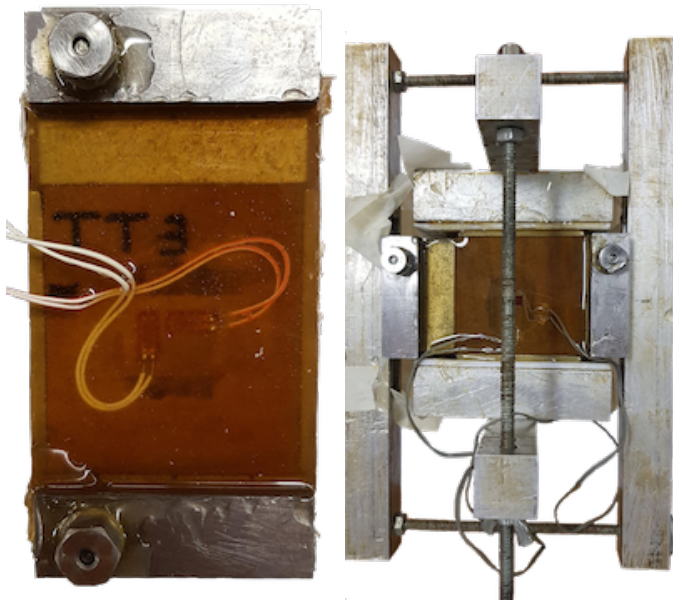


Figure 4.4: Jacketed specimen (left) and the coating set-up (right)

1. The upper, lower, and lateral platens were put in contact with the instrumented specimen and held together using clamps (Figure 4.4b)

2. Each face of the specimen was covered with two layers of polyurethane; each dried for 24 hours at room temperature

4.4 Experiments

Although the apparatus was designed about 30 years ago, the loading pistons were recently added to the biaxial frame. This new feature gave the possibility to explore new experiments conditions offered by the Plane-Strain Apparatus. Four tests were performed under different testing conditions and configuration of the equipment.

4.4.1 True-triaxial testing

Since the Plane-Strain Apparatus was improved with hydraulic pistons, several true triaxial experiments, particularly under constant mean stress conditions were performed. However, none were done under plane strain conditions. One of this study objectives was to perform the first true triaxial experiment under plane strain condition in the Plane-Strain Apparatus.



Figure 4.5: Apparatus for the true-triaxial experiments

Apparatus

1. The specimen, coated with polyurethane, was placed on the internal load cell and the position of the axial LVDTs was adjusted. The three LVDTs and the strain gages were connected to high-pressure pass throughs located on the base unit.
2. The biaxial frame was then placed on the base unit, around the specimen, and the loading piston assembly put on top of the specimen and adjusted so that it was centered with the base unit. A LVDT was then attached to the linear bearing (Figure 4.5).
3. The pressure vessel was placed around the assembly, bolted with the base unit and filled with oil.
4. Finally, the top cap was connected to the pistons' hydraulic circuit and bolted to the pressure vessel.

Plane strain condition

The plane strain testing condition involves control of the strain in the intermediate stress direction. As the axial (i.e. major) stress increases until failure, the intermediate stress should constantly be adjusted during the test to keep the strain constant and equal to zero in its direction.

The following procedure was applied to perform the true-triaxial experiment under the plane strain condition:

1. The Plane-Strain Apparatus was assembled, placed inside the MTS load frame the instrumentation was connected to the data acquisition system.
2. The hydraulic intensifiers were connected to the pressure cell and the pistons. Each one was bled to ensure no entrapped air existed in the hydraulic circuit.
3. Seating stresses of $\sigma_1 = \sigma_2 \approx 1 \text{ MPa}$ were applied to the specimen to ensure adequate contact between the specimen and the platens. A $\sigma_3 \approx 1 \text{ MPa}$ was also applied. It is noted that this condition corresponds to a hydrostatic stress state ($\sigma_1 = \sigma_2 = \sigma_3 = 1 \text{ MPa}$).
4. The three principal stresses were then increased hydrostatically until the desired confining pressure (σ_3) was achieved. In so doing, a stress increment of $\sim 2 \text{ MPa}$ was consistently used. A small deviatoric stress of about 1 MPa was kept during the hydrostatic loading to ensure good contact between the platens and the specimen.
5. Once the desired confining pressure (i.e. minor stress σ_3) was reached, the deviatoric loading was initiated by maintaining the minor stresses (σ_3) constant while the major stress (σ_1) was increased until failure was achieved. The intermediate stress was manually applied and controlled so that the strain in the intermediate stress direction (ϵ_2) was kept constant and equal to zero during the test. The stress path applied during the test can be summarized as follow:

$$\sigma_1 > 0, \quad \Delta\sigma_3 = 0 \quad \text{and} \quad \epsilon_2 = 0 \quad (4.1)$$

The minor stress was applied using a fluid pressure system where confinement is provided using hydraulic oil. The fluid pressure system is composed of a microcontroller and a screw-type hydraulic intensifier that allows for confining pressure to be held constant throughout the test. A second hydraulic intensifier was used to apply the intermediate stress through the hydraulic pistons. The major stress was applied through the loading piston with a 1 MN load frame.

During the test, the following measurements were recorded:

- Internal load applied to the specimen

- Axial displacement of the specimen
- Axial and transversal strain of the specimen
- Fluid pressure applied to the specimen (σ_3)
- Fluid pressure applied to the pistons (σ_2)
- Displacement of the linear bearing

It is noted that the test was axial displacement controlled using a displacement rate of 0.0005 m s^{-1} which was monitored from the average of the two axial LVDTs.

Constant mean stress condition

In order to compare the results given by the plane strain test, a true-triaxial experiment under constant mean stress condition was performed at the mean stress achieved at failure under plane strain condition.

The following procedure was applied:

1. The Plane-Strain Apparatus was assembled, placed inside the MTS load frame the instrumentation was connected to the testing system.
2. The hydraulic intensifiers were connected to the pressure cell and the pistons. Each one was bled to ensure no entrapped air existed in the hydraulic circuit.
3. Seating stresses of $\sigma_1 = \sigma_2 \approx 1 \text{ MPa}$ were applied to the specimen to ensure adequate contact between the specimen and the platens. A $\sigma_3 \approx 1 \text{ MPa}$ was also applied. It is noted that this condition corresponds to a hydrostatic stress state ($\sigma_1 = \sigma_2 = \sigma_3 \approx 1 \text{ MPa}$).
4. *Hydrostatic loading phase*: The three principal stresses were then increased hydrostatically until the desired confining pressure (σ_3) was achieved. In so doing, a stress increment of $\sim 2 \text{ MPa}$ was used.
5. *"Deviatoric" loading phase I*: Once the desired confining pressure (i.e. minor stress σ_3) was reached, the deviatoric loading was initiated by maintaining the minor stresses (σ_3) constant while the major (σ_1) and intermediate (σ_2) stresses were increased to the same value corresponding to the desired mean stress. The stress path applied during the phase can be summarized as follow:

$$\sigma_1 = \sigma_2 = \sigma_{1,2} \text{ with } \sigma_{1,2} = 0 \quad (4.2)$$

$$\Delta\sigma_3 = 0 \quad (4.3)$$

Chapter 4. Multi-axial experiments

6. “*Deviatoric*” loading phase 2: Once the desired mean stress was reached, it was kept constant during the rest of the test. To do so, the minor stress was kept constant and the major and intermediate stresses followed $\Delta\sigma_1 = -\Delta\sigma_2$ until failure was achieved.

The lateral stresses were applied using two hydraulic intensifiers connected to the pressure vessel and the pistons. The major stress was applied through the loading piston with a 1 MN load frame.

During the test, the following measurements were recorded:

- Internal load applied to the specimen
- Axial displacement of the specimen
- Axial and transversal strain of the specimen
- Fluid pressure applied to the specimen
- Fluid pressure applied to the pistons
- Displacement of the linear bearing

It is noted that the test was axial displacement controlled using a displacement rate of 0.0005 m s^{-1} , which was monitored from the average of the two axial LVDTs.

4.4.2 Axisymmetric triaxial stress on a prismatic specimen

One of the specimens prepared for an experiment under constant mean stress condition was too large to fit the biaxial frame. As the specimen preparation is time consuming, it was decided to modify the Plane-Strain Apparatus, by removing the biaxial frame, and to perform an axisymmetric triaxial compression test on a prismatic specimen.

In this configuration, the apparatus preserved the base unit, the loading piston and the pressure cell. The axial (major) stress was still applied by the loading piston and the intermediate stress was induced through fluid pressure, equal to the minor stress. The stress state that undergoes the specimen during this experiment was similar to the one applied in conventional triaxial compression.

Apparatus

For this experiment, the Plane-Strain Apparatus configuration was modified by removing the biaxial frame. In addition to the usual elements of the device, three steel cylinders equipped with threaded rod were placed between the base unit and the loading piston assembly (Figure 3.9).



Figure 4.6: Apparatus for the axisymmetric triaxial stress on a prismatic specimen

In the standard configuration of the device, the biaxial frame acts as an emergency stop that protects the instrumentation below the loading piston, in case of a sudden drop of the assembly due to brittle failure of the specimen. However, in this axisymmetric triaxial testing set-up, nothing stands between the base unit and the loading piston. The three cylinders were then added to the apparatus to replace the biaxial frame and avoid damaging the instrumentation around the specimen. The height was adjusted in order to have a less than 5 mm spacing with the loading piston, which correspond to the displacement range of the LVDTs placed next to the specimen.

As more space was available around the specimen, lateral LVDTs were also added to measure displacement and strain in the minor stress direction.

Procedure

The procedure defined for conventional triaxial compression in Chapter 3 was followed for this experiment:

Chapter 4. Multi-axial experiments

1. The Plane-Strain Apparatus was assembled and placed inside the MTS load frame.
2. A seating stress of $\sigma_a \approx 1 \text{ MPa}$ was applied to the specimen to ensure adequate contact between the specimen and the platens. It is noted that this condition corresponds to a hydrostatic stress state ($\sigma_r = \sigma_a \approx 1 \text{ MPa}$).
3. The axial (σ_a) and radial (σ_r) stresses were then increased hydrostatically until the desired confining pressure (σ_r) was achieved. In so doing, a stress increment of $\sim 2 \text{ MPa}$ was consistently used.
4. Once the desired confining pressure (radial stress σ_r) was reached, the deviatoric loading was initiated by maintaining the radial stresses (σ_r) constant while the axial stress (σ_a) was increased until failure was achieved. The stress path applied during the test can be summarized as follow:

$$\sigma_1 = \sigma_a \text{ with } \sigma_a > 0 \quad (4.4)$$

$$\sigma_2 = \sigma_3 = \sigma_r \text{ with } \sigma_r = 0 \quad (4.5)$$

$$\sigma_a > \sigma_r \quad (4.6)$$

σ_1 , σ_2 and σ_3 are the principal stresses of the stress state; respectively major, intermediate and minor stress.

The radial stress was applied using a fluid pressure system where confinement is provided using hydraulic oil. The axial load was applied through the loading piston with a 1 MN MTS load frame.

During the test, the following measurements were recorded:

- Internal load applied to the specimen
- Axial and lateral displacement of the specimen
- Axial and transversal strain of the specimen
- Fluid pressure applied to the specimen, i.e. σ_3
- Displacement of the linear bearing

It is noted that the test was axial displacement controlled using a displacement rate of 0.0005 m s^{-1} , which was monitored from the average of the two axial LVDTs measurements.

Table 4.1: Results of the true-triaxial experiment under plane-strain condition

Test	σ_1 [MPa]	σ_2 [MPa]	σ_3 [MPa]	p [MPa]	q [MPa]	θ [$^\circ$]
TT1	88.14	46.85	10	48.33	55.28	28.12

4.5 Results

For the purpose of this study, four experiments in the Plane-Strain Apparatus were performed: one true-triaxial test ran under plane strain condition, one axisymmetric triaxial compression test and two attempts of true-triaxial test under constant mean-stress.

4.5.1 True-triaxial experiment under plane strain condition

The true-triaxial experiment under plane strain condition was performed at a minor principal stress (i.e. σ_3) of 10 MPa. Table 4.1 summarizes the results of the experiments by presenting the stress state achieved at failure of the specimen.

The stress-strain plot, presented in Figure 4.7, shows the evolution of the three principal stresses after hydrostatic loading at 10 MPa. After reaching its peak value, the axial stress decreased rapidly which reveals the brittle post-peak behavior of the rock subject to this state of stress. By keeping $\Delta\epsilon_2 = 0$ through the test (Figure 4.8), the intermediate stress increased linearly until the major stress reached its peak value. At this point, failure of the specimen is achieved and the strain ϵ_2 increase so does the intermediate stress. The minor stress was kept constant in accordance with the experiment requirements.

Figure 4.9 shows the failed specimen the plane exposed to the pistons that applied the intermediate stress, i.e. from the $(\sigma_3 - \sigma_1)$ plane where the failure surface formed. The specimen presents a kink in the failure surface at the middle of the specimen, leading to two different angles (75° and 65°). This have also been observed in previous experiments performed in the plane strain apparatus [6]. At failure, the steeper rupture surface occurs and the ability to control the stress state is lost which create a dynamic process, leading to a less steep rupture surface.

4.5.2 Axisymmetric triaxial compression experiment on a prismatic specimen

The axisymmetric triaxial compression test was performed at a confining stress (i.e. $\sigma_2 = \sigma_3$) of 20 MPa. This minor principal stress was chosen to be close to the highest value allowed by the pressure cell capacity, which was 24 MPa. Table 4.2 summarize the results of the experiments by presenting the stress state at achieved at failure of the specimen.

The stress-strain plot, presented in Figure 4.10, shows the evolution of the three principal stresses after the hydrostatic loading at 20 MPa. After the axial stress reached a peak value of 99.95 MPa, it started to decrease before stabilizing around 95 MPa. This post-peak tendency of

Chapter 4. Multi-axial experiments

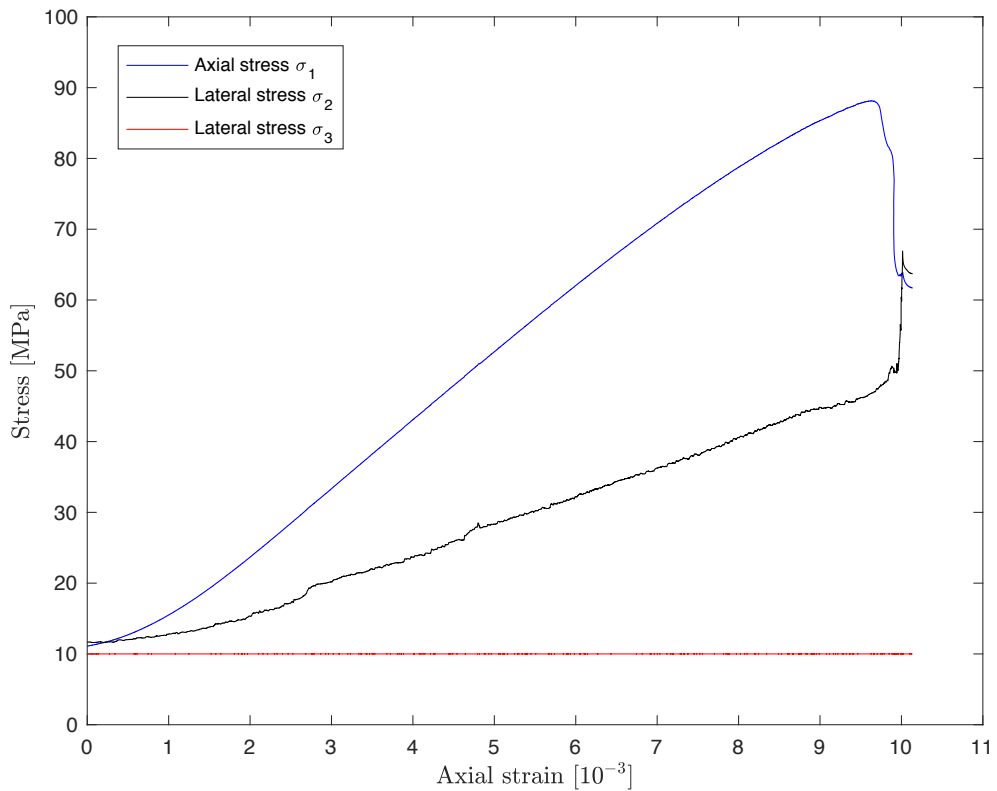


Figure 4.7: Stress and axial strain response for the true-triaxial experiment performed under plane strain condition

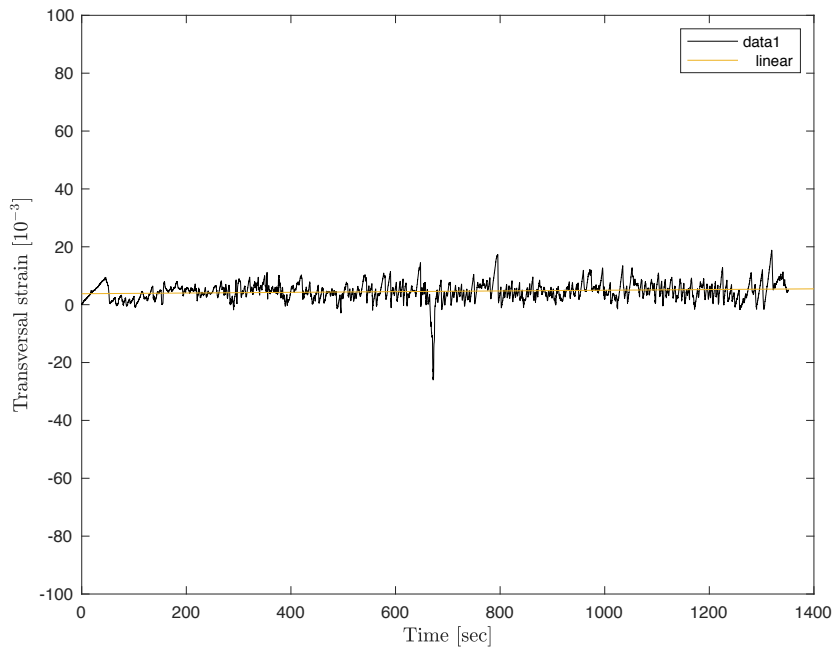


Figure 4.8: Transversal strain vs. time during true-triaxial experiment under plane strain condition

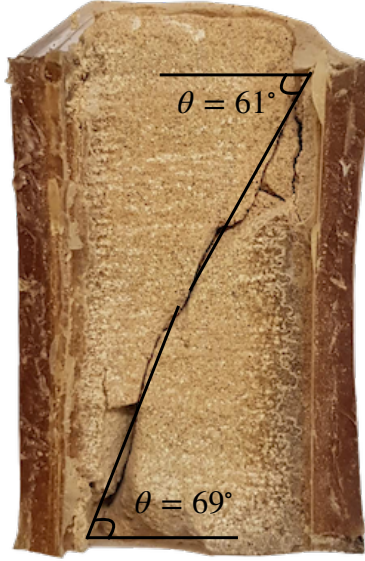


Figure 4.9: Failure surface of the TT 1 specimen

Table 4.2: Results of the axisymmetric triaxial experiment on a prismatic specimen

Test	σ_1 [MPa]	σ_2 [MPa]	σ_3 [MPa]	p [MPa]	q [MPa]	θ [$^\circ$]
TT 2	99.95	20	20	46.65	62.28	0

the axial stress can be explained by the dilatancy of the specimen along the failure surface after it was formed, and the use of axial displacement control during the experiment. The minor and intermediate stresses were kept constant in accordance with the experiment conditions requirements.

Figure 4.11 shows the failed specimen a) from the side perpendicular to the minor stress direction, and b) from the bottom (perpendicular to the axial stress). It presents a failure surface oriented at 66° in the $(\sigma_I - \sigma_{II})$ directional plane, starting from the top right and ending at the bottom middle of the specimen.

A comparison with the conventional triaxial compression test performed at 20 MPa is presented in Table 4.3. It shows a difference of $\sim 10\%$ of axial stress at peak, the higher being reached by the prismatic specimen in the Plane-Strain Apparatus.

Table 4.3: Results of the true-triaxial experiment under plane-strain condition

Test	σ_1 [MPa]	σ_2 [MPa]	σ_3 [MPa]	p [MPa]	q [MPa]	θ [$^\circ$]
TT 2	99.95	20	20	46.65	62.28	0
CTC 5	91.08	20	20	44.72	71.08	0

Chapter 4. Multi-axial experiments

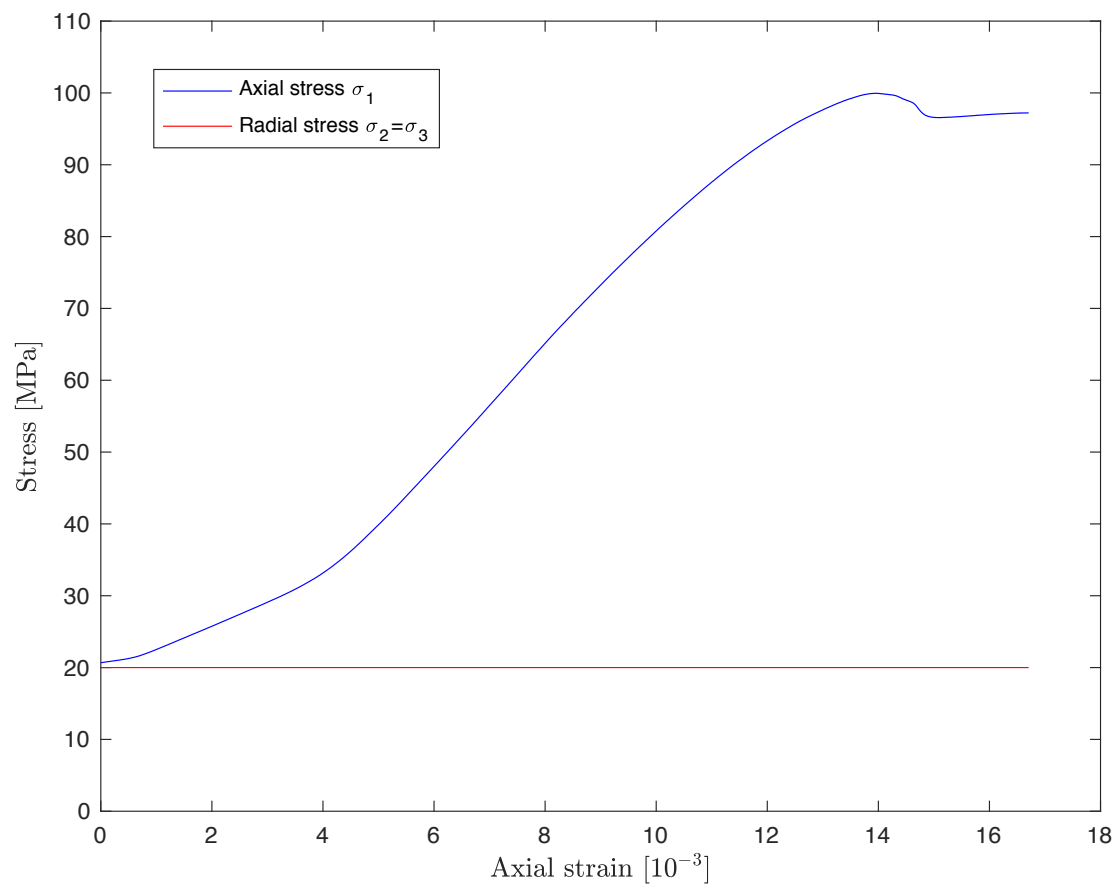


Figure 4.10: Stress vs. axial strain plot for the axisymmetric triaxial compression experiment

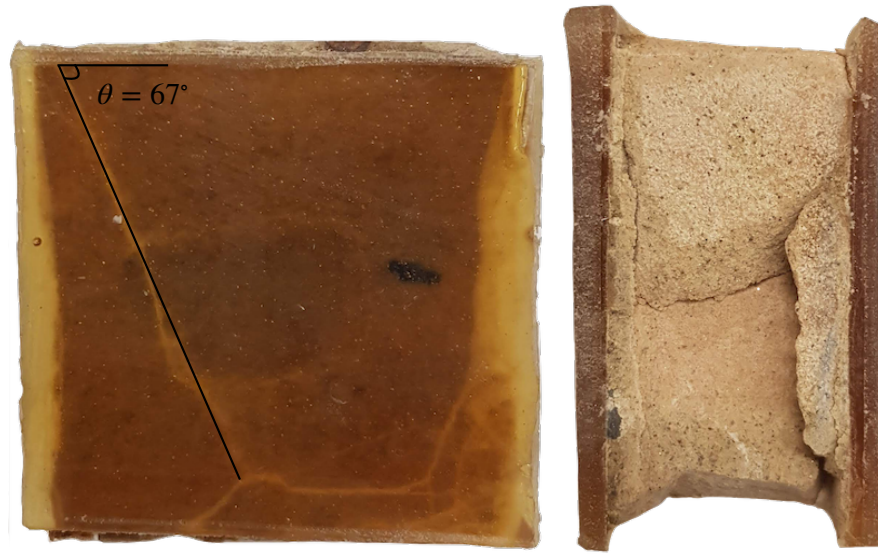


Figure 4.11: Failure surface of the TT2 specimen from the side and bottom

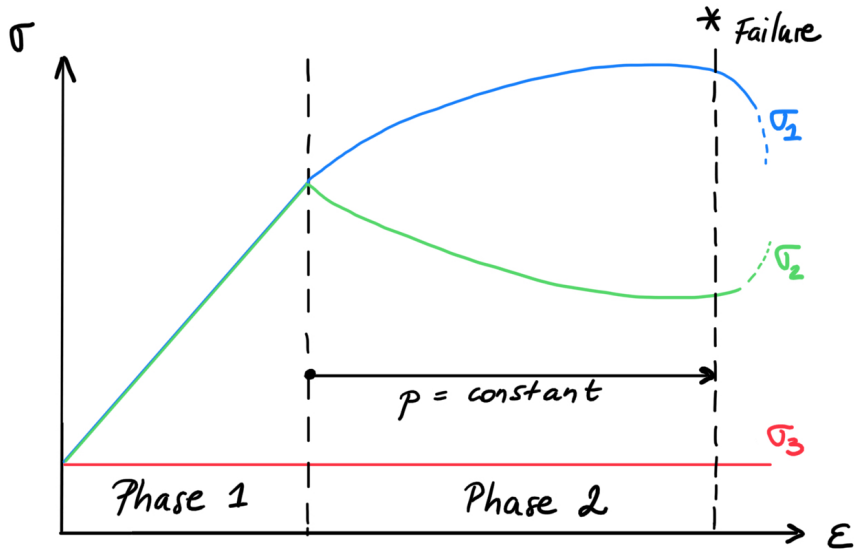


Figure 4.12: Sketch of the procedure for true-triaxial experiment under constant mean stress condition

4.5.3 True-triaxial experiment under constant mean stress condition

A true-triaxial test under constant mean stress condition was performed for this study. This test result was supposed to be compared with the one of the true-triaxial test performed under plane strain condition. Therefore, the stress path followed for the test presented in this section was based on the mean stress reach at failure for TT1.

Figure 4.12 schematically represents the procedure defined in section 4.4. The initial phase is a hydrostatic loading to achieve 10 MPa, which corresponds to the minor stress applied in the first experiment. Starting from the second phase to the end, the minor stress is kept at 10 MPa. At the end of the second phase (i.e. “deviatoric” loading phase 2), the mean stress that would be kept constant until the end of the test, is achieved. For this test, the magnitude of the major and intermediate stresses at the end of this phase were back calculated from the mean stress at failure of the first test, following Equations 4.7 to 4.10.

$$p_{TT1} = 48.3 \text{ MPa} \quad \text{and} \quad \sigma_3 = 10 \text{ MPa} \quad (4.7)$$

$$\sigma_{1,\text{init}} = \sigma_{2,\text{init}} = \sigma_{1,2} \quad (4.8)$$

$$p_{\text{initial}} = \frac{2\sigma_{1,2} - \sigma_3}{2} = 48.3 \text{ MPa} \quad (4.9)$$

$$\sigma_{1,2,\text{int}} = \frac{3p_{\text{initial}} - \sigma_3}{2} = 67.5 \text{ MPa} \quad (4.10)$$

Chapter 4. Multi-axial experiments

Table 4.4: Results of the true-triaxial experiment under plane-strain condition

σ_1 [MPa]	σ_2 [MPa]	σ_3 [MPa]
59	60.0	10.0

The test was stopped during the second phase of loading; the first phase involved hydrostatic stress of 10 MPa. The objective was to increase the axial σ_1 and lateral σ_2 stresses at the same rate to 67 MPa, but as σ_2 was increasing, before reaching 67 MPa, failure occurred while σ_1 was 60 MPa. The specimen extracted from its polyurethane coat showed a rupture plane in the $(\sigma_2 - \sigma_3)$ directional plane (Figure 4.13) leading to the following conclusions:

- The specimen failed during the second phase of loading
- Failure occurred when $\sigma_2 > \sigma_1$ and σ_2 was the major stress

The predicted axial stress at failure for the conditions of the test ($\sigma_{III} = 10$ MPa and $\sigma_{II} = 60$ MPa) was computed using the three-parameter Paul-Mohr-Coulomb failure criterion. The theoretical background of the criterion is detailed in Chapter 3 and its strength parameters obtained for Dunnville sandstone are presented in Chapter 5. The predicted σ_I at failure is presented in Table 4.4.

The state of stress at failure obtained is very close to the one applied to the specimen during the second phase of loading, and it is in agreement with the directional change of the major stress revealed by the orientation of the failure plane.



Figure 4.13: Failure surface on constant mean stress test specimen

5 Analyses and Discussion

5.1 Overview

The main objective of this study was to evaluate three failure criteria Dunnville sandstone. As explained in the previous chapters, the empirical nature of most failure criteria requires a thick database of diverse multi-axial experiments for their development.

Dunnville sandstone has been used for several works in the past and particularly for multi-axial experiments [1][3][2]. The tests performed in the scope of this study (cf. Chapter 4) presented the opportunity to enrich the existing database and to evaluate the failure criteria with data representative of Dunnville sandstone response.

The database presented in Table 5.1 is based on the work of Zeng et al. (2019) [3] and extended with the results of the experiments from this study. In this table, each experiment is associated with the following elements: the orientation of the bedding regarding the application of the axial stress, the three principal stresses $\sigma_I, \sigma_{II}, \sigma_{III}$ and the stress invariants (p, q, θ). This database was used for the evaluation of Mohr-Coulomb, Hoek-Brown and Paul-Mohr-Coulomb failure criteria.

5.2 Evaluation of the failure criteria

The Mohr-Coulomb, Hoek-Brown and Paul-Mohr-Coulomb failure criteria presented in Chapter 2 were fitted to the experiment results of Dunnville sandstone from Table 5.1. A computation program was developed for the fittings using the programming language Python. All the resources needed to access the program files are listed in Appendix C.

The three failure criteria are evaluated through their representation in the three coordinates systems presented in Chapter 2, and their accuracy in terms of how good they fit the data. In this study, this "accuracy" is chosen to be evaluated by comparing the least mean standard deviation misfits, as proposed by Benz et al. (2008) [16].

Chapter 5. Analyses and Discussion

Table 5.1: Database of experiments results for Dunnville Sandstone. The "Published" data are from Zeng et al. (2019) [3]

Test	Bedding	σ_I [MPa]	σ_{II} [MPa]	σ_{III} [MPa]	p [MPa]	q [MPa]	θ [$^{\circ}$]
Published TC-1	\perp	29.7	0.0	0.0	9.9	29.7	0
Published TC-2	\perp	39.4	2.5	2.5	14.8	36.9	0
Published TC-3	\perp	52.9	5.0	5.0	21.0	47.9	0
Published TC-4	\perp	71.5	10.0	10.0	30.5	61.5	0
Published TC-5	\perp	98.4	20.0	20.0	46.1	78.4	0
Published TC-6	\perp	114.5	30.0	30.0	58.2	84.5	0
Published TC-7	\perp	129.4	40.0	40.0	69.8	89.4	0
Published TC-8	\perp	142.1	50.0	50.0	80.7	92.1	0
Published TC-9	\perp	153.8	60.0	60.0	91.3	93.8	0
Published TC-10	\parallel	24.9	0.0	0.0	8.3	24.9	0
Published TC-11	\parallel	35.2	2.5	2.5	13.4	32.7	0
Published TC-12	\parallel	48.8	5.0	5.0	19.6	43.8	0
Published TC-13	\parallel	68.0	10.0	10.0	29.3	58.0	0
Published TC-14	\parallel	95.9	20.0	20.0	45.3	75.9	0
Published TC-15	\parallel	110.9	30.0	30.0	57.0	80.9	0
Published TC-16	\parallel	125.5	40.0	40.0	68.5	85.5	0
Published TC-17	\parallel	138.1	50.0	50.0	79.4	88.1	0
Published TC-18	\parallel	150.8	60.0	60.0	90.3	90.8	0
UCS	\perp	29.8	0	0	27.95	51.43	0
TC 9	\perp	49.43	5	5	19.81	44.43	0
TC 0	\perp	61.43	10	10	27.95	51.43	0
TC 5	\perp	91.08	20	20	44.72	71.08	0
TC 8	\perp	127.3	40	40	65.73	87.30	0
TC 10	\perp	151.1	60	60	88.12	91.10	0
Published TE-1	\perp	35.0	35.0	0.8	23.6	34.2	60
Published TE-2	\perp	40.0	40.0	1.2	27.1	38.8	60
Published TE-3	\perp	50.0	50.0	6.0	35.3	44.0	60
Published TE-4	\perp	60.0	60.0	10.1	43.4	49.9	60
Published TE-5	\perp	69.0	69.0	11.5	49.8	57.5	60
Published TE-6	\parallel	40.0	40.0	1.8	27.3	38.2	60
Published TE-7	\parallel	50.0	50.0	5.7	35.2	44.3	60
Published TE-8	\parallel	60.0	60.0	8.0	42.7	52.0	60
TE 3	\perp	35	35	3.96	24.64	31.08	60
TE 1	\perp	40	40	4.50	27.89	36.34	60
TE 2	\perp	60	60	9.68	43.01	50.98	60
Published TT-1	\perp	48.3	31.6	5.0	28.3	37.8	37.5
Published TT-2	\perp	52.9	25.1	7.0	28.3	40.1	22.7
Published TT-3	\perp	63.9	12.1	9.0	28.3	53.4	2.9
Published TT-4	\perp	70.6	49.4	15.0	45.0	48.7	37.8
Published TT-5	\perp	77.5	70.5	20.0	56.0	54.3	53.5
Published TT-6	\perp	83.9	62.1	22.0	56.0	54.4	39.7
TT 1	\perp	88.14	46.85	10	48.33	55.28	28.12
TT 2	\perp	99.98	20	20	46.65	62.28	0

The standard deviation s_i of one test series i formed by j experiments subject to the same minor stress (σ_{III}) is defined by Equation 5.1. In this expression, n is the number of experiments in the test series i , $\sigma_{I,j}^{\text{test}}$ is the maximum stress at failure for a data point j (obtained from the database) and $\sigma_{I,j}^{\text{calc}}$ is the calculated one using the considered criterion formulation.

$$s_i = \sqrt{\frac{1}{n} \sum_j (\sigma_{I,j}^{\text{calc}} - \sigma_{I,j}^{\text{test}})^2} \quad (5.1)$$

Finally, the mean standard deviation misfit is computed following Equation 5.2, where m is the number of test series. The smaller the \bar{S} is, the better is the prediction of the model for the rock compared to other criteria. A criterion that would perfectly fit the data will present no misfits.

$$\bar{S} = \frac{1}{m} \sum_i s_i \quad (5.2)$$

5.2.1 Mohr-Coulomb failure criterion

The Mohr-Coulomb failure criterion is formulated in terms of two principal stresses (Equations 2.17 and 2.18) and unique strength parameters (ϕ, c), therefore, the fitting was done using only axisymmetric triaxial compression tests results ($\theta = 0^\circ$).

From this fitting, the coefficients K_p and C_0 were determined and the other parameters were computed:

$$K_p = 2.026 \quad \text{and} \quad C_0 = 41.78 \text{ MPa} \quad (5.3)$$

$$\phi = \frac{K_p - 1}{K_p + 1} = 19.43^\circ \quad (5.4)$$

$$c = \frac{C_0(1 - \sin\phi)}{2\cos\phi} = 14.79 \text{ MPa} \quad (5.5)$$

$$V_0 = \frac{C_0}{K_p - 1} = 40.73 \text{ MPa} \quad (5.6)$$

Knowing the strength parameters, the Mohr-Coulomb failure surface is plotted in the $(\sigma_3 - \sigma_1)$ plane using Equation 2.17(Figure 5.1).

The criterion was also fitted in the $(p - q)$ plane, for which the plot obtained is shown in Figure 5.2. The coefficients $m_{c,e}$ and $b_{c,e}$ were computed using Equations 2.33 to 2.36:

$$m_c = \frac{6 \sin \phi}{3 - \sin \phi} = 0.76 \quad (5.7)$$

$$m_e = \frac{6\sin\phi}{3 + \sin\phi} = 0.61 \quad (5.8)$$

$$b_c = \frac{6c\cos\phi}{3 - \sin\phi} = 31.1 \text{ MPa} \quad (5.9)$$

$$b_e = \frac{6c\cos\phi}{3 + \sin\phi} = 24.8 \text{ MPa} \quad (5.10)$$

Finally, the Mohr-Coulomb criterion is presented in the π -plane, obtained following the procedure described in Section 2.2.1. Figure 5.3 shows Mohr-Coulomb failure criterion in the π -plane at different values of the mean stress p .

The mean standard deviation misfit obtained with the Mohr-Coulomb failure criterion is 17.7 MPa.

5.2.2 Hoek-Brown failure criterion

The Hoek-Brown failure criterion is also formulated in terms of two principal stresses (Equations 2.37) and strength parameters (m , C_0). Therefore, the fitting was done using only axisymmetric triaxial compression tests results ($\theta = 0^\circ$).

From this fitting, the strength parameters m and C_0 was determined and V_0 was computed:

$$m = 3.10 \quad \text{and} \quad C_0 = 42.35 \text{ MPa} \quad (5.11)$$

$$V_0 = \frac{C_0}{m} = 13.65 \text{ MPa} \quad (5.12)$$

Knowing the strength parameters, the Hoek-Brown failure surface is plotted in the $(\sigma_3 - \sigma_1)$ plane using Equations 2.38 for the compression line and 2.39 for extension (Figure 5.1).

In the $(p - q)$ plane, the Hoek-Brown failure criterion is plotted using Equations 2.42 for compression and 2.43 for extension, and shown in Figure 5.5. These surfaces are expressed in terms of m and C_0 previously defined.

Finally, the Hoek-Brown criterion is presented in the π -plane, obtained following the procedure described in Section 2.2.2. Figure 5.6 shows Hoek-Brown failure criterion in the pi-plane at different values of the mean stress p .

The mean standard deviation misfit obtained with the Hoek-Brown failure criterion is 17.5 MPa.

5.2. Evaluation of the failure criteria

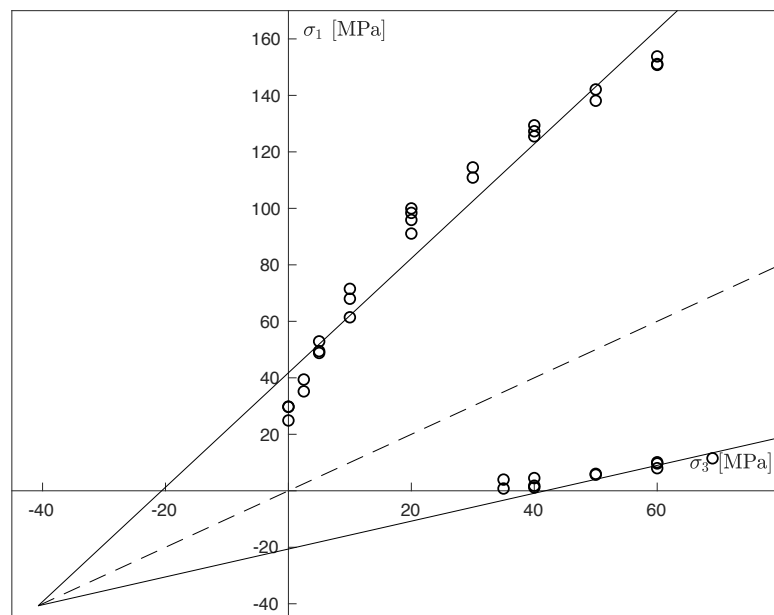


Figure 5.1: Mohr-Coulomb criterion failure surface in $(\sigma_3 - \sigma_1)$ plane

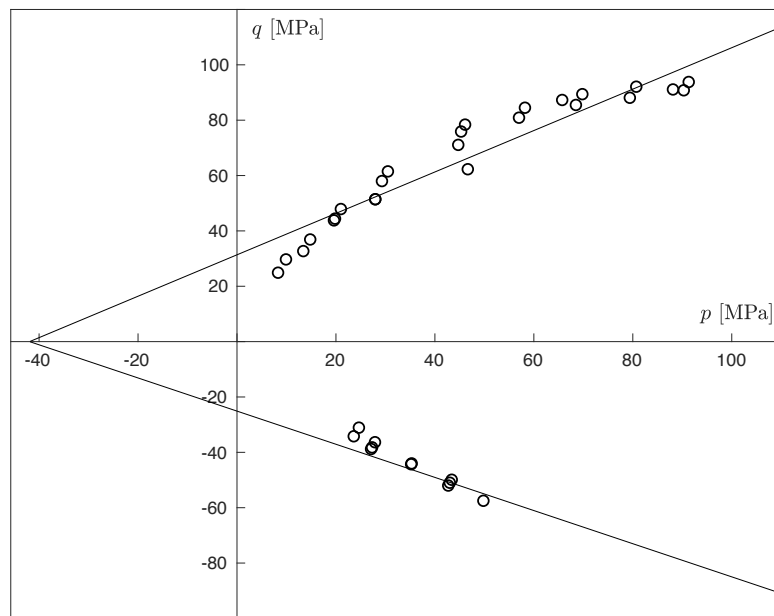
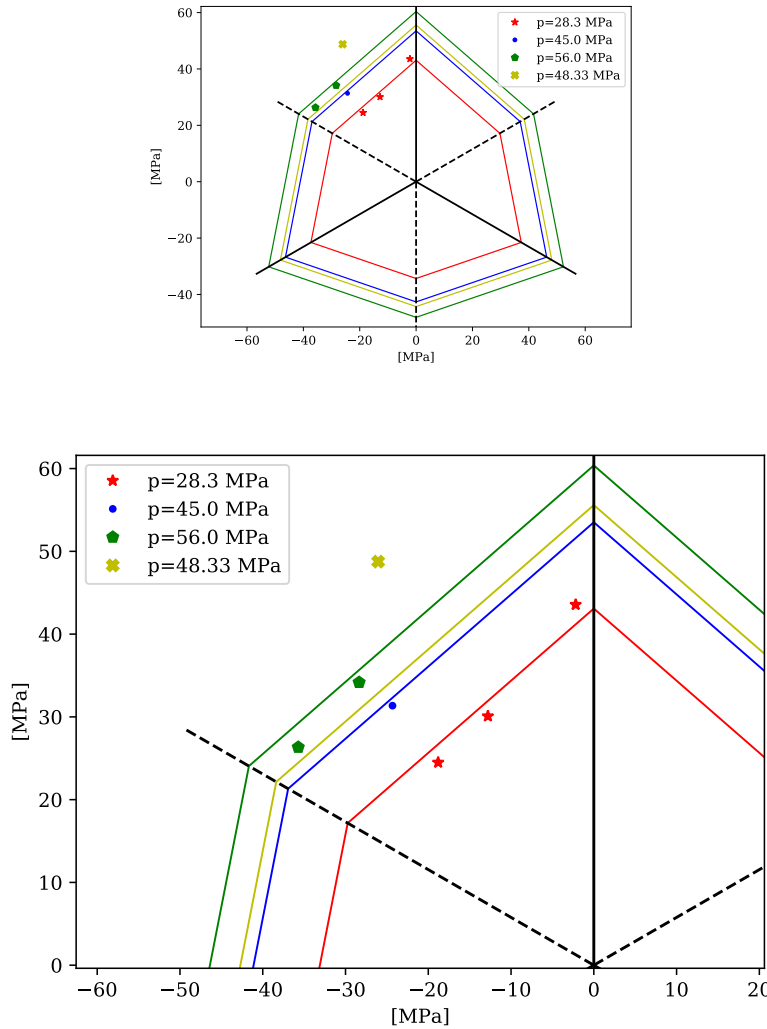


Figure 5.2: Mohr-Coulomb criterion failure surface in $(p - q)$ plane


 Figure 5.3: Mohr-Coulomb criterion failure surface in π -plane

5.2.3 Paul-Mohr-Coulomb failure criterion with one plane

Contrary to the previous criteria, the Paul-Mohr-Coulomb failure criterion is formulated in terms of the three principal stresses (Equations 2.44 and 2.48) and non-unique strength parameters (i.e. $\phi_{c,e}$, $c_{c,e}$, V_0). Therefore, the fitting was done using all tests results from the database.

From the least-square solution fitting described in Chapter 2 (cf. Section 2.3, Equations 2.57 and 2.62), the following solution could be obtained:

$$x_1 = \frac{b_c}{V_0} = 0.81 \quad (5.13)$$

5.2. Evaluation of the failure criteria

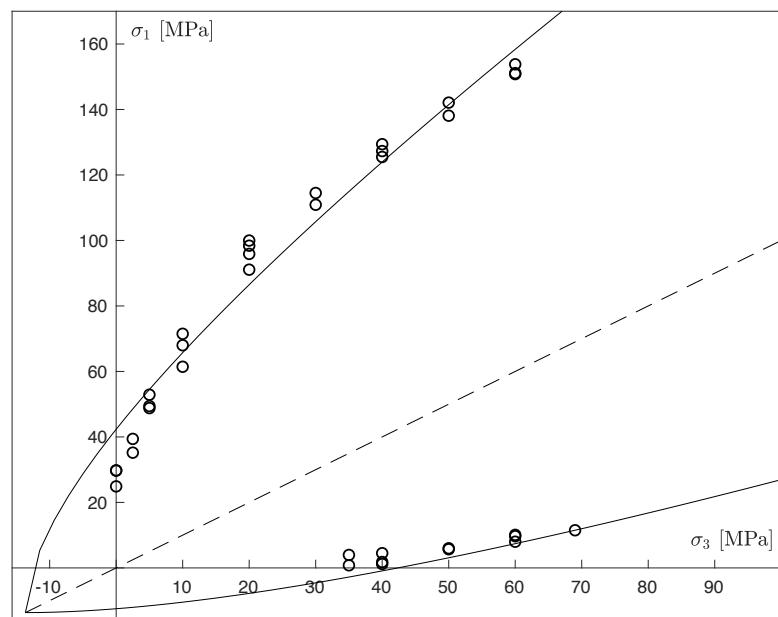


Figure 5.4: Hoek-Brown criterion failure surface in $(\sigma_3 - \sigma_1)$ plane

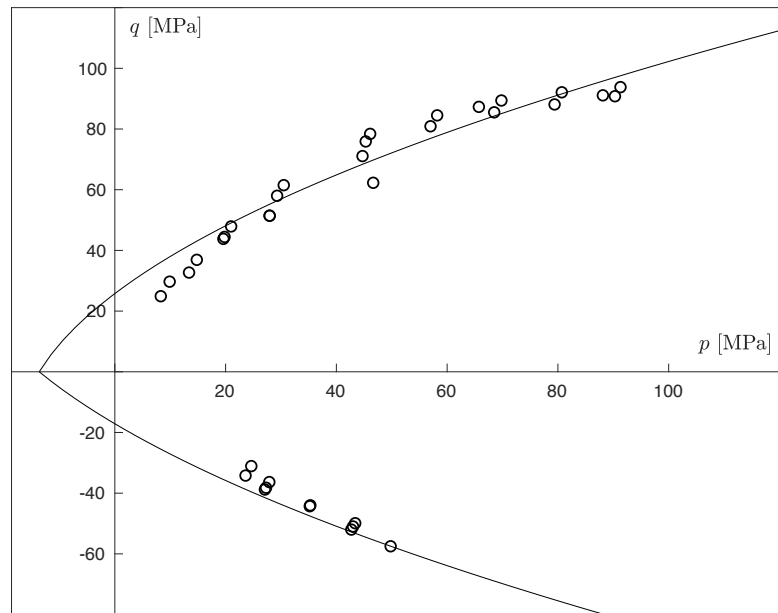


Figure 5.5: Hoek-Brown criterion failure surface in $(p - q)$ plane

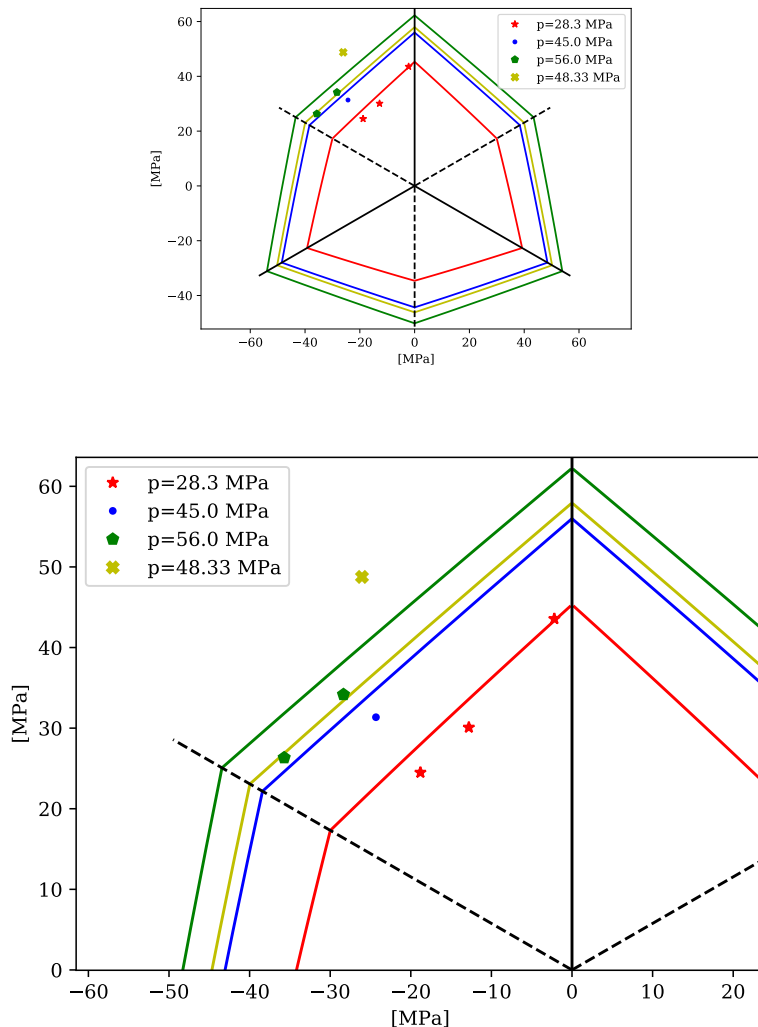


Figure 5.6: Hoek-Brown criterion failure surface in π -plane

$$x_2 = k = -0.91 \quad (5.14)$$

$$x_3 = b_c = 28.77 \text{ MPa} \quad (5.15)$$

Following Equations 2.61 to 2.65, the strength parameters for Paul-Mohr-Coulomb failure criteria can be computed:

$$V_0 = \frac{b_c}{0.81} = 35.62 \text{ MPa} \quad (5.16)$$

$$b_e = \frac{2b_c}{(1 - \sqrt{3}k)} = 22.31 \text{ MPa} \quad (5.17)$$

$$\phi_c = \arcsin\left(\frac{3b_c}{6V_0 + b_c}\right) = 20.85^\circ \quad (5.18)$$

$$\phi_e = \arcsin\left(\frac{3b_e}{6V_0 - b_e}\right) = 20.46^\circ \quad (5.19)$$

$$c_c = \frac{b_c(3 - \sin\phi_c)}{6\cos\phi_c} = 13.57 \text{ MPa} \quad (5.20)$$

$$c_e = \frac{b_e(3 + \sin\phi_e)}{6\cos\phi_e} = 10.52 \text{ MPa} \quad (5.21)$$

Knowing the strength parameters, the Paul-Mohr-Coulomb failure surface can be plotted in the $(\sigma_3 - \sigma_1)$ plane using Equations 2.49 to 2.51. The graph obtained, using the coefficients computed in Equations 5.22 to 5.25, is presented in Figure 5.7.

$$M_c = \frac{1 + \sin\phi_c}{1 - \sin\phi_c} = 2.11 \quad (5.22)$$

$$M_e = \frac{1 + \sin\phi_e}{1 - \sin\phi_e} = 2.08 \quad (5.23)$$

$$C_c = \frac{2c_c \cos\phi_c}{1 - \sin\phi_c} = 39.38 \text{ MPa} \quad (5.24)$$

$$C_e = \frac{2c_e \cos\phi_e}{1 - \sin\phi_e} = 30.31 \text{ MPa} \quad (5.25)$$

In the $(p - q)$ plane, the Paul-Mohr-Coulomb failure criterion is plotted using Equations 2.54 to 2.56, and the graph obtained in presented in Figure 5.8. These surfaces are expressed in terms of $b_{c,e}$, defined by Equations 5.15 and 5.17, and $m_{c,e}$ computes as follow:

$$m_c = \frac{6\sin\phi_c}{3 - \sin\phi_c} = 0.81 \quad (5.26)$$

$$m_e = \frac{6\sin\phi_e}{3 + \sin\phi_e} = 0.63 \quad (5.27)$$

Finally, the Paul-Mohr-Coulomb criterion is presented in the π -plane, obtained following the procedure described in Section 2.2.3. Figure 5.9 shows the failure criterion in the π -plane at different mean stresses p , corresponding to true-triaxial experiments mean stresses at failure (i.e. data points where $0^\circ < \theta < 60^\circ$ in Table 5.1).

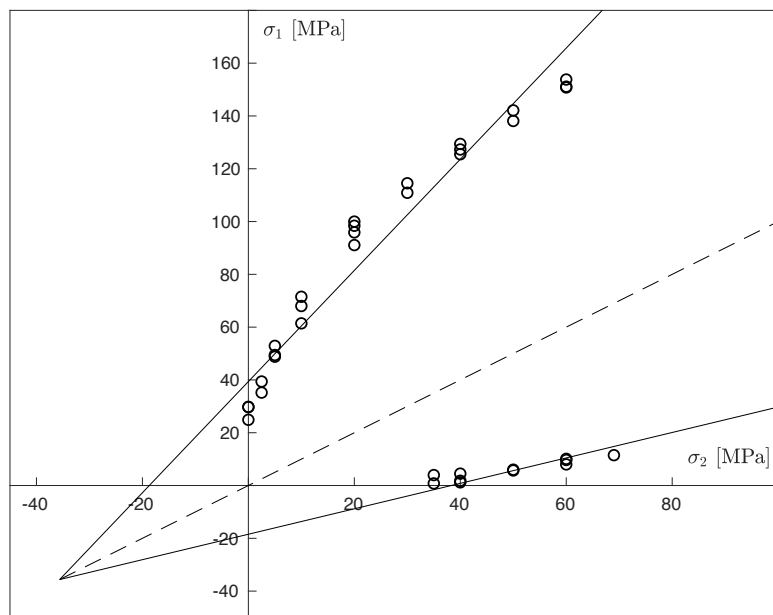


Figure 5.7: Paul-Mohr-Coulomb criterion failure surface in $(\sigma_3 - \sigma_1)$ plane

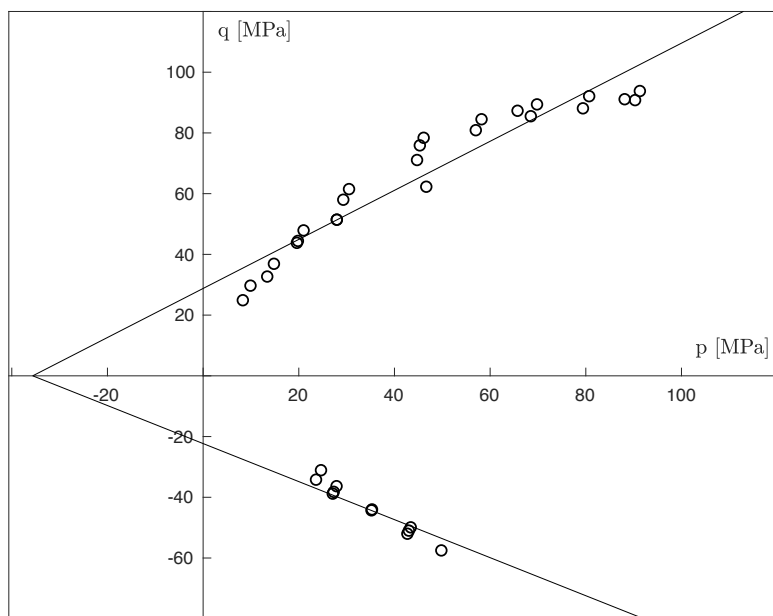


Figure 5.8: Paul-Mohr-Coulomb criterion failure surface in $(p - q)$ plane

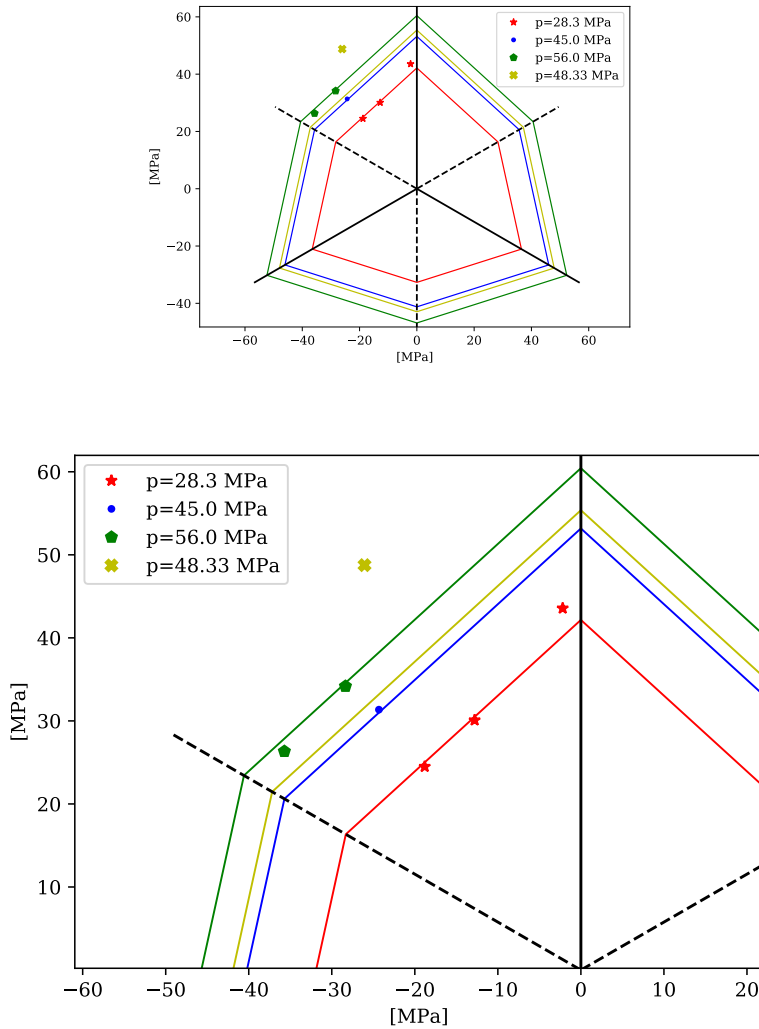


Figure 5.9: Paul-Mohr-Coulomb criterion failure surface in π -plane

The mean standard deviation misfit obtained with the Paul-Mohr-Coulomb failure criterion is 16.7 MPa.

5.2.4 Comparison of the failure criteria

The mean standard deviation misfits obtained for the three failure criteria show that Paul-Mohr-Coulomb provides a better approximation of the data points (Table 5.2). The three misfits values are very close and the observation of the fittings in the $(\sigma_3 - \sigma_1)$ and $(p - q)$ planes shows that the failure criteria provide similar approximations of the data points. However, in the π -plane the Paul-Mohr-Coulomb provide a better fitting of the true-triaxial data (Figure 5.9).

Table 5.2: Mean standard deviation misfits obtained for the three failure criteria

Criterion	Mean standard deviation misfit \bar{S} [MPa]
Mohr-Coulomb	17.7
Hoek-Brown	17.5
Paul-Mohr-Coulomb, 1 plane	16.7

Table 5.3: Parameters of the planes defining the failure surface of Paul-Mohr-Coulomb criterion

Plane	P1	P2
Friction angle in compression	$\phi_c^{(1)}$	$\phi_c^{(2)}$
Friction angle in extension	$\phi_e^{(1)}$	$\phi_e^{(2)}$
Theoretical uniaxial tensile strength	$V_0^{(1)}$	$V_0^{(2)}$

5.3 Paul-Mohr-Coulomb failure criterion with two planes

Published data from multi-axial experiments on multiple rocks showed that the failure envelop that describe them best is not linear over a large range of mean stress. However, popular failure theories as Mohr-Coulomb or Hoek-Brown, are either linear or do not provide an accurate prediction for all mean stresses. In this study, Paul-Mohr-Coulomb failure criteria is chosen to address this issue by approximating the nonlinear failure surface in a piecewise linear manner, resulting in a failure surface defined by six parameters.

5.3.1 Paul-Mohr-Coulomb with six parameters

The Paul-Mohr-Coulomb failure criterion presented in Section 5.2.3 is referred to as Paul-Mohr-Coulomb with three parameters and the failure surface is a plane defined by the general equation of the criterion (Equation 2.48) using V_0 , ϕ_c and ϕ_e . The Paul-Mohr-Coulomb failure surface defined in a piecewise manner is, therefore, made of a minimum of two planes, each expressed using three strength parameters, leading to the six parameters criterion.

The three parameter criterion describes a regular 6-sided pyramid in the principal stresses space (Section 2.1). By adding a plane to the failure surface, the six parameters criterion, therefore, describes two irregular 6-sided pyramids. Each plane is then defined by the parameters presented in Table 5.3, where $P2$ indicates the plane that approximate data points at low mean stress and $P1$ the ones at higher mean stress. Table 5.4 present four types of Paul-Mohr-Coulomb failure surfaces that can be defined according to the values of the parameters. For all types, the following conditions apply:

$$V_0^{(1)} > V_0^{(2)} \quad \text{and} \quad 0^\circ \leq \phi_{c,e}^{(i)} \leq 90^\circ \quad (5.28)$$

5.3. Paul-Mohr-Coulomb failure criterion with two planes

Table 5.4: Types of failure surfaces for the six parameters Paul-Mohr-Coulomb criterion

Type of failure surface	Parameters conditions
(i) 6-sided	$V_0^{(1)} = V_0^{(2)}$
(ii) 6-12-6 sided	$\phi_c^{(1)} < \phi_c^{(2)}, \phi_e^{(1)} < \phi_e^{(2)}, p_c \neq p_e$
(iii) 6-12 sided	$(\phi_c^{(1)} < \phi_c^{(2)}, \phi_e^{(1)} \geq \phi_e^{(2)})$ or $(\phi_c^{(1)} \geq \phi_c^{(2)}, \phi_e^{(1)} < \phi_e^{(2)})$
(iv) 6-12-6 sided	$\phi_c^{(1)} < \phi_c^{(2)}, \phi_e^{(1)} < \phi_e^{(2)}, p_c = p_e$

The complete graphical representation of the Paul-Mohr-Coulomb failure surface is composed of the $(p - q)$ plane, the $(\sigma_{II} - \sigma_I)$ plane, the π -plane and the principal stresses three-dimensional space. The transition between $P2$ and $P1$ is well represented in the $(p - q)$ plane, where they intersect on the compression side at the mean stress value p_c and on the extension side at p_e . In the case of the failure surface type (ii), these transitions points have different values leading to a 12 sided transition zone on the pyramid for mean stress values $p \in [p_c; p_e]$. Sketches of the 6-12-6 sided failure surface in different planes and in the three-dimensional space are presented in Figure 5.10, where the $(\sqrt{3}p - \sigma_1^*)$ plane is equivalent to the $(p - q)$ plane. More schematic representations and details on the four failure surfaces types are provided in Appendix D.

The inclusion of the intermediate stress in the Paul-Mohr-Coulomb equation (Equation 2.44) makes relevant the representation of the criterion in the $(\sigma_2 - \sigma_1)$ plane. Indeed, this plane presents the advantage to gather the data points for axisymmetric experiments, shown on compression and extension lines, as well as true-triaxial data in the same plot (Figure 5.11). The Paul-Mohr-Coulomb failure surfaces are plotted for a chosen value of σ_3 , using the following equation, based the rearrangement of Equation 2.44:

$$\sigma_I = \frac{1}{A} (1 - B\sigma_{II} - C\sigma_{III}) \quad (5.29)$$

5.3.2 2-plane fitting

The fitting of a six-parameter Paul-Mohr-Coulomb failure surface requires datasets for each plane. Once determined, these datasets are used for plane fitting, following the procedure presented in Section 2.3. This repartition of the data points into different planes is a challenging step of the failure criterion fitting, as it should give the optimal solution for the database considered.

One objective of this study was to create a program that automatically allocates data points to both planes, with the aim of getting a distribution that provides the best fitting for the Paul-

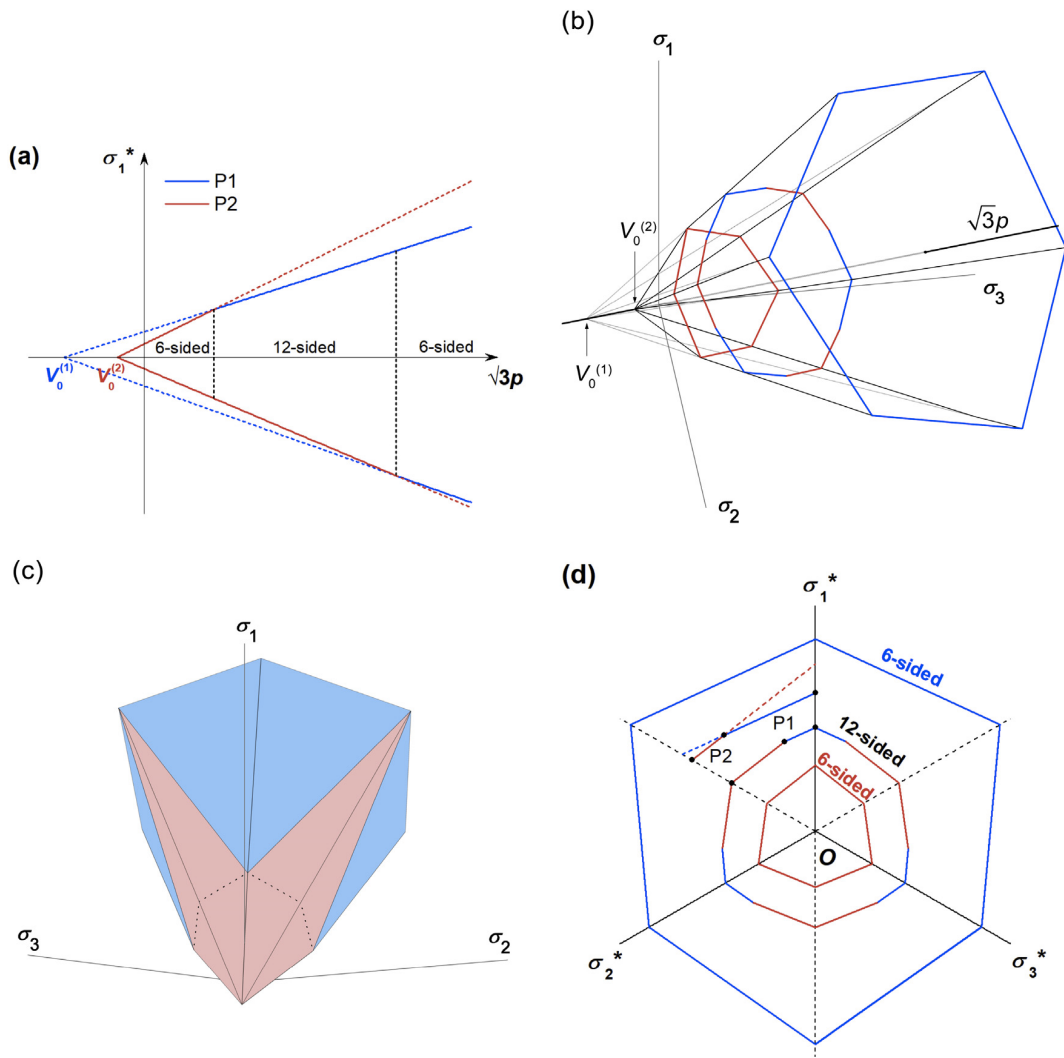


Figure 5.10: Paul-Mohr-Coulomb 6-12-6 sided failure surface graphical representations

5.3. Paul-Mohr-Coulomb failure criterion with two planes

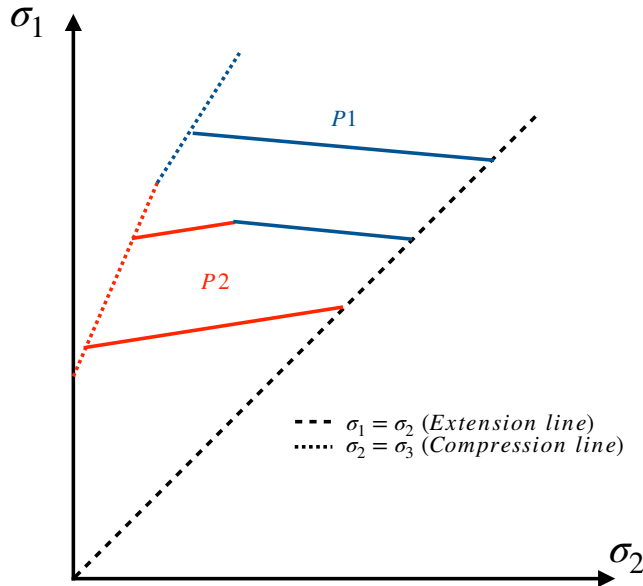


Figure 5.11: Paul-Mohr-Coulomb 6-12-6 sided failure surface in $(\sigma_{II} - \sigma_I)$ plane

Mohr-Coulomb criterion. Moreover, it was crucial that this program was developed not only for the rock tested in this study (i.e. Dunnville Sandstone), but for any rock with appropriate experimental data. This problem can be summarized by the following question:

How to automatize the allocation of data points into $P1$ or $P2$ in order to provide the most accurate fitting of the Paul-Mohr-Coulomb criterion ?

In the following paragraphs, the algorithm created to solve this problem is described.

Algorithm construction

The algorithm developed to solve the problem presented belongs to the *Brute-force* algorithm family. This category is based on the following principle: every possibility offered by the database is tried and the one that gives the best solution to the problem is selected. The amount of data available in the case of rock testing ($n_{max} \sim 50$) is small enough to use this type of algorithm without having issues related to efficiency.

In the case of this study, the algorithm will test all the possible variations of data allocations to the $P1$ or $P2$ datasets which can be created from the rock database. For each possible combination, planes $P1$ and $P2$ are created by the computation of their coefficient and fitting parameters defined for Paul-Mohr-Coulomb, following the procedure presented in 2.3. Then, the Mean Square Error (MSE), defined by Equation 5.31, is computed for each combination of datasets. Finally the data allocation variation that provides the minimal MSE is selected as the solution of the two planes fitting problem.

The algorithm proposed in this study can be apply to any rock testing database that contains results of the three principal stresses at failure (Table 5.1). Indeed, the rock database is the only input that is required to run this algorithm.

Computation of the mean square error

The error used in the computation of *MSE* is equal to the distance of a data point, defined by σ_I , σ_{II} and σ_{III} , from its fitted plane, defined by Equation 2.44:

$$err_i = A^{(j)}\sigma_I^i + B^{(j)}\sigma_{II}^i + C^{(j)}\sigma_{III}^i - 1 \quad (5.30)$$

where i is the index of the data point in the database and j indicates the plane number in which the data is allocated (i.e. $j = 1$ for $P1$ and $j = 2$ for $P2$). The Mean Square Error of a certain dataset combination k is then computed as follow:

$$MSE_k = \frac{1}{n} \sum_{i=1}^n err_i^2 \quad (5.31)$$

The dataset combination k that obtains the minimal *MSE* value provides the best fitting solution for Paul-Mohr-Coulomb failure surface for the considered rock.

Program resources

This algorithm was implemented in the programming language Python. The resources on the program developed to solve the two planes fitting problem are gathered in Appendix C. It contains the Python files required to run the program and a *README* document that explains how to use the program. Moreover, all the code files are commented in detail to ease their use and understanding.

5.3.3 Dunnville sandstone

The program presented in the previous section was applied to the experimental results database of Dunnville sandstone (cf. Table 5.1). The six-parameters Paul-Mohr-Coulomb failure surface obtained is presented in the following paragraphs through its representation in the $(p - q)$, $(\sigma_{II} - \sigma_I)$, π - planes and in the principal stresses three-dimensional space.

Strength parameters computation

The solution obtained from the least-square solution fitting describe in Chapter 2 (cf. Section 2.3, Equations 2.57 and 2.62) is presented in Table 5.5.

The strength parameters for Paul-Mohr-Coulomb failure criteria could be computed from Equations 2.61 to 2.65. The values obtained are gathered in Table 5.6.

Graphical representation of the failure surface

Knowing the strength parameters, the Paul-Mohr-Coulomb failure surface could be plotted in the $(p - q)$ plane using Equations 2.54 to 2.56 applied to each plane. The values of parameters $m_{c,e}$ and $c_{c,e}$ are presented in Table 5.7 and the $(p - q)$ plane plot is shown in Figure 5.12.

The failure surface can also be plotted in the $(\sigma_{II} - \sigma_I)$ plane. Equation 5.29 provides the planes equation in this coordinates system using the general expression of the Paul-Mohr-Coulomb criterion, which coefficients A , B and C are presented in Table 5.8. Figure 5.13 presents the six parameters failure surface for Dunnville sandstone in the $(\sigma_{II} - \sigma_I)$ plane.

The failure surface planes are also presented in the π -plane, obtained following the procedure described in Section 2.2.3. Figure 5.14 shows the failure criterion in the π -plane at different mean stresses p that correspond to true-triaxial experiments mean stresses at failure for $0^\circ < \theta < 60^\circ$ in Table 5.1. In addition, Figure 5.15 presents the projection of the $P_2, P_2 - P_1$ transition and P_1 pyramids on the π -plane.

Finally, Figure 5.16 shows the 6-12-6 sided pyramid obtained for Dunnville sandstone in the three-dimensional space.

A summary of the Paul-Mohr-Coulomb six parameters solution and the mean standard deviation misfits obtained for Dunnville Sandstone is presented in Table 5.9. The fittings provided by Mohr-Coulomb, Hoek-Brown, three and six parameters Paul-Mohr-Coulomb criteria can be compared using the mean standard deviation misfits values obtained (Table 5.2). The six parameter Paul-Mohr-Coulomb criterion provides the best prediction with the least mean standard deviation misfits for the two planes. This can be explained by the combination of the intermediate stress inclusion in the failure criterion general equation and the approximation of the failure surface non linearity, giving the most accurate states of stress prediction at failure. The observation of the six parameter Paul-Mohr-Coulomb and Hoek-Brown fittings in the $(p - q)$ and π - planes also presents for the first one a better approximation of the true-triaxial data points, but also of the axisymmetric ones, which was not the case with the three parameter Paul-Mohr-Coulomb.

The program developed for the Paul-Mohr-Coulomb criterion was generalized so that it can be used to fit of other rocks. A summary of the results obtained for rocks with available database from literature is provided in Appendix E.

Chapter 5. Analyses and Discussion

Table 5.5: $P1$ and $P2$ least-square solutions x for Dunnville sandstone

Plane	$x_1^{(i)}$	$x_2^{(i)}$	$x_3^{(i)}$
$P1$	0.54	-1.02	47.08
$P2$	1.39	-1.10	15.47

Table 5.6: $P1$ and $P2$ strength parameters for Dunnville sandstone

Plane	$b_c^{(i)}$ [MPa]	$b_e^{(i)}$ [MPa]	$V_0^{(i)}$ [MPa]	$\phi_c^{(i)}$ [°]	$\phi_e^{(i)}$ [°]
$P1$	47.1	34.1	86.9	14.4	12.1
$P2$	15.5	10.7	11.1	34.3	34.8

Table 5.7: $P1$ and $P2$ fitting parameters for Dunnville sandstone

Plane	$m_c^{(i)}$ [-]	$m_e^{(i)}$ [-]	$c_c^{(i)}$ [MPa]	$c_e^{(i)}$ [MPa]
$P1$	0.54	0.39	22.3	16.2
$P2$	1.39	0.96	7.61	5.26

Table 5.8: Paul-Mohr-Coulomb general equation coefficients for Dunnville sandstone

Plane	$A^{(i)}$	$B^{(i)}$	$C^{(i)}$
$P1$	1.74×10^{-2}	4.26×10^{-3}	-3.32×10^{-2}
$P2$	3.47×10^{-2}	-8.31×10^{-4}	-1.24×10^{-1}

Table 5.9: Summary of $P1$ and $P2$ strength parameters for Dunnville sandstone

Plane	$V_0^{(i)}$ [MPa]	$\phi_c^{(i)}$ [°]	$\phi_e^{(i)}$ [°]	\bar{S} [MPa]
$P1$	86.9	14.4	12.1	14.9
$P2$	11.1	34.3	34.8	6.11

5.3. Paul-Mohr-Coulomb failure criterion with two planes

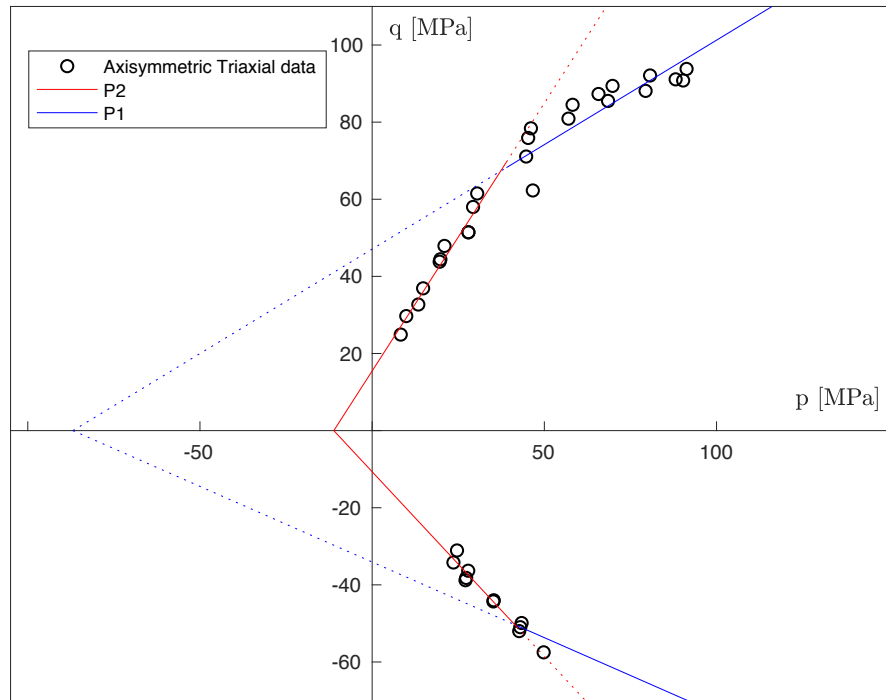


Figure 5.12: Paul-Mohr-Coulomb failure surface in the $(p - q)$ plane for Dunnville sandstone

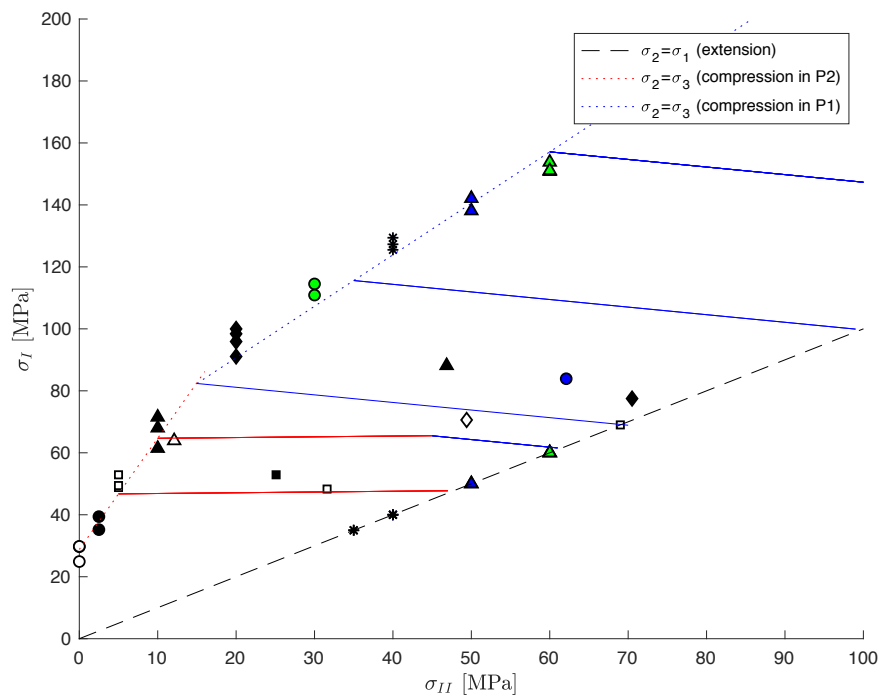


Figure 5.13: Paul-Mohr-Coulomb failure surface in the $(\sigma_{II} - \sigma_I)$ plane for Dunnville sandstone

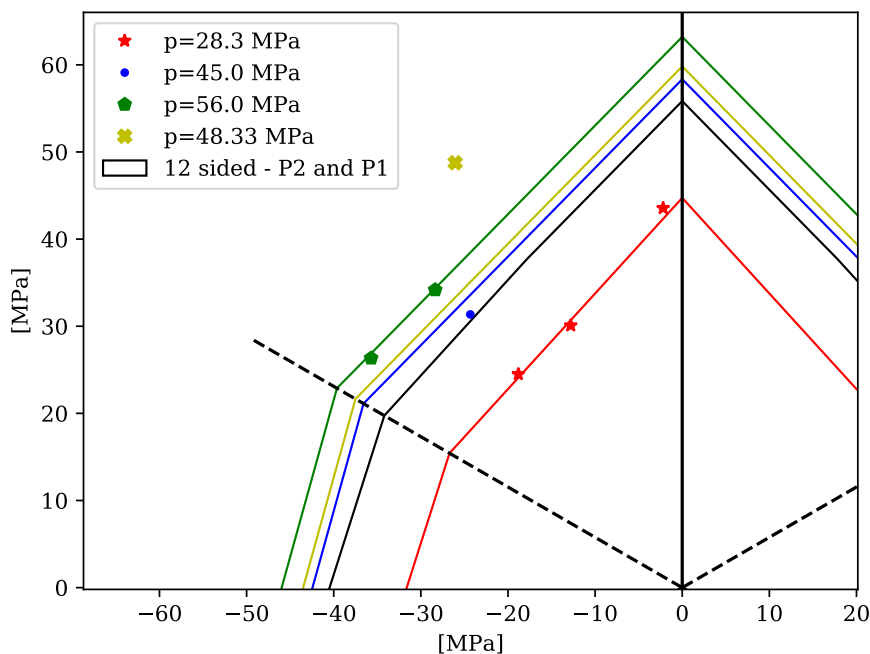


Figure 5.14: Paul-Mohr-Coulomb failure surface in the π -plane for Dunnville sandstone

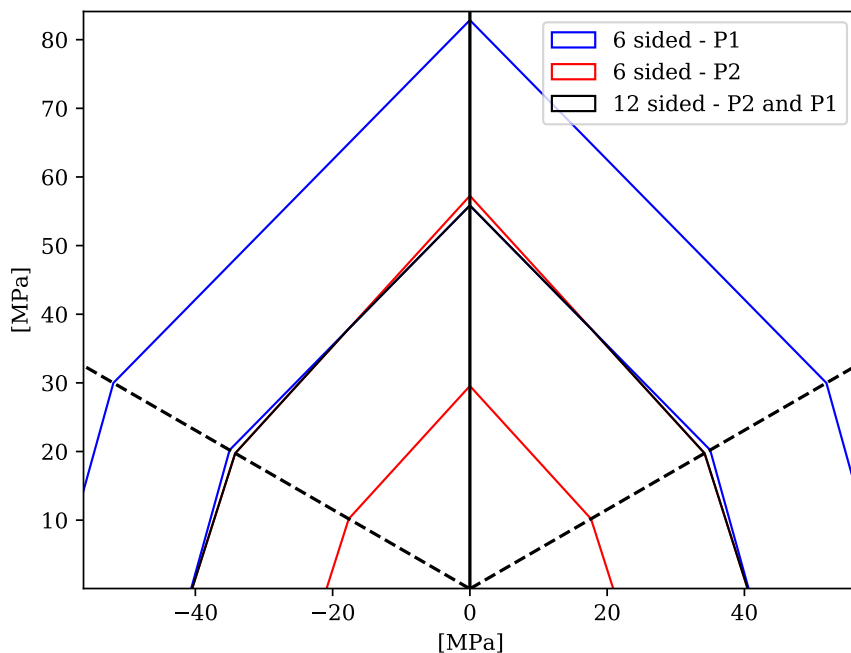


Figure 5.15: 6-12-6 sided pyramid projection in the π -plane for Dunnville sandstone

5.3. Paul-Mohr-Coulomb failure criterion with two planes

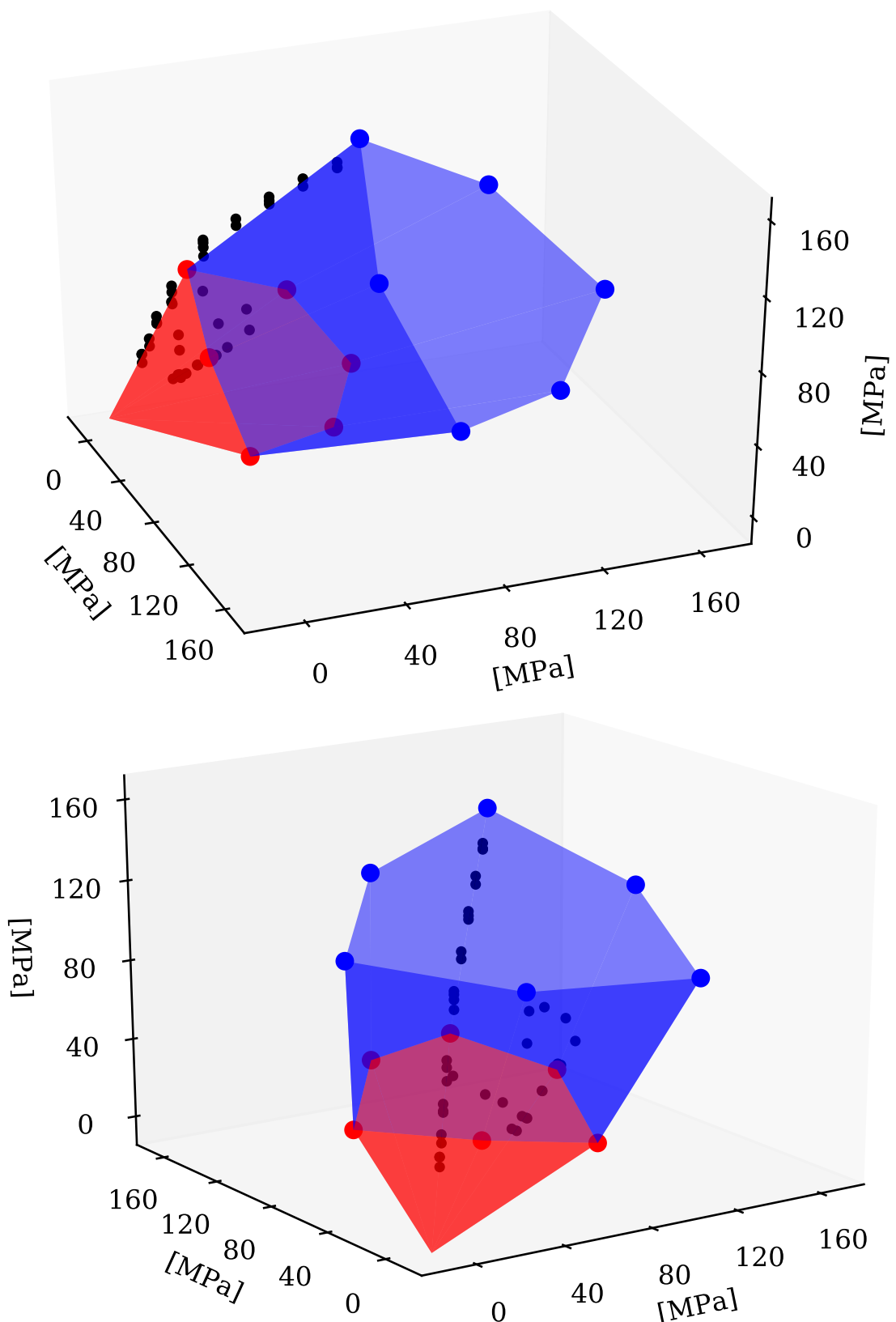


Figure 5.16: Paul-Mohr-Coulomb 6-12-6 sided failure surface pyramid for Dunnville sandstone

5.4 Simplified Paul-Mohr-Coulomb criterion

One criticism can be addressed to the Paul-Mohr-Coulomb failure criterion regarding the amount of experiments required to construct the two plane failure surface. Indeed, in order to build the failure surface of the three-parameter Paul-Mohr-Coulomb criterion, at least three data points are needed, leading to a requirement of six points for the six parameters criterion. These six data points corresponds to the same number of experiments, ideally of different procedures, that is needed to be performed on the same rock. By carrying out this study in a well equipped research environment, it was possible to perform multiple experiments under different conditions. However, this is hardly the case in the majority of rock mechanics and geoengineering applications for which that amount of data is not always available.

This simplified Paul-Mohr-Coulomb criterion is based on the assumption of a limited amount of data available, that are obtained from axisymmetric compression experiments. These data are used to fit the piecewise linear failure envelop in compression, and the one in extension is built by making the following simplification on the friction angles:

$$\phi_e^{(1)} = \phi_c^{(1)} = \phi^{(1)} \quad \text{for } P1 \quad (5.32)$$

$$\phi_e^{(2)} = \phi_c^{(2)} = \phi^{(2)} \quad \text{for } P2 \quad (5.33)$$

The failure surface is then defined by two planes built using four parameters, hence the name of the simplified or four-parameter Paul-Mohr-Coulomb failure criterion.

This simplified Paul-Mohr-Coulomb criterion fitting was performed for Dunnville sandstone, using only six axisymmetric compression data from the database (Table 5.1) that covers a large range of mean stresses. The selected data are presented in Table 5.10. The parameters obtained from this fitting and the ones computed using the condition defined in Equation 5.32 are presented in Table 5.11.

Table 5.10: Data selected to fit the simplified Paul-Mohr-Coulomb failure criterion

Test	Bedding	σ_I [MPa]	σ_{II} [MPa]	σ_{III} [MPa]	p [MPa]	q [MPa]	θ [$^\circ$]
Published TC-2	\perp	39.4	2.5	2.5	14.8	36.9	0
Published TC-3	\perp	52.9	5.0	5.0	21.0	47.9	0
Published TC-4	\perp	71.5	10.0	10.0	30.5	61.5	0
Published TC-6	\perp	114.5	30.0	30.0	58.2	84.5	0
Published TC-7	\perp	129.4	40.0	40.0	69.8	89.4	0
Published TC-8	\perp	142.1	50.0	50.0	80.7	92.1	0

In order to compare and assess the quality of this fitting, the Mohr-Coulomb and Hoek-Brown

5.4. Simplified Paul-Mohr-Coulomb criterion

Table 5.11: $P1$ and $P2$ strength parameters for Dunnville sandstone obtained from the simplified Paul-Mohr-Coulomb criterion fitting

Plane	$V_0^{(i)}$ [MPa]	$\phi_c^{(i)}$ [$^\circ$]	$\phi_e^{(i)}$ [$^\circ$]
$P1$	192.2	9.2	9.2
$P2$	9.25	38.1	38.1

failure surfaces were also fitted using only the selected data:

$$\text{Mohr-Coulomb criterion: } K_p = 2.12 \quad \text{and} \quad C_0 = 43.09 \quad (5.34)$$

$$\text{Hoek-Brown criterion: } m = 3.65 \quad \text{and} \quad C_0 = 41.40 \quad (5.35)$$

The mean standard deviation misfit for the three criteria were computed only using the non-fitted data (data not used for the failure surface fitting). For the simplified Paul-Mohr-Coulomb criterion, these data needed to be allocated to one plane of the piecewise failure surface. This was done by computing the perpendicular distances from one data point to each plane, and selecting the smaller one. The obtained mean standard deviation misfits are presented in Table 5.12, where for Paul-Mohr-Coulomb it is computed as the mean of the values obtained for $P1$ and $P2$.

Table 5.12: Mean standard deviation misfits obtained for the three failure criteria

Criterion	Mean standard deviation misfit \bar{S} [MPa]
Mohr-Coulomb	18.6
Hoek-Brown	17.5
Four-parameter Paul-Mohr-Coulomb	11.8

The four-parameter Paul-Mohr-Coulomb criterion shows the smallest misfit compared to the other two. Moreover, the simplified Paul-Mohr-Coulomb misfit is close to the one obtained from the six-parameter Paul-Mohr-Coulomb criterion. Again, this confirms that the Paul-Mohr-Coulomb can provide the most accurate failure surface, even in the case of a limited amount of data available and the inclusion of a restrictive condition. It should, however, be noted that in the case of Dunnville sandstone, this simplified criterion does not give a good approximation of the multi-axial data at high mean stress. Moreover, the Mohr-Coulomb and Hoek-Brown failure surfaces provide a more accurate fitting of these data. This is due to the high value of mean stress at which $P1$ and $P2$ intercept in the $(p - q)$ plane that leads to the allocation of the majority of the non-fitted data to $P2$, and $P1$ to be almost exclusively made of compression data.

5.5 Discussion

The previous sections provide a comparison of the four failure criteria principally based on the computation of the mean standard deviation misfits \bar{S} . This quantitative comparison indicator is based on the computation of the error between the predicted and real values of the major stress, and report the precision of the prediction provided by a failure criterion. Another comparison could also be relative to the failure surface. Indeed, a rigorous evaluation of a failure criterion can be made by the computation of the distance between a data point and the failure surface. This type of error computation was used in this work in the *Brute-force* algorithm developed for the six parameters Paul-Mohr-Coulomb fitting (Section 5.3.2). In this case, as well as for Mohr-Coulomb, the computation of the "point-plane" distance is made possible and convenient thanks to the explicit general equation of the planes that forms the failure surface. However, in the case of Hoek-Brown and other criteria defined by implicit equations, it becomes challenging to go through the mathematical derivations required to compute this distance. An interesting addition to this work would be to look at all the criteria evaluated here from the point of view of the "data-failure surface" distance, and to compare the quantitative indicators of their accuracy.

On the π -plane representations of the failure criteria (Figure 5.14) the data point of the true-triaxial experiment under plane strain condition (i.e. $p = 48.3$ MPa) presents an outlier from the failure surface, and also from the "alignment" or "group" of other true-triaxial data (mainly performed under constant mean stress). The experiments from previous work (published data in Table 5.1) may have been performed on specimens from a different block of rock than the one used for the tests presented in this study. Therefore, it is possible that the specimen used for the plane strain test had different properties, leading to this outlier.

The comparison of the three failure criteria revealed the importance of taking into account the intermediate stress in their formulation. First, the evaluation of the Mohr-Coulomb and Paul-Mohr-Coulomb indicates that even with the use of a linear criterion to approximate a non-linear failure surface, the one defined by a general equation in terms of the three principal stresses gives a better approximation of the data points. Moreover, the comparison between the Hoek-Brown and Paul-Mohr-Coulomb fittings reveals that a linear criterion that takes into account σ_{II} gives a better fitting of the data from true-triaxial experiments, which is more representative of in-situ conditions.

6 Conclusion

The purpose of this study was to evaluate the Mohr-Coulomb, Hoek-Brown and Paul-Mohr-Coulomb failure criteria by analyzing the results of multi-axial experiments performed on Dunnville sandstone.

A review of the three failure criteria was provided, and the three were described in different coordinates systems: the $(p - q)$, $(\sigma_3 - \sigma_1)$ and π - planes. The strength parameters used are the frictions angles in compression ϕ_c and in extension ϕ_e , the theoretical isotropic tensile strength V_0 , the uniaxial compressive strength C_0 and the fitting parameter m . The parameters for the Mohr-Coulomb and Hoek-Brown failure criteria were based on the results of axisymmetric triaxial compression experiments, and these two do not include the intermediate stress σ_{II} in their formulation. The three parameter Paul-Mohr-Coulomb failure criterion is defined by the three principal stresses, and its parameters were computed with the results of all multi-axial data, using a fitting method based on the least squares approach.

Dunnville sandstone was used as a representative rock with known geological history and mineralogy, and its behavior under uniaxial and multi-axial testing was observed by performing appropriate experiments. To investigate the intermediate stress effect on rock failure, two true-triaxial experiments under different stress paths were performed using the University of Minnesota Plane-Strain Apparatus. The addition of pistons enabling the direct application of the intermediate stress (σ_{II}) gave the possibility to perform a true-triaxial experiment with a plane strain testing condition ($\epsilon_2 = 0$).

The results of the experiments performed in the scope of this study enriched the available data on Dunnville sandstone, and were gathered with results published in the literature. This database was then used to evaluate the Mohr-Coulomb, Hoek-Brown and three parameter Paul-Mohr-Coulomb failure criteria. Their comparison, based on the least mean standard deviation misfit, showed that the three parameter Paul-Mohr-Coulomb provided the best prediction and fitting of the experimental data, due to the inclusion of the intermediate stress and the definition of different frictions angles for compression and extension.

Chapter 6. Conclusion

The Paul-Mohr-Coulomb failure criterion was further investigated by evaluating its accuracy using a failure surface described by two planes instead of one, leading to a six parameter Paul-Mohr-Coulomb failure criterion. The failure criterion fitting was enabled by the development of a algorithm, that automatically allocated the data to the failure surface (either plane 1 or 2) that minimizes the mean squared error of the distance between the two-plane failure surface and the data points. This program was generalized to enable its use for any rock with available results of multi-axial strength experiments.

The evaluation showed that Paul-Mohr-Coulomb with six parameters (two planes) provides the most accurate prediction and fitting of the failure surface.

Future work

As the evaluation of the failure criteria is based on the multi-axial experiments, the improvement of database is crucial. It is recommended that multi-axial experiments continue, where all three principal stresses at failure are known. Interesting stress states that need further investigation include true-triaxial experiments under (i) plane strain condition or (ii) constant mean stress and constant Lode angle. Moreover, the presented experiments could also be extended to fluid-saturated rock, by introducing fluid pressure in multi-axial testing.

A Notations

The following symbols are used in the thesis:

A, B, C	material parameters used for Paul-Mohr-Coulomb failure criterion
b	width of the prismatic specimen
b_c	intercept of axisymmetric compression line in $(p - q)$ plane
b_e	intercept of axisymmetric extension line in $(p - q)$ plane
C_0	uniaxial compressive strength
c	cohesion
d	cylindrical specimen diameter
E	Young's modulus
err	distance between a data point and its fitted plane
h	specimen height
I_1	first invariant of stress state
J_2	second invariant of stress state
J_3	third invariant of stress state
k	slope of Paul-Mohr-Coulomb failure line in π -plane
K_p	slope of the Mohr-Coulomb failure line in $(\sigma_3 - \sigma_1)$ plane
L	length of the prismatic specimen
M_c	slope of the Paul-Mohr-Coulomb compression line in $(\sigma_3 - \sigma_1)$ plane
M_e	slope of the Paul-Mohr-Coulomb extension line in $(\sigma_3 - \sigma_1)$ plane
MSE	mean square error
m	parameter for Hoek-Brown criterion
m_c	slope of the axisymmetric compression line in the $(p - q)$ plane
m_e	slope of the axisymmetric extension line in the $(p - q)$ plane
p	mean stress
p_c	mean stress of P1 and P2 intersection point in $(p - q)$ plane for compression
p_e	mean stress of P1 and P2 intersection point in $(p - q)$ plane for extension
$P1$	plane 1
$P2$	plane 2
q	deviatoric stress
q_c	deviatoric stress for triaxial compression
q_e	deviatoric stress for triaxial extension

Appendix A. Notations

S_{ij}	deviator stress
\bar{S}	mean standard deviation misfit
s_i	standard deviation of the tests series i
V_0	theoretical isotropic tensile strength
$V_0^{(1)}$	theoretical isotropic tensile strength for P1
$V_0^{(2)}$	theoretical isotropic tensile strength for P2
V_P	P-wave speed
x_1, x_2, x_3	component of the vector solution from least-square fitting
α	b_c/b_e
δ_{ij}	Kronecker delta
ϵ_{II}	intermediate principal strain
ϵ_a	axial strain
ϵ_l	lateral strain
ϕ	friction angle
$\phi^{(1)}$	friction angle for P1
$\phi^{(2)}$	friction angle for P2
ϕ_c	friction angle for axisymmetric compression
$\phi_c^{(1)}$	compression friction angle for P1
$\phi_c^{(2)}$	compression friction angle for P2
ϕ_e	friction angle for axisymmetric extension
$\phi_e^{(1)}$	extension friction angle for P1
$\phi_e^{(2)}$	extension friction angle for P2
v	Poisson's ratio
θ	Lode angle (angle from σ_1^* in the π -plane)
ρ	dry density
σ	normal stress
σ_a	axial stress
σ_r	radial stress
σ_{ij}	stress component
$\sigma_{1,2}$	stress at the end of phase 1 of the constant mean stress true-triaxial experiment
$\sigma_I, \sigma_{II}, \sigma_{III}$	major, intermediate and minor principal stresses
$\sigma_1, \sigma_2, \sigma_3$	principal stresses with no regard to magnitude
$\sigma_1^*, \sigma_2^*, \sigma_3^*$	projection of the principal stress axes in π -plane
$\sigma_{I,j}^{test}$	major stress of data point j
$\sigma_{I,j}^{calc}$	predicted major stress
τ	shear stress

B Failure criterion formulation in π -plane

The principal stresses, with no consideration for magnitude, are formulated in the π -plane as follow:

$$\sigma_1 = p + \frac{\sqrt{6}}{3}r \cos(\theta) \quad (\text{B.1})$$

$$\sigma_2 = p - \frac{\sqrt{6}}{3}r \sin\left(\frac{\pi}{6} - \theta\right) \quad (\text{B.2})$$

$$\sigma_3 = p - \frac{\sqrt{6}}{3}r \sin\left(\frac{\pi}{6} + \theta\right) \quad (\text{B.3})$$

Mohr-Coulomb failure criterion

The Mohr-Coulomb failure criterion is expressed in terms of the principal stresses σ_I and σ_{III} :

$$\sigma_I = K_p \sigma_{III} + C_0 \quad (\text{B.4})$$

The formulation of the criterion in the π -plane is defined bellow for each possible ordering of stresses. On this plane, a point is at a distance r from the origin of the hydrostatic axis and oriented at the Lodge angle θ from the σ_1^* axis.

Section (i) : $\sigma_I = \sigma_1$, $\sigma_{II} = \sigma_2$ and $\sigma_{III} = \sigma_3$

$$rcos\theta = \frac{6}{2\sqrt{6} + \sqrt{6}K_p} \left[p(K_p - 1) - \frac{\sqrt{2}}{2}K_p r sin\theta + C_0 \right] \quad (\text{B.5})$$

Section (ii) : $\sigma_I = \sigma_2$, $\sigma_{II} = \sigma_1$ and $\sigma_{III} = \sigma_3$

$$rcos\theta = \frac{6}{K_p\sqrt{6} - \sqrt{6}K_p} \left[p(K_p - 1) - \frac{\sqrt{2}}{2}r sin\theta(1 + K_p) + C_0 \right] \quad (\text{B.6})$$

Appendix B. Failure criterion formulation in π -plane

Section (iii) : $\sigma_I = \sigma_2$, $\sigma_{II} = \sigma_3$ and $\sigma_{III} = \sigma_1$

$$rcos\theta = \frac{6}{2\sqrt{6} + \sqrt{6}K_p} \left[p(K_p - 1) + \frac{\sqrt{2}}{2} r sin\theta - C_0 \right] \quad (\text{B.7})$$

Section (iv) : $\sigma_I = \sigma_3$, $\sigma_{II} = \sigma_2$ and $\sigma_{III} = \sigma_1$

$$rcos\theta = \frac{6}{2\sqrt{6} + \sqrt{6}K_p} \left[p(K_p - 1) - \frac{\sqrt{2}}{2} r sin\theta - C_0 \right] \quad (\text{B.8})$$

Section (v) : $\sigma_I = \sigma_3$, $\sigma_{II} = \sigma_1$ and $\sigma_{III} = \sigma_2$

$$rcos\theta = \frac{6}{K_p\sqrt{6} - \sqrt{6}K_p} \left[p(K_p - 1) + \frac{\sqrt{2}}{2} r sin\theta(1 + K_p) + C_0 \right] \quad (\text{B.9})$$

Section (vi) : $\sigma_I = \sigma_1$, $\sigma_{II} = \sigma_3$ and $\sigma_{III} = \sigma_2$

$$rcos\theta = \frac{6}{2\sqrt{6} + \sqrt{6}K_p} \left[p(K_p - 1) + K_p \frac{\sqrt{2}}{2} r sin\theta + C_0 \right] \quad (\text{B.10})$$

Hoek-Brown failure criterion

The Hoek-Brown failure criterion is expressed in terms of the principal stresses σ_I and σ_{III} :

$$\sigma_I = \sigma_{III} + C_0 \sqrt{\frac{m}{C_0} \sigma_{III} + 1} \quad (\text{B.11})$$

The formulation of the criterion in the π -plane is defined bellow for each possible ordering of stresses. On this plane, a point is at a distance r from the origin of the hydrostatic axis and oriented at the Lodge angle θ from the σ_1^* axis.

Section (i) : $\sigma_I = \sigma_1$, $\sigma_{II} = \sigma_2$ and $\sigma_{III} = \sigma_3$

$$rcos\theta = \frac{2}{\sqrt{6}} \left[-\frac{\sqrt{2}}{2} r sin\theta + C_0 \sqrt{\frac{m}{C_0} \left(p - \frac{\sqrt{6}}{6} r cos\theta - \frac{\sqrt{2}}{2} r sin\theta \right) + 1} \right] \quad (\text{B.12})$$

Section (ii) : $\sigma_I = \sigma_2$, $\sigma_{II} = \sigma_1$ and $\sigma_{III} = \sigma_3$

$$rcos\theta = \sqrt{6} \left[p - \frac{\sqrt{2}}{2} r sin\theta + \frac{C_0^2 - 2r^2 sin^2\theta}{C_0 m} \right] \quad (\text{B.13})$$

Section (iii) : $\sigma_I = \sigma_2$, $\sigma_{II} = \sigma_3$ and $\sigma_{III} = \sigma_1$

$$rcos\theta = \frac{2}{\sqrt{6}} \left[\frac{\sqrt{2}}{2} rsin\theta - C_0 \sqrt{\frac{m}{C_0} \left(p + \frac{\sqrt{6}}{3} rcos\theta \right) + 1} \right] \quad (\text{B.14})$$

Section (iv) : $\sigma_I = \sigma_3$, $\sigma_{II} = \sigma_2$ and $\sigma_{III} = \sigma_1$

$$rcos\theta = \frac{2}{\sqrt{6}} \left[-\frac{\sqrt{2}}{2} rsin\theta - C_0 \sqrt{\frac{m}{C_0} \left(p + \frac{\sqrt{6}}{3} rcos\theta \right) + 1} \right] \quad (\text{B.15})$$

Section (v) : $\sigma_I = \sigma_3$, $\sigma_{II} = \sigma_1$ and $\sigma_{III} = \sigma_2$

$$rcos\theta = \sqrt{6} \left[p + \frac{\sqrt{2}}{2} rsin\theta + \frac{C_0^2 - 2r^2 sin^2\theta}{C_0 m} \right] \quad (\text{B.16})$$

Section (vi) : $\sigma_I = \sigma_1$, $\sigma_{II} = \sigma_3$ and $\sigma_{III} = \sigma_2$

$$rcos\theta = \frac{2}{\sqrt{6}} \left[\frac{\sqrt{2}}{2} rsin\theta + C_0 \sqrt{\frac{m}{C_0} \left(p - \frac{\sqrt{6}}{6} rcos\theta + \frac{\sqrt{2}}{2} rsin\theta \right) + 1} \right] \quad (\text{B.17})$$

Paul-Mohr-Coulomb failure criterion

The Paul-Mohr-Coulomb failure criterion is expressed in terms of the principal stresses σ_I , σ_{II} and σ_{III} :

$$A\sigma_I + B\sigma_{II} + C\sigma_{III} = 1 \quad (\text{B.18})$$

The formulation of the criterion in the π -plane is defined below for each possible ordering of stresses. On this plane, a point is at a distance r from the origin of the hydrostatic axis and oriented at the Lodge angle θ from the σ_1^* axis.

Section (i) : $\sigma_I = \sigma_1$, $\sigma_{II} = \sigma_2$ and $\sigma_{III} = \sigma_3$

$$rcos\theta = \frac{6}{\sqrt{6}(2A - B - C)} \left[1 - p(A + B + C) - \frac{\sqrt{2}}{2} rsin\theta(B + C) \right] \quad (\text{B.19})$$

Appendix B. Failure criterion formulation in π -plane

Section (ii) : $\sigma_I = \sigma_2$, $\sigma_{II} = \sigma_1$ and $\sigma_{III} = \sigma_3$

$$rcos\theta = \frac{6}{\sqrt{6}(2B - A - C)} \left[1 - p(A + B + C) + \frac{\sqrt{2}}{2} r sin\theta(C - A) \right] \quad (\text{B.20})$$

Section (iii) : $\sigma_I = \sigma_2$, $\sigma_{II} = \sigma_3$ and $\sigma_{III} = \sigma_1$

$$rcos\theta = \frac{6}{\sqrt{6}(2C - A - B)} \left[1 - p(A + B + C) + \frac{\sqrt{2}}{2} r sin\theta(B - A) \right] \quad (\text{B.21})$$

Section (iv) : $\sigma_I = \sigma_3$, $\sigma_{II} = \sigma_2$ and $\sigma_{III} = \sigma_1$

$$rcos\theta = \frac{6}{\sqrt{6}(2C - B - A)} \left[1 - p(A + B + C) + \frac{\sqrt{2}}{2} r sin\theta(A - B) \right] \quad (\text{B.22})$$

Section (v) : $\sigma_I = \sigma_3$, $\sigma_{II} = \sigma_1$ and $\sigma_{III} = \sigma_2$

$$rcos\theta = \frac{6}{\sqrt{6}(2B - A - C)} \left[1 - p(A + B + C) + \frac{\sqrt{2}}{2} r sin\theta(A - C) \right] \quad (\text{B.23})$$

Section (vi) : $\sigma_I = \sigma_1$, $\sigma_{II} = \sigma_3$ and $\sigma_{III} = \sigma_2$

$$rcos\theta = \frac{6}{\sqrt{6}(2A - B - C)} \left[1 - p(A + B + C) + \frac{\sqrt{2}}{2} r sin\theta(B - C) \right] \quad (\text{B.24})$$

C Fitting program

The resources of the program developed for failure criteria fitting are available at the following address: <https://github.com/hfuselier/PDM/tree/master/python>.

Its objective is to provide a fitting solution and representations of the failure surface in a three-dimensional space and in the π -plane for the Paul-Mohr-Coulomb failure criterion. The development of the program was considered to enable the fitting of the three-parameter, six-parameter and simplified Paul-Mohr-Coulomb criterion. The ".README.pdf" file explains how to use the program for the evaluation of the Paul-Mohr-Coulomb failure criterion and its comparison with the Mohr-Coulomb and Hoek-Brown failure criteria.

The files gather in the "python" folder are organized as presented in Table C.1.

Table C.1: Organization of the program

Application	Associated files
Paul-Mohr-Coulomb with three parameters	<i>pmc.py,</i> <i>brute_force.py,</i> <i>error_computation.py,</i> <i>Plot_one_plane.ipynb</i>
Paul-Mohr-Coulomb with six parameters	<i>pmc.py,</i> <i>brute_force.py,</i> <i>error_computation.py,</i> <i>Plot_3D_6-12-6.ipynb</i>
Simplified Paul-Mohr-Coulomb	<i>pmc_4p.py,</i> <i>brute_force_4p.py,</i> <i>error_computation_4p.py,</i> <i>Plot_3D_6-12-6.ipynb</i>

Appendix C. Fitting program

Application	Associated files
Mohr-Coulomb fitting with all data	<i>mc.py,</i> <i>error_computation.py,</i> <i>Plot_one_plane.ipynb</i>
Hoek-Brown fitting with all data	<i>hb.py,</i> <i>error_computation.py,</i> <i>Plot_one_plane.ipynb</i>
Mohr-Coulomb fitting with six data	<i>mc.py,</i> <i>error_computation_4p.py,</i> <i>Plot_one_plane.ipynb</i>
Hoek-Brown fitting with six data	<i>hb.py,</i> <i>error_computation_4p.py,</i> <i>Plot_one_plane.ipynb</i>

D Paul-Mohr-Coulomb failure surface

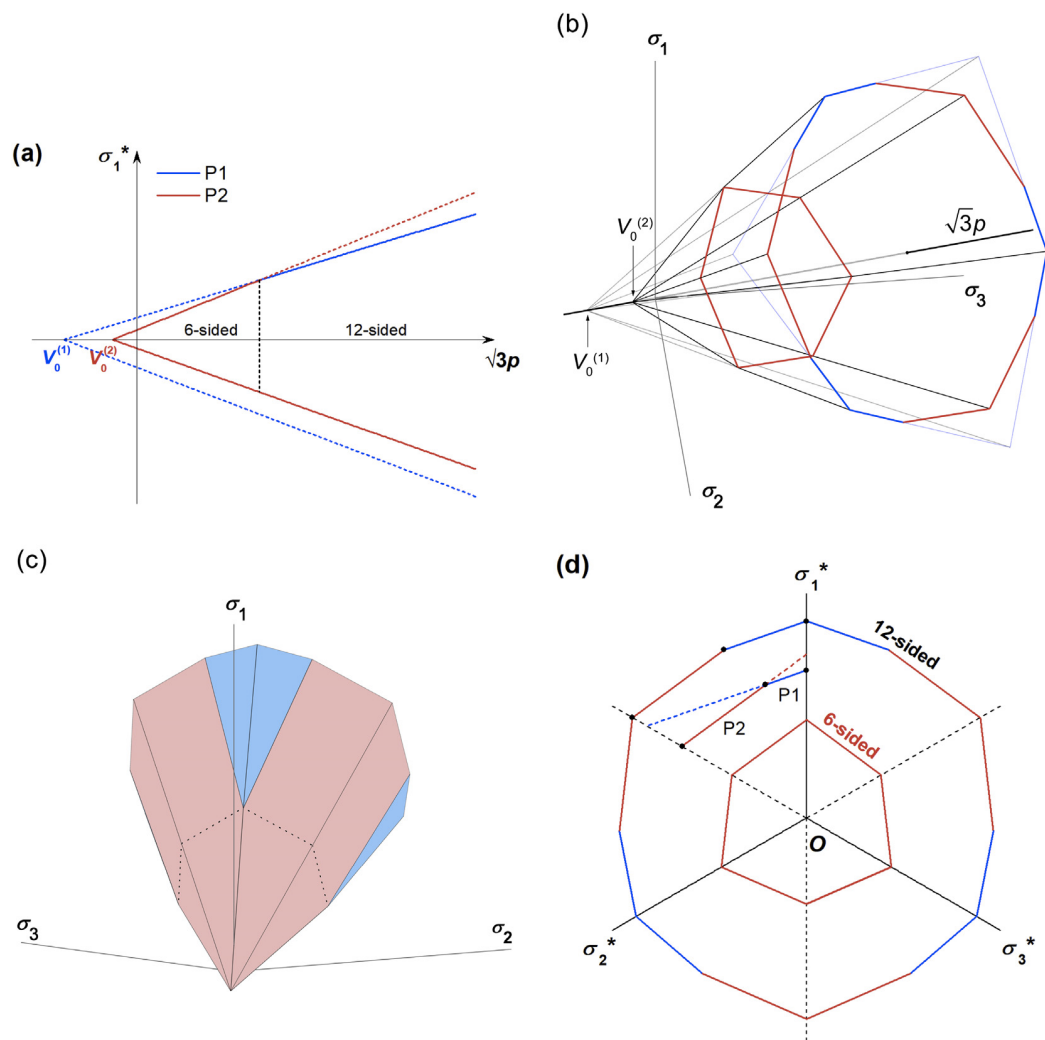


Figure D.1: Paul-Mohr-Coulomb 6-12 sided failure surface graphical representations from Labuz et al. (2018) [1]

Appendix D. Paul-Mohr-Coulomb failure surface

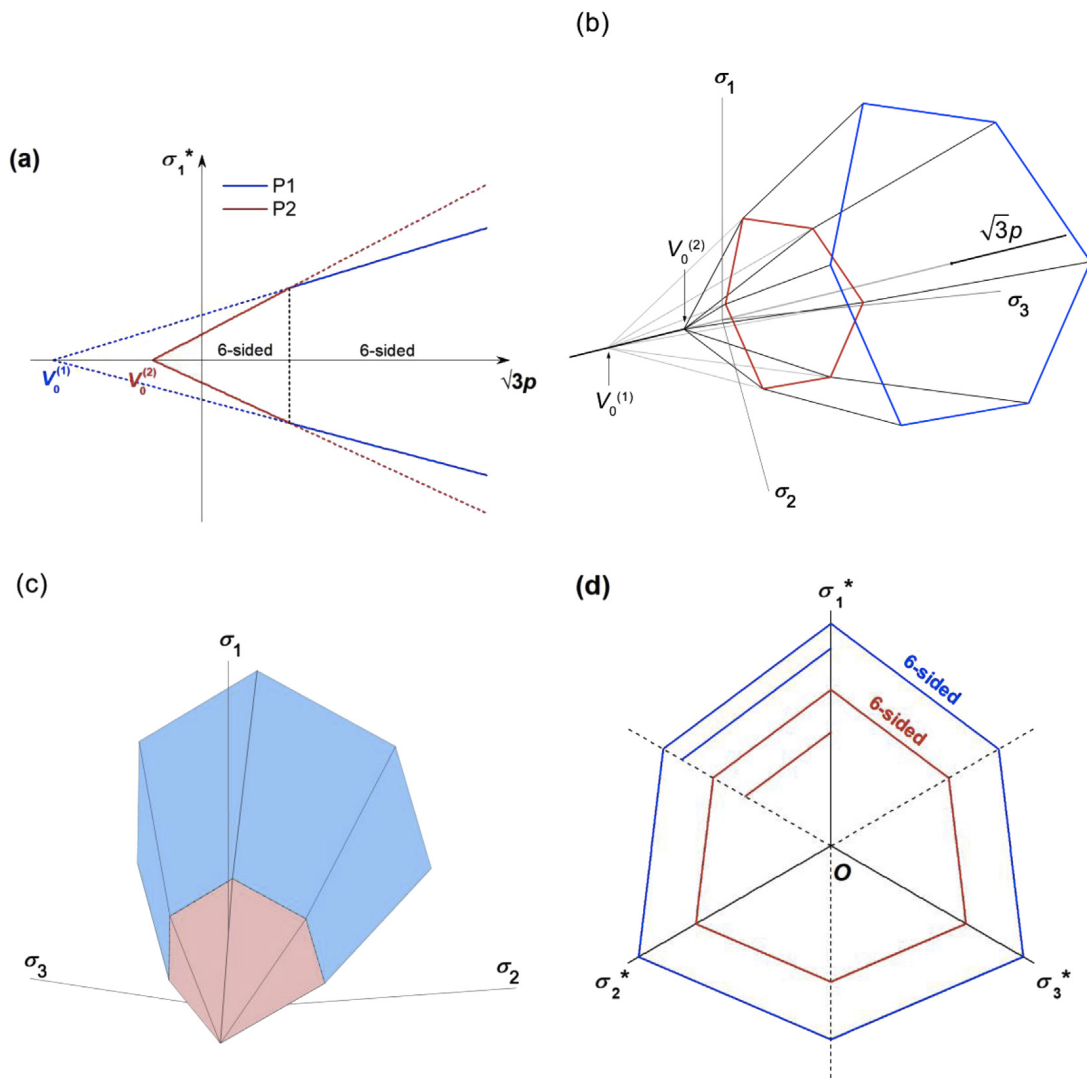


Figure D.2: Paul-Mohr-Coulomb 6-6 sided failure surface graphical representations from Labuz et al. (2018) [1]

E Paul-Mohr-Coulomb failure criteria for rocks from literature

The Paul-Mohr-Coulomb failure criterion was evaluated for rocks with published data (from Labuz et al. (2018) [1]) that provide a 6-12-6 failure surface. The obtained results are presented in Table E.1.

Table E.1: Values of the six PMC parameters for selected rock with a 6-12-6 sided failure surface

Rock	$V_0^{(1)}$ [MPa]	$\phi_c^{(1)}$ [°]	$\phi_e^{(1)}$ [°]	$V_0^{(2)}$ [MPa]	$\phi_c^{(2)}$ [°]	$\phi_e^{(2)}$ [°]
Darley Dale sandstone	76.3	30.9	32.2	18.3	44.9	48.4
Berea sandstone	84.1	28.3	25.9	13.2	47.7	53.0
Indiana limestone	31.0	27.2	28.1	9.68	43.9	44.3
Taiwan siltstone	61.3	28.8	28.9	10.5	48.4	39.8
Coconino sandstone	50.7	36.8	36.8	7.81	53.3	55.1
Bentheim sandstone	27.3	33.5	34.5	9.44	37.7	43.1

Bibliography

- [1] J. F. Labuz, F. Zeng, R. Makhnenko, and Y. Li, "Brittle failure of rock: A review and general linear criterion," *Journal of Structural Geology*, vol. 112, pp. 7–28, jul 2018. doi: 10.1016/j.jsg.2018.04.007
- [2] A. Tarokh, "Poro-elastic response of saturated rock." phdthesis, Department of Civil, Environmental and Geo-Engineering, University of Minnesota, 2016, p.71.
- [3] F. Zeng, B. L. Folta, and J. F. Labuz, "Strength testing of sandstone under multi-axial stress states," *Geotechnical and Geological Engineering*, vol. 37, no. 6, pp. 4803–4814, may 2019. doi: 10.1007/s10706-019-00939-5
- [4] C. J. Jaeger and N. G. W. Cook, *Fundamentals of Rock Mechanics, 3rd edition.* Chapman and Hall, 1979.
- [5] E. Hoek, E. T. Brown, and E. Vol, "Empirical strength criterion for rock masses," *Journal of the Geotechnical Engineering Division, ASCE.*, vol. 106, pp. 1013–1015, 1980.
- [6] J. Labuz, S.-T. Dai, and E. Papamichos, "Plane-strain compression of rock-like materials," *International Journal of Rock Mechanics and Mining Sciences & Geomechanics Abstracts*, vol. 33, no. 6, pp. 573–584, sep 1996. doi: 10.1016/0148-9062(96)00012-5
- [7] R. Makhnenko and J. Labuz, "Plane strain testing with passive restraint," *Rock Mechanics and Rock Engineering*, vol. 47, no. 6, pp. 2021–2029, nov 2013. doi: 10.1007/s00603-013-0508-2
- [8] B. Paul, "Generalized pyramidal fracture and yield criteria," *International Journal of Solids and Structures*, vol. 4, pp. 175–196, 1968.
- [9] J. P. Meyer and J. F. Labuz, "Linear failure criteria with three principal stresses," *International Journal of Rock Mechanics and Mining Sciences*, vol. 60, pp. 180–187, jun 2013. doi: 10.1016/j.ijrmms.2012.12.040
- [10] B. Folta, "Strength testing under multi-axial stress states," Master's thesis, Department of Civil, Environmental and Geo-Engineering, University of Minnesota, 2016. [Online]. Available: <http://hdl.handle.net/11299/182131>

Bibliography

- [11] M. Ostrom, “Cambrian stratigraphy in western wisconsin,” 1966. [Online]. Available: https://wgnhs.wisc.edu/pubs/download_ic07/
- [12] R. Ulusay, “The isrm suggested methods for rock characterization, testing and monitoring: 2007-2014,” *ISRM*, 2015.
- [13] “Practices for preparing rock core as cylindrical test specimens and verifying conformance to dimensional and shape tolerances,” 2019. doi: 10.1520/d4543-19
- [14] J. Labuz and J. Bridell, “Reducing frictional constraint in compression testing through lubrication,” *International Journal of Rock Mechanics and Mining Sciences & Geomechanics Abstracts*, vol. 30, no. 4, pp. 451–455, aug 1993. doi: 10.1016/0148-9062(93)91726-y
- [15] J. Franklin and E. Hoek, “Developments in triaxial testing technique,” *Rock mechanics*, vol. 2 (4), p. 223–228.
- [16] T. Benz and R. Schwab, “A quantitative comparison of six rock failure criteria,” *International Journal of Rock Mechanics and Mining Sciences*, vol. 45, no. 7, pp. 1176–1186, oct 2008. doi: <https://doi.org/10.1016/j.ijrmms.2008.01.007>